

AD-A235 002
████████████████████

AEOSR-JR- 91 0264

2

**Damage Accumulation in Advanced Metal Matrix Composites
under Thermal Cycling**

M. Taya, M. Ramulu, W. Armstrong, and M. Dunn
Department of Mechanical Engineering
Mail Stop FU-10
University of Washington
Seattle, Washington 98195

DTIC
ELECTE
APR 17 1991
S C D

25 February 1991

Final Report for Period 1 October 1987 - 15 October 1990

Prepared for

AIR FORCE OFFICE OF SCIENTIFIC RESEARCH
Bolling Air Force Base
Washington, DC 20332

DTIC FILE COPY

91 4 16 056

REPORT DOCUMENTATION PAGE

Form Approved
OASD No. 0704-0108

1a. REPORT SECURITY CLASSIFICATION unclassified		1b. RESTRICTIVE MARKINGS	
2a. SECURITY CLASSIFICATION AUTHORITY		3. DISTRIBUTION / AVAILABILITY OF REPORT Unlimited	
2b. DECLASSIFICATION / DOWNGRADING SCHEDULE			
4. PERFORMING ORGANIZATION REPORT NUMBER(S) UW-ME-91-001		5. MONITORING ORGANIZATION REPORT NUMBER(S) AEOSR-TR- 91 0261	
6a. NAME OF PERFORMING ORGANIZATION University of Washington	6b. OFFICE SYMBOL (if applicable) UW-ME	7a. NAME OF MONITORING ORGANIZATION Air Force Office of Scientific Research	
6c. ADDRESS (City, State, and ZIP Code) Department of Mechanical Engineering Seattle, WA 98195		7b. ADDRESS (City, State, and ZIP Code) Bolling Air Force Base Washington, D.C. 20332 <i>BA410</i>	
8a. NAME OF FUNDING / SPONSORING ORGANIZATION Air Force Office of Sci Res	8b. OFFICE SYMBOL (if applicable) AFOSR / <i>NA</i>	9. PROCUREMENT INSTRUMENT IDENTIFICATION NUMBER AFOSR-89-0059	
8c. ADDRESS (City, State, and ZIP Code) Bolling Air Force Base Washington, DC 20332 <i>BA410</i>		10. SOURCE OF FUNDING NUMBERS	
		PROGRAM ELEMENT NO. <i>101001</i>	PROJECT NO. <i>2302</i>
		TASK NO. <i>B2</i>	WORK UNIT ACCESSION NO.
11. TITLE (Include Security Classification) Damage Accumulation Process in Advanced Metal Matrix Composites Under Thermal Cycling <i>(W)</i>			
12. PERSONAL AUTHOR(S) Minoru Taya, Mamidala Ramulu, William Armstrong, Marty Dunn			
13a. TYPE OF REPORT Final report	13b. TIME COVERED FROM 10/14/89 TO 10/15/90	14. DATE OF REPORT (Year, Month, Day) 25 February 1991	15. PAGE COUNT 185
16. SUPPLEMENTARY NOTATION			
17. COSATI CODES			18. SUBJECT TERMS (Continue on reverse if necessary and identify by block number) Metal Matrix Composites, Damage Accumulation Process, Thermal Cycling, Powder Processing, Machining, Damage model
FIELD	GROUP	SUB-GROUP	
19. ABSTRACT (Continue on reverse if necessary and identify by block number) <p>This research investigates the response to thermal cycling of a set of W-1% ThO₂ reinforced Fe-25CR-8Al-.50Y superalloy matrix composites. During this research, unique composite materials were produced by powder metallurgical processing. These materials were three aligned composites of differing reinforcement aspect ratio, and a hierarchic composite which included fine diameter Al₂O₃ fibers. After HIP processing, specimen blanks were cut from the HIP billets by abrasive water-jet after which specimens were turned using a conventional engine lathe. The specimens were then thermal sprayed with an oxidation resistant FeCrAlY coating identical to the matrix material. The specimens were then thermal cycled between 1100 C and 352 C and between 1100 C and 534 C for 100, 500, or 750 cycles on a specially built thermal cycling machine. The dimensional change of each specimen was measured. It was found that the initial longitudinal growth per thermal cycle was</p>			
20. DISTRIBUTION / AVAILABILITY OF ABSTRACT <input checked="" type="checkbox"/> UNCLASSIFIED/UNLIMITED <input type="checkbox"/> SAME AS RPT. <input type="checkbox"/> DTIC USERS		21. ABSTRACT SECURITY CLASSIFICATION Unclassified	
22a. NAME OF RESPONSIBLE INDIVIDUAL George Haritos		22b. TELEPHONE (Include Area Code) (202) 767-4987	22c. OFFICE SYMBOL AFOSR

19. ABSTRACT continued

small. After many thermal cycles however the longitudinal growth per thermal cycle became much larger.

A severe growth of fiber-matrix interfacial damage was documented with Scanning Electron Microscopy. The growth of two interfacial reaction phases was determined with a KEVEX dispersive x-ray analysis. The mechanical properties of the interfacial material were investigated with a Vickers microhardness test. Finally, the basic mechanical response of the material was investigated with room temperature tensile testing.

The experimental results were analyzed using a new micro-mechanics model. It was found that the predictions of the model agreed with experimental data from the W-FeCrAlY, the W-Cu, and the SiC-Al composite systems. The model was then able to qualitatively explain the measured increase in longitudinal strain per thermal cycle with increasing interfacial damage. Finally, based on model and experimental results, a multi-scale hybrid metal matrix composite configuration which is not expected to develop a large longitudinal growth per thermal cycle is recommended.

Accession For	
NTIS Special	<input checked="" type="checkbox"/>
DTIC	<input type="checkbox"/>
Unclassified	<input type="checkbox"/>
Justification	
By	
Distribution	
Availability	
Dist.	Special
A-1	

TABLE OF CONTENTS

List of Figures.....	v
List of Tables.....	xi
Chapter 1 Introduction.....	1
Chapter 2 Literature Review	3
2.1 Metal Matrix Composite Processing.....	3
2.1.1 Metal Matrix Composite Processing Methods...	3
2.1.2 MMC Processing Defects.....	7
2.2 MMC Damage Processes	9
2.2.1 Mechanical Damage Processes	9
2.2.2 Thermal-Mechanical Damage Processes	9
2.3 W / FeCrAlY Metal Matrix Composites.....	11
2.3.1 Tungsten Fiber Properties	11
2.3.2 FeCrAlY Matrix Properties	12
2.3.3 W-FeCrAlY Interfacial Properties	13
2.3.4 W-FeCrAlY under Thermal Cycling.....	14
2.4 Thermal Cycling Deformation Models	17
2.4.1 Garmong's Model	17
2.4.2 Yoda et al's Model.....	22
2.4.3 Taya-Mori's Model.....	27
Chapter 3 Test Specimen Processing.....	36
3.1 Material Production.....	36
3.1.1 Fiber Processing	36
3.1.2 Matrix Processing.....	37
3.1.3 Composite Assembly.....	39

	3.1.4	Polymer Burn-off.....	41
	3.1.5	Hot Isostatic Press Processing.....	43
3.2		Specimen Fabrication.....	45
	3.2.1	Abrasive Water-jet Cutting.....	45
	3.2.2	Specimen Machining	46
	3.2.3	Specimen Coating.....	47
3.3		Initial Specimen Characteristics.....	48
	3.3.1	Volume Fraction of Reinforcement.....	48
Chapter 4		Thermal-Mechanical Testing.....	49
	4.1	Tensile Testing	49
	4.1.1	Tensile Test Apparatus and Procedures	49
	4.1.2	Room Temperature Tensile Test Results.....	50
	4.2	Thermal Cycling Testing.....	54
	4.2.1	Thermal Cycling Test Apparatus and Procedures.....	54
	4.2.2	Creep Thermal Cycling Machine.....	57
	4.3	Thermal Cycling Dimensional Change Results.....	62
Chapter 5		Material Analysis.....	70
	5.1	Damage Processes	70
	5.1.1	Growth of Reaction Phases.....	70
	5.1.2	Transmission Electron Microscopy Study	88
	5.1.3	Thermal Spray Layer Damage.....	93
	5.2	Interfacial Microporosity Growth.....	96
Chapter 6		Mechanical Analysis.....	114
	6.1	Thermal Cycling Deformation Model.....	114
	6.1.1	Eshelby's Model	115
	6.1.2	Analytical Model for Thermal Cycling Strain.	118
	6.2	Comparison of Present Model with Previous Models	128
	6.3	Comparison of Present Model with Experiment	134

6.3.1	W-1%ThO ₂ Reinforced 67Fe-24Cr-8Al-0.5Y	134
6.3.2	W Reinforced Cu	145
6.3.3	SiC Reinforced 2124-T6 Al	150
6.4	Analysis of the Case of Defected Interfaces	154
Chapter 7	Conclusions and Recommendations.....	159
7.1	Conclusions	159
7.2	Recommendations	160
References	164
Appendix A	Cox Shear Lag Model.....	177
Appendix B	Eshelby Tensors	182

LIST OF FIGURES

Number	Page
Figure 2.1	Garmong Thermal Cycling Deformation Model Result.21
Figure 2.2	Yoda et al Thermal Cycling Deformation Model.....22
Figure 2.3	Yoda et al Experimental Thermal Cycling Strain Result Compared to Model Prediction.26
Figure 2.4	Temperature Time Curve for Taya-Mori Thermal Cycling Model27
Figure 2.5	Taya-Mori Thermal Cycling Deformation Model Result.35
Figure 3.1.	Filament Winding Machine.....36
Figure 3.2	Composite Specimen Fabrication.....39
Figure 3.3	Burn-off Time Temperature Schedule.....41
Figure 3.4	Hot Isostatic Press Time Temperature Pressure Schedule.43
Figure 3.5	Tungsten Carbide Cutting Tool Geometry.....46
Figure 3.6	Machined Thermal Cycling Test Specimen.....47
Figure 4.1	FeCrAlY Matrix Stress Strain Diagram.50
Figure 4.2	FeCrAlY CF Comparative Stress Strain Diagram. ...51
Figure 4.3	Composite Stress Strain Diagram.....52
Figure 4.4	Comparative Stress Strain Diagram, ASF-20, AF....53
Figure 4.5.	Metallurgical Thermal Cycler.....55
Figure 4.6	Creep Thermal Cycling Machine.....57
Figure 4.7	Furnace Transport System.....58
Figure 4.8	Silicon Carbide Resistance Element Furnace.....59

Figure 4.9	Creep Thermal Cycler Time-Temperature History....60
Figure 4.10	Normalized Length Change Versus Number of Thermal Cycles, 1100-352 C.63
Figure 4.11	Normalized Length Change Versus Number of Thermal Cycles, 1100-534 C.64
Figure 4.12	Normalized Length Change Versus Number of Thermal Cycles, ASF-20, ASF-5 Comparison.65
Figure 4.13	Normalized Length Change Versus Number of Thermal Cycles, ASF-20, AF Comparison.66
Figure 4.14	Normalized Area Change Versus Number of Cycles, 1100-352 C.....68
Figure 4.15	Normalized Area Change Versus Number of Cycles, 1100-534 C.....69
Figure 5.1	Microstructural Features Observed During Microscopy.....72
Figure 5.2(a)	CF, as-received, Normal View.73
Figure 5.2(b)	CF, 500 cycles 1100-352 C, Normal View.....73
Figure 5.3	ASF-20, 500 cycles 1100-352 C, Normal View.74
Figure 5.4(a)	ASF-5, as received, Normal View.74
Figure 5.4(b)	ASF-5, 500 cycles 1100-352 C, Normal View.....75
Figure 5.4(c)	ASF-5, 1000 cycles 1100-352 C, Normal View.75
Figure 5.5(a)	AF, as received, Normal View.....76
Figure 5.5(b)	AF, 500 cycles 1100-352 C, Normal View.....76
Figure 5.5(c)	AF, 1000 cycles 1100-352 C, Normal View.....77
Figure 5.6	Reaction Zone Crack Density Versus Number of Thermal Cycles.78
Figure 5.7	Attached Reaction Zone Thickness Versus Number of Thermal Cycles.....79
Figure 5.8(a)	Atomic Weight Percent Versus Distance, CF, as received.....80

Figure 5.8(b)	Atomic Weight Percent Versus Distance, CF, 500 cycles 1100-352 C.....	81
Figure 5.9(a)	Atomic Weight Percent Versus Distance, AF, as received.....	82
Figure 5.9(b)	Atomic Weight Percent Versus Distance, AF, 500 cycles 1100-352 C.....	83
Figure 5.10	Chromium Weight Percent Versus Distance, CF.....	84
Figure 5.11	Chromium Weight Percent Versus Distance, AF.....	85
Figure 5.12	Microhardness Indentations of ASF-5, 500 cycles 1100-352 C.....	86
Figure 5.13	Microhardness Indentations of AF, 500 cycles 1100-352 C.....	86
Figure 5.14	Vickers Microhardness Versus Distance.....	87
Figure 5.15	AF, 500 Cycles, Attached Reaction Layer.....	89
Figure 5.16	ASF-20, 500 Cycles, Matrix and Attached Reaction Zone.....	90
Figure 5.17(a)	AF, 500 Cycles, Matrix and Attached Reaction Zone.....	91
Figure 5.17(b)	AF, 500 Cycles, Matrix and Alumina Fiber.....	92
Figure 5.18(a)	ASF-20, 100 cycles, Thermal Spray Layer.....	94
Figure 5.18(b)	ASF-20, 500 cycles, Thermal Spray Layer.....	94
Figure 5.18(c)	ASF-20, 500 cycles, Specimen Exterior.....	95
Figure 5.19(a)	ASF-5, 500 cycles, 1100-352 C, Lateral Section View, Fiber End.....	97
Figure 5.19(b)	ASF-5, 500 cycles, 1100-352 C, Lateral Section View, 800 Micron from Fiber End.....	97
Figure 5.20(a)	ASF-5, 750 cycles, 1100-352 C, Lateral Section View, Fiber End.....	98
Figure 5.20(b)	ASF-5, 750 cycles, 1100-352 C, Lateral Section View, 800 Micron from Fiber End.....	98

Figure 5.21(a)	AF, 500 cycles, 1100-352 C, Lateral Section View, Fiber End.	100
Figure 5.21(b)	AF, 500 cycles, 1100-352 C, Lateral Section View, 800 Micron from Fiber End.	100
Figure 5.22(a)	AF, 750 cycles, 1100-352 C, Lateral Section View, Fiber End.	101
Figure 5.22(b)	AF, 750 cycles, 1100-352 C, Lateral Section View, 800 Micron from Fiber End.	101
Figure 5.23(a)	ASF-20, 500 cycles, 1100-352 C, Lateral Section View, Fiber End.	103
Figure 5.23(b)	ASF-20, 500 cycles, 1100-352 C, Lateral Section View, 800 Micron from Fiber End.	103
Figure 5.24(a)	CF, 500 cycles, 1100-352 C, Lateral Section View, Fiber End.	105
Figure 5.24(b)	CF, 500 cycles, 1100-352 C, Lateral Section View, 800 Micron from Fiber End.	105
Figure 5.25	Damage Quantifying SEM Photograph Locations. .	107
Figure 5.26	Interfacial Porosity as a Function of Distance from Fiber End, ASF-5, 500 and 700 cycles.	108
Figure 5.27	Interfacial Porosity as a Function of Distance from Fiber End, AF, 500 and 700 cycles.	109
Figure 5.28	Interfacial Porosity as a Function of Distance from Fiber End, ASF-5 and ASF-20, 500 Cycle Comparison.	110
Figure 5.29	Interfacial Porosity as a Function of Distance from Fiber End, AF and ASF-20, 500 Cycle Comparison.	111
Figure 5.30	The Damage Accumulation Process.	112
Figure 6.1	Eshelby Domains.	115

Figure 6.2	Idealized Time-Temperature Excursion Curve.	118
Figure 6.3	Model Stress and Strain versus Temperature Behavior.	125
Figure 6.4	Comparison of Present Model with Computed Garmong Result.	130
Figure 6.5	Expanded View of Figure 6.4.....	131
Figure 6.6	Taya-Mori Stress Relaxation.....	133
Figure 6.7	0.2% Yield Stress Versus Temperature for FeCrAlY (from Wukusick and Collins, 1964).....	136
Figure 6.8	Model Strain Components versus Fiber Volume Fraction.....	138
Figure 6.9	Model Strain Components versus Fiber Volume Fraction.....	139
Figure 6.10	Model Strain Components Versus Fiber Aspect Ratio.....	140
Figure 6.11	Strain Per Thermal Cycle Versus Fiber Volume Fraction.....	141
Figure 6.12	Strain Per Thermal Cycle Versus Fiber Aspect Ratio.....	142
Figure 6.13	Thermal Cycling Strain versus Number of Thermal Cycles, W-FeCrAlY Experimental Result.....	143
Figure 6.14	Comparison of Model Prediction with Experimental Result for Thermal Cycling Strain per Cycle versus Volume Fraction of Fiber, W-1%ThO ₂ FeCrAlY.....	144
Figure 6.15	Thermal Cycling Strain versus Number of Thermal Cycles, W-Cu Experimental Result.	14
Figure 6.16	Comparison of Model Prediction with Experimental Result for Thermal Cycling Strain per Cycle versus Volume Fraction of Fiber, W-Cu.....	148

Figure 6.17	Maximum Thermal Cycle Temperature versus Lateral Strain, SiC-Al, Experimental Result.....	152
Figure 6.18	Comparison of Model Prediction with Experimental Result for Thermal Cycling Lateral Strain per Cycle versus Volume Fraction of Fiber, SiC-Al.....	153
Figure 6.19	Progressively Damaged Fiber-Matrix Interface.	155
Figure 6.20	Hypothetical Damage Process.....	156
Figure 6.21	Integration of the Hypothetical Process in Figure 6.20.	157
Figure 7.1	Recommended Thermal Cycling Resistant W- FeCrAlY Composite Mixed Scale Hybrid Reinforcement Configuration.	161
Figure A1.	Cox Shear Lag Model Parameters	177
Figure A2.	Cox Model Result For W-FeCrAlY Composites. . .	181
Figure B.1	Sphere.....	182
Figure B.2	Oblate spheroid.	183
Figure B.3	Prolate spheroid.....	184

LIST OF TABLES

Number	Page
Table 2.1 TRW Thermal Cycling Under Load Data.....	15
Table 2.2 Garmong Model Input Parameters	20
Table 2.3 Taya-Mori Model Input Parameters.....	34
Table 3.1 Produced Composite Materials	48
Table 4.1 Longitudinal Thermal Cycling Strain	62
Table 4.2 Normalized Thermal Cycling Area Deformation.....	67
Table 6.1 Garmong Model Input Parameters	128
Table 6.2 Taya-Mori and Present Model Input Parameters.....	129
Table 6.3 Input Data for W-FeCrAlY.....	134
Table 6.4 Creep Data for FeCrAlY (ref. Saller et al, 1954)	137
Table 6.5 Input Data for W-Cu	145
Table 6.6 Input Data for SiC-Al.....	150
Table 7.1 Input Data for Recommended W-FeCrAlY Mixed Scale Hybrid Composite.....	163

Chapter 1 Introduction

Metal matrix composite research has been motivated by the expectation of significantly improved mechanical properties which would lead in turn to previously unobtainable performance in heat engine and high temperature structural applications. Unfortunately, these performance expectations have proven very difficult to realize. This is because the optimistic expectations are usually based on a number of simplifying assumptions.

The most common simplifying assumptions are; the metallic matrixes will retain properties identical to a monolithic metal of the same chemical composition, the reinforcement will remain unchanged, and the material bond between the two remains perfect. With this set of assumptions metal matrix composites appear to have the most desirable performance possibilities of any material system, combining the advantages of metals and ceramics. They would have high toughness and defect tolerance since any crack growth would entail plastic flow. The microstructures of the metal matrixes would be enhanced with simple heat treatments. Useful articles could be processed and fabricated using the same basic metallurgical manufacturing techniques common in metals. The strength and fatigue resistance would be high, since the reinforcing fibers are both strong and fatigue resistant. Finally the composites would have possibilities unique to them. They could eliminate high strain gradients by distributing internal forces through large domains, and they would allow the possibility of specifying particular properties in a nonisotropic way.

The complexities of real composite behavior makes the attainment of the above desirable possibilities much more difficult. The composite will contain high residual stresses due to the large mismatch in thermal expansion between matrix and fiber. The matrix will develop exceedingly complicated dislocation configurations which in general are never realized in monolithic metals. Defect structures coalesce into extremely complicated geometric arrangements. Significant chemical interdiffusion

and reactions often occur which strongly affects the nature of the fibers, matrix, and interface. The fibers will often develop attached intermetallic reaction zones which have low defect tolerance and high defect populations. Finally the material will have some degree of damage due to the manufacture of the composite.

This thesis investigates the response to thermal cycling of a W-1% ThO₂ reinforced 67% Fe-25% Cr-8% Al-0.5% Y matrix composite. It is expected that the results of this study will be of technological interest since this material is under active consideration for use in high temperature structures. It is expected that the results of this study will be of scientific interest since thermal cycling testing provides clear contrast between the predictions of simple phenomenological models and the results of complex material processes.

Within the body of this thesis, a literature review examines significant previous work. The techniques used to produce and thermal cycle the target material are explained. A number of experimental results will be presented which document the evolution of complex thermal-mechanical damage processes. An analytical model will then be developed which predicts well the longitudinal thermal cycling deformation rate of several different composite systems when the structure of these materials are simple. This analysis will then in a qualitative way explain the rate of thermal cycling deformation when the material evolves into a more complex state.

Chapter 2 Literature Review

2.1 Metal Matrix Composite Processing

2.1.1 Metal Matrix Composite Processing Methods

Metal matrix composite (MMC) processing can be conveniently divided into three categories: (1) Molten Metal Processing, (2) Diffusion Processing, and (3) Deposition Processing. The suitability of each for a particular material system is determined primarily by the ability of the chosen processing to provide an optimization of interfacial strength without undue interfacial chemical degradation. However there are other significant considerations including cost, residual thermal stresses, reinforcement damage, matrix porosity, reinforcement geometry, matrix dislocation configuration, warpage, and required post fabrication.

(1) Molten Metal Processing:

Molten metal processing brings the matrix metal into contact with the reinforcement in a molten state. The high matrix material temperatures required promote aggressive fiber-matrix reaction which generally result in both strong interfacial strength, and high interfacial reaction. When the composite is cooled to room temperature large thermal mismatch strains develop. The method is actively pursued in spite of its inherent disadvantages since it is expected to provide better economics than competing solid state processes.

An example of this type of processing is provided by an investment casting process performed using a tungsten 2% thoria fiber MAR M322E matrix (Helmink and Piwonka, 1979). In this example a blade mold was made by dipping and stuccoing a

wax assembly which contained oriented fibers. The finished mold was placed into a vacuum and preheated to 1371 C. The MAR M322E charge was poured into the mold at 1321 C. The filled mold was then withdrawn from the furnace and allowed to cool by radiation. When the resultant composite was examined thermal damage was evidenced by numerous circumferential cracks around the reinforcement and a 9 micron wide fiber-matrix reaction zone.

A form of molten metal processing which has proven very successful for low reactivity material systems is squeeze casting. In this technique a preheated reinforcement array is injected with molten metal under high pressure. The entire assembly is then rapidly cooled so that the deleterious interfacial reactions have limited time to progress. A particularly promising material system for this type of processing has been alumina fiber reinforced aluminum composites (Mortensen et al, 1986). In this material system the alumina fiber reactivity is low, the maximum processing temperatures required for the aluminum matrix are low, and the thermal conductivity of the aluminum matrix is high.

(2) Diffusion Processing:

The most successful composite processing technique in highly reactive systems has been diffusion processing. In this method solid metal matrix powders or foils are compacted at sufficient pressures and temperatures to consolidate the matrix with diffusion mass transport. The great advantage of this technique is that the maximum matrix temperatures are lower in this case as compared to molten metal processes thus reducing the extent of interfacial reaction and thermal residual stresses.

An interesting example of this type of solid state processing was used to produce a W-2% Thoria fiber Kovar (Fe-29Ni-17Co) matrix composite. In this study (Larsson and Warren, 1979) the matrix material was obtained as tubing with an inner diameter of 0.4 mm and an outer diameter of between 0.5 mm and 0.7 mm. The tungsten reinforcement had a diameter of 0.3 mm. The reinforcing fibers were threaded into the tubing in 2 m lengths and then the material was cut into suitable smaller lengths. The material was encapsulated into cylindrical HIP capsules with a plug of excess

matrix material at the fiber ends. The material was HIPed at pressures between 150 and 250 MPa and temperatures between 1050 C and 1200 C. Upon examination, the fibers were found to be very well dispersed and the reaction layer thickness varied between one and twenty micron.

A reference of particular interest to this study used warm rolled Teflon to bind a FeCrAlY powder (Brentnall, 1974). During the warm rolling the Teflon formed an interconnected stringy mass which entrained the matrix powders. Reinforcement fibers of Mo-TZM, and W-1% thoria were wound on a drum, and then coated with a binder. The fiber sheets and matrix powder cloths were assembled into the correct geometric configuration, and then the organic materials were burned off. After polymer burn-off the composite was diffusion consolidated in a hot press. A variation of this process used a paraffin wax powder binder, and fibers hand laid onto adhesive tape (Morimoto and Taya, 1988).

A mixed form of diffusion / deformation processing was used to consolidate a W 1% ThO₂ / FeCrAlY composite (Rozner and Wiley, 1979). In this study the composite was initially sintered at high temperature. After sintering the composite was hot swaged. During swaging the porosity was greatly reduced while the reinforcement configuration remained nearly the same. Following hot swaging, the material was upset, hammer forged, and then closed die forged to produce a turbine airfoil shape. It was found that the near surface tungsten fibers smoothly followed the contours of the forging indentions while more centered fibers remained straight. The resulting forged airfoils had fibers distributed randomly in the lateral direction and well oriented in the longitudinal direction.

(3) Deposition Processing:

The most successful form of deposition processing for structural materials has been spray deposition processing. In this method an atomised stream of molten metal particles is sprayed onto a warm substrate or fiber preform. The primary advantages of this method are that the matrix and reinforcement are in contact at very high temperatures only for a very short time, the deposited matrix material is free of binder

impurities, and the extent of interfacial reaction is low since the matrix particles remain at high temperatures for very short amounts of time (McKimpson and Scott, 1989). Additionally this form of composite fabrication is able to co-deposit discontinuous, misoriented reinforcement along with the matrix material.

Experience with spray deposition of monolithic metals has shown that the best possible spraying condition is one where the sprayed surface retains a very thin layer of semi-molten material at the time of the arrival of a splat (Evans et al, 1985). This condition gives rise to a favorable low porosity, equiaxed microstructure. This optimal deposition condition will not be uniformly met in practice, however, since the statistical distribution of particle sizes produces variations in splat impact conditions, and the distribution in impact sequencing produces variations in impacted surface conditions. Examples of the types of microstructural details produced by spray nonuniformity include poorly bonded grain boundaries, porosity, and reinforcement debonding. Because of these defects post-deposition processing is usually required to improve the consolidation of the spray deposited sheets. While the matrix material is being sprayed, short fibers can be co-deposited. To do this it is only necessary to entrain a controlled amount of chopped fibers in the high velocity gas plasma flow (Singer and Ozbek, 1985). Since the spray is impacting on a thin layer of semi-molten material which solidifies very quickly, gravimetric separation does not occur between the particles and the co-deposited reinforcement. Additionally since the solidification occurs near a free boundary, the magnitude of the thermal mismatch stress is decreased.

In an example of co-deposition processing, lamellar structures were produced in a FeCrAlY matrix and alumina or mullite fiber composite in a low pressure plasma process (Jackson and Mehan, 1987). The extremely fast cooling rates of 10^5 to 10^6 C/sec produced a very fine matrix microstructure and also eliminated significant interfacial reaction. The produced composites also had very low levels of interfacial porosity.

Another example of co-deposition processing was used to create a 218CS tungsten fiber FECRALLOY matrix (Westfall, 1985). In this case the tungsten wires were

wrapped on a mandrel which was mounted in an inert gas enclosure. The matrix material was sprayed onto the rotating mandrel coating the fibers and creating the monotape. The sprayed monotape was cut into appropriate sized sheets and stacked. Finally the material was HIP processed. The produced composite was compared to a diffusion processed composite made with an organic binder and was found to be 10 MPa stronger. The superior strength of the deposition processed material was ascribed to the avoidance of organic residue contamination.

The most common form of post-deposition processing has been to HIP process cut and stacked layers of thermal sprayed sheets (Westfall, 1985). This method has shown very good results for a variety of composite systems and would be the preferred method for any application where the product geometry is compatible with an available HIP machine. An example of an intermetallic composite processed this way had Al_2O_3 fibers in a Ni_3Al matrix (German and Bose, 1988). Consolidation was good after one hour at 1100 C and 172 MPa. The resultant HIP product was found to be superior to several reaction hot isostatic pressed composites processed at lower temperatures.

2.1.2 MMC Processing Defects

A basic challenge in the processing of metal matrix composite systems is to control the extent of factors proven deleterious in monolithic structural metals. For instance, it is a normal monolithic metal design practice to avoid the creation of large stress gradients, but composite materials will always have inherently high stress gradients near the reinforcing phase. It is usually desirable to avoid any interior chemical degradation during service, but metal matrix composite materials will generally have chemically active interfaces because it is these interfaces which provide the strongest interfacial bonding. The porosity of typical engineering materials are kept very low, while composite materials have a significant amount of porosity associated with the introduction of the reinforcing phase. Finally nonloaded monolithic parts are normally required to be stress free, while composite materials always retain significant levels of internal thermal residual stress. The composite is said to be

defected only when one of these undesired factors has a significant effect on an important property.

Another basic challenge in the use of composite materials is due to the difficulty in optimizing a particular single composite factor without suffering decreased properties from another related factor. For example, high interfacial reactivity provides good matrix-fiber wetting and a strong bond but also increased detrimental fiber-matrix reaction. High volume fraction of reinforcement can provide high strength and low density but also increased matrix triaxiality and lowered fracture toughness. High working temperatures will result in lowered matrix viscosity and easier matrix consolidation, but also increased thermal residual stress and increased fiber-matrix reaction. Small fiber diameter can lead to increased fracture resistance but also greater vulnerability to fiber strength loss due to interfacial reactions. From these considerations it is seen that the metal matrix composite processor must trade-off inherently contradictory properties.

A different type of defect than that discussed so far is labeled a structural defect. These defects are due to the failure of the processor to provide a perfect geometrical arrangement of fibers and matrix. Examples of structural defects include matrix rich areas, fiber clumping, excessive porosity, and fiber misalignments (Rack and Ratnaparkhi, 1988). This type of defect decreases the ability of the composite to support mechanical and thermal loads since strain and stress gradients become large in the defect dominated domains. Additionally these defects decrease the fatigue resistance of the composite since the matrix rich domains will allow the growth of larger matrix defect structures.

2.2 MMC Damage Processes

2.2.1 Mechanical Damage Processes

Metal matrix composites always experience at least one large cool-down from processing temperature before any significant applied service loading. Due to the large difference in thermal expansion coefficient between the reinforcement and matrix, large thermal residual stresses and plastic strains develop. These strain and stress fields are highly localized depending on the composites exact reinforcement geometry and property-processing history (Tanaka et al, 1982). The large plastic strains produce in turn a highly complex initial dislocation configuration in the composite (Davidson, 1987). During service the thermal residual stresses and the applied loads superimpose, often causing additional plastic straining. This additional plastic straining increases the severity and complexity of the dislocation configuration. Sufficiently severe dislocation configurations result in microcavities (Lemaitre and Dufailly, 1987). The result of this process is that any domain of the composite experiencing repeated plastic flow rapidly assumes a highly defected fatigue state.

In spite of this rapid damage development, experiments have shown some metal matrix composite materials have excellent mechanical fatigue resistance. This is due to the ability of these materials to "shakedown" to a configuration where only elastic straining occurs. The domains which were subjected to repeated plastic straining having lost any significant strength or stiffness (Johnson, 1982). Monolithic metals are often able to shakedown in a similar way but because of the inherent high stiffness and load transfer ability of reinforcements the composites are able to sustain much higher percentages of ultimate load.

2.2.2 Thermal-Mechanical Damage Processes

The previous section described the intensification of damage development in metal matrix composites due to the presence of the reinforcement. In spite of this

intensification the materials have often shown excellent mechanical fatigue resistance. This resistance is attributed to the ability of reinforced materials to shakedown to a configuration where only elastic straining occurs. However during sufficiently severe thermal-mechanical exposure the composite retains essentially no purely elastic strain domains near the fiber-matrix interface. Therefore, the interface becomes highly defected and the material advantages of compositing are lost.

In an example of this type of process Yoda et al, 1979, observed the matrix interfacial zones in a tungsten fiber reinforced copper composite thermal cycled between 200 C and 800 C. The matrix interface was observed by carefully removing the fibers and then using scanning electron microscopy on the exposed matrix interfacial surfaces. The initial interfacial attachment was very good as evidenced by surface markings on the tungsten wires due to wire drawing being expressed in the matrix. After 50 cycles the matrix interface contained round and isolated pores. After 200 cycles the pores had increased in numbers until they coalesced into a highly complicated irregular structure. Tensile tests were performed on the as-processed and as-cycled material and the results were consistent with a dramatic loss of interfacial strength.

In another example, Kyono et al, 1988, thermal cycled a carbon fiber aluminum composite between 30 C and 350 C. After thermal cycling the composite developed severe interfacial porosity and reduced tensile performance.

2.3 W / FeCrAlY Metal Matrix Composites

2.3.1 Tungsten Fiber Properties

The technological usefulness of tungsten is due to a unique set of physical properties. It has the highest melting point of any metal, 3410 C, and it has a very high density of 19.3 g/cm. The specific heat is very low, 29.03 J/mol-K at 1373 K, while the thermal conductivity is very high, 1.11 W/cm-K at 1373 K. The coefficient of linear thermal expansion is very low, 4.266×10^{-6} at 20 C, and the modulus of elasticity is high at 400 GPa (Mullendore, 1984).

The initial processing of commercial tungsten is by powder metallurgy. Billets are formed and then pre-sintered in hydrogen at 1200 C (Mullendore, 1984). The resulting compacts are fully sintered by resistive self heating at 2800 to 300 C. The produced billets are generally hot swaged or rolled and then drawn to fiber diameter. Since tungsten is unusual in that the ductility increases with increasing work, the drawing temperature steadily decreases. In the case of thoriated tungsten filament the principal factor controlling the microstructure is the response of the ThO₂ particles to the thermal mechanical processing conditions (Snow and Dunham, 1975). The initial drawing proceeds at such high temperatures that the thoria particles are plastic. As drawing temperature decreases the elongated thoria particles become increasingly hard and brittle until they start to break. Increasing deformation at this stage produces porosity associated with the thoria particles. This process develops a particle alignment along the fiber axis quite different from the original billet microstructure. The density of the worked thoriated fibers was measured to be 18.98 g/cc, a result which indicates the presence of nearly as much porosity as thoria. Recrystallization of the fibers produces highly elongated tungsten grains. It is thought that the presence of the aligned thoria particles reduces the mobility of the transverse grain boundaries.

The tensile ductility of drawn thoriated tungsten wires is very low (Harris and Ellison, 1966). The room temperature ductility of thoriated tungsten is approximately

1.95% while the 815 C ductility is approximately 0.85% when tested with a strain rate of $1.5 \times 10^{-4} \text{ sec}^{-1}$. When creep tests were performed on tungsten wire it was found that little primary creep occurred at 1371 C (Harris and Ellison, 1966). However when the creep temperature was decreased a greater amount of primary creep occurred and the extent of the secondary creep was decreased. Additionally there was no indication of recrystallization in a creep test at 1093 C for 100 hours. The 1371 C result gave a stress exponent consistent with a diffusion controlled process, while a 649 C result gave a stress exponent consistent with a dislocation glide process.

2.3.2 FeCrAlY Matrix Properties

FeCrAlY alloys are primarily used as high temperature oxidation coatings on nickel based superalloys. The alloys have a chromium content of approximately 25%. Increases in chromium content above this value result in a slight increase in oxidation resistance but at the cost of impaired workability and ductility (Wukusick and Collins, 1964). The aluminum content must be above 2% to provide an oxidation resistant Al_2O_3 layer. Increasing the aluminum content from 2% to 4% created an increasingly smooth and adherent oxide scale. Aluminum contents greater than 4% made the alloy increasingly brittle. This brittleness has been attributed to the formation of large alumina inclusions and an increasing grain size (Tjong et al, 1988). The yttrium had little influence on mechanical properties.

While the oxidation resistance of FeCrAlY is excellent, the high temperature mechanical properties are very similar to stainless steels. Since FeCrAlY alloys are typically used at much higher homologous temperatures than would be the case for stainless steels, creep and stress rupture are serious considerations. In fact the stress to produce rupture in 100 hours at 1093 C for a Fe 25-Cr 4-Al 1-Y alloy is only 3.49 MPa (Wukusick and Collins, 1964). Another study found that the ultimate tensile strength of a Fe 25-Cr 6-Al 1-Y alloy at 1000 C to be approximately 70 MPa (Wilson et al, 1978). The same study found the ultimate tensile strength at 20 C to be 1300 Mpa. Another problematic feature of the material is that the extent of tensile ductility has been found to be quite sensitive to temperature. A Fe 25-Cr 6-Al 1-Y alloy in a

11.35 mm gauge length, 3.2 diameter tensile specimen produced approximately 12% elongation at room temperature while a similar Fe 25-Cr 11-Al 1-Y specimen produced only 6% elongation at room temperature (Wilson et al, 1978). Both of these ductility values remained constant with increasing temperature until 400 C at which the ductility rose rapidly to approximately 30% at 600 C after which the ductility decreased.

The microstructure of well processed FeCrAlY alloys contain a dispersion of YFe₉ in a fine grained matrix (Wukusick and Collins, 1964). The yttrium has been shown to both , reduce the rate of formation, while increasing the quality of Cr₂O₃ scales. Yttrium also increases the adherence of Al₂O₃ and Cr₂O₃ scales (Golightly et al, 1976). In FeCrAl alloys without yttrium the oxide scale has been shown to grow into a very convoluted ridged structure (Golightly et al, 1976). The creation of this type of morphology requires the outward diffusion of aluminum. It is conjectured that the presence of the yttrium reduces the outward diffusion of the aluminum. The lateral growth of the oxide cannot occur in this case and pegging action is obtained by locking the scale around Y₂O₃ particles which result from YFe₉ oxidation. It is also conjectured that the yttrium oxide particles are preferred vacancy sinks which then reduce the formation of voids under the attached scale. The strength of the oxide scale bonding was particularly evident during a thermal cycling test when a FeCrAlY alloy showed no measurable increase in the rate of oxidation as compared to an isothermal exposure (Stott, 1979). Another study found that the tensile strain needed to cause oxide scale cracking at room temperature was 1.4% to 2.3%, values which are much higher than typical for adhered oxides (Golightly et al, 1979). Also during this study it was found that cooling the specimen to cause a thermal cycle did not affect the strain required for scale cracking.

2.3.3 W-FeCrAlY Interfacial Properties

The interface between W-1%ThO₂ fibers and FeCrAlY matrix has been shown to be a site of very active chemical and microstructural activity. The principal chemical event is the formation of an attached Fe-Cr-W ternary eutectic zone (Brentnall et al, 1974). The thickness of this reaction zone grows according to a parabolic equation in

time and temperature (Tien et al. 1989). The extent of the reduction in fiber section area was measured for a W-1% ThO₂ reinforced FeCrAlY as 9.3% at 1093 C for 10 hours and 24.1% at 1093 C for 100 hours.

In another study coupon samples were exposed in air for 10, 100, and 1000 hours at 1093 C (Brentnall, 1976). The thickness of the reaction zone was measured to be 3.8 micron at 10 hours, 6.60 micron at 100 hours, and 17.78 micron at 1000 hours.

2.3.4 W-FeCrAlY under Thermal Cycling

To investigate the thermal cycling response of tungsten reinforced superalloy materials Brentnall et al, 1975, thermal cycled 0.119 by 0.250 by 4.5 inch prismatic W-FeCrAlY composite specimens by resistance heating in an argon environment. The heat cycle was either between 1090 C and room temperature or between 1200 C and room temperature with a one minute heat up and four minute cool down time. The specimens exhibited wrinkled surfaces and a 20% reduction in tensile strength after 1000 cycles. There was no evidence of matrix or fiber cracking. Evidence of typical monolithic thermal fatigue damage such as grain boundary cracking and wedge crack propagation was also missing. However these judgments were evidently not made on the basis of electron microscopy. A damage process was indicated by specimens cycled 1000 times between 30 C and 1204 C having a 11 ksi lower tensile modulus than specimens cycled 100 times between the same temperatures.

In a later study Brentnall et al, 1977, thermal cycled with an applied load one set of specimens between 21 C and 649 C and another set between 21 C and 760 C. The specimen was brought to full load at the completion of the heat cycle which took 47 seconds. The total cycle time was 3.3 to 3.6 minutes. The results of these tests are given in Table 2.1.

Table 2.1 TRW Thermal Cycling Under Load Data

<u>Area</u>	<u>Orientation</u>	<u>Temperature (C)</u>	<u>Stress (ksi)</u>	<u>N</u>	<u>A length</u>	<u>A width</u>	<u>A thickness</u>	<u>R of</u>
	0	21-760	0-40	1000	2.05	0.00	-3.80	-3.80
	0	21-649	0-50	1001	6.40	-1.30	-8.90	-10.2
	0	21-649	0-60	1000	.67	-0.15	-0.02	-0.17
	÷ - 15	21-649	0-40	1000	3.98	-6.60	-1.60	-8.20
	÷ - 15	21-649	0-50	1000	16.70	-6.30	-7.30	-13.6

The specimens were reported to be free of surface cracks or distortion after the tests. The 15° oriented specimen subjected to a large longitudinal elongation of 16.70 mm. showed signs of necking. When this necked region was examined it was found that there were no signs of fiber debonding or internal cracking.

Wetherhold et al, 1988, thermal cycled a 37 volume percent 218 CS tungsten fiber FeCrAl matrix uniaxial composite 800 times to temperatures of 850, 1000, and 1090 C. The thermal cycling was done in a vacuum by resistance heating. Optical microscopy and scanning electron microscopy revealed an accumulation of damage in the interface reaction zone and in the matrix. The strength of the matrix-fiber bond was increased in the cycled material.

In another study Wetherhold et.al, 1987, thermal cycled the same composite as above from room temperature to 1090 C for 200, 300, 400, 600, and 800 cycles. A large amount of matrix and interface damage was found. An idealized thermal problem was calculated which showed that the tungsten fibers were forced by the resistance heating method to far higher temperatures on short time scales than was the matrix. It was conjectured that this thermal characteristic could be responsible for intensification of the matrix damage. During this same study the surface roughness of a .006 in thick FeCrAl coating was measured as a function of thermal cycling condition. It

was found that the composite surface roughened rapidly in the first 200 cycles after which the roughness steadily increased at a slower rate. Numerous surface cracks were found oriented normal to the fiber axis. These cracks were particularly numerous in thin coating areas.

Morimoto and Taya, 1988, thermal cycled W-1% ThO₂ and Al₂O₃ reinforced FeCrAlY specimens from room temperature to 1100 C with a twelve minute cycle time. This study was unique in that the specimens were thermal cycled in furnaces rather than resistance heated. Damage processes were indicated in the case of uniaxially aligned continuous W- 1% ThO₂ FeCrAlY when the specimen diameter increased by approximately 5% within the first 100 cycles and then remained at this amount until 200 cycles. During this study the thermal cycled specimens generally warped. This behavior made accurate determination of residual properties quite difficult. A SEM investigation was performed after cycling to determine the cause of the observed dimensional changes. This investigation gave evidence of microcracking in the fiber-matrix interface. However this study found far less evidence of matrix damage than had earlier resistance heating studies.

2.4 Thermal Cycling Deformation Models

2.4.1 Garmong's Model

The assumptions underlying this model are: 1) the composite deformation is one-dimensional, 2) the stresses and strains are uniform within each phase, 3) the interfaces are perfect, and 4) the composite is metallurgically stable (Garmong, 1974). The one-dimensional nature of the model restricts the analysis to uniaxial continuous fiber composite cases, however the model is applicable to a wide variety of heating-cooling scenarios.

In beginning the derivation of the model, Garmong identified the stress equilibrium equation as

$$\sigma_c = \sigma_f V_f + \sigma_m V_m \quad (2.4.1)$$

As a consequence of assumptions (1), (2), and (3) both fiber and matrix are deformed at the same rate during the process. In this case the strain continuity equation becomes

$$\varepsilon_m(t) - \varepsilon_m(t=0) = \varepsilon_f(t) - \varepsilon_f(t=0) \quad (2.4.2)$$

In both cases the $t = 0$ strains are elastically recoverable strains. The fiber is assumed to remain elastic at all times so its strain is given by

$$\varepsilon_f = \frac{\sigma_f}{E_f} \quad (2.4.3)$$

The matrix strain is given by

$$\varepsilon_m = (\varepsilon_m)_e + (\varepsilon_m)_c \quad (2.4.4)$$

where the subscript c refers to anelastic creep strain and the subscript e refers to recoverable elastic strain.

A basic definition of time dependant creep rate is given by

$$\left(\dot{\epsilon}_m\right)_c = \frac{d}{dt} \left(\epsilon_m\right)_c \quad (2.4.5)$$

Garmong chose the Dorn formulation for steady state creep which is given by

$$\left(\dot{\epsilon}_m\right)_c = -A \left(\frac{|\sigma_m|}{G}\right)^s \frac{G b}{k T} D_o e^{-Q/RT} \quad (2.4.6)$$

where G is the matrix shear modulus, b is the matrix Burgers vector, k is Boltzmann's constant, R is the gas constant, D_o is the pre-exponential constant, and Q is the activation constant for self diffusion

The general governing equation was then given as

$$\int_{T_1}^{T_2} (\alpha_m - \alpha_f) dT = \frac{\sigma_a - \sigma_m V_m}{V_f E_f} - \frac{\sigma_m}{E_m} + \left[\frac{\sigma_m - \sigma_o}{K^*}\right]^{1/n} \\ + \int_{T_1}^{T_2} A \left(\frac{|\sigma_m|}{G}\right)^s \frac{G b}{k T} D_o e^{-Q/RT} \left(\frac{dt}{dT}\right) dT \quad (2.4.7)$$

Unfortunately Garmong numerically evaluated Equation (2.4.7) incorrectly in his 1974 paper (Tyson, 1975). He then published incorrect results which showed the difference in plastic strain during the heat-up and cool-down cycles increased monotonically with increasing fiber volume fraction. An additional error made by Garmong in his 1974 paper was the use of a very large value for yield stress as a

function of temperature for his matrix material (Tyson, 1975). When Tyson submitted a communication which pointed out the errors in the original paper, and proposed a simple incremental method of calculation, he did not recalculate the residual plastic strain in the composite matrix as a function of fiber volume fraction .

Table 2.2 Garmong Model Input Parameters

$\alpha_m - \alpha_f$	= $10 \times 10^{-6} / K$
V_f	= 0.5
E_m	= $6.9 \times 10^4 \text{ MN/m}^2$
E_f	= $2.1 \times 10^5 \text{ MN/m}^2$
σ_0	= $56.0 - 0.07 * T$
K^*	= 690 MN/m^2
n	= 0.5
G	= 2.62×10^4
s	= 4.4
$D_0 A G b / k$	= $3.1 \times 10^{26} / s$
Q/R	= 17,600 K
T_{max}	= 700 K
T_{min}	= 300 K
T_{max} hold time	= 60 seconds

The values in Table 2.2 are very similar to the values for an aluminum matrix SiC reinforced composite. However the difference between the matrix and fiber coefficients of thermal expansion would be about twice as large in the SiC-Al composite as that given in Table 2.2.

Figure 2.1 shows the results of a program which follows the Tyson development of Garmong's Model. These results are for the data listed in Table 2.2, and include the corrected value for matrix yield strength. In his development Garmong did not specifically calculate the thermal cycling deformation of a macroscopic composite solid. His intention was to find the amount of plastic flow occurring in a composite to be used as an indication of fatigue damage development (Garmong, 1974). If one follows the rationale of the macroscopic model of Taya-Mori the residual plastic strain would be multiplied by the matrix volume fraction, f , to find the macroscopic composite strain. This result is included in Figure 2.1.

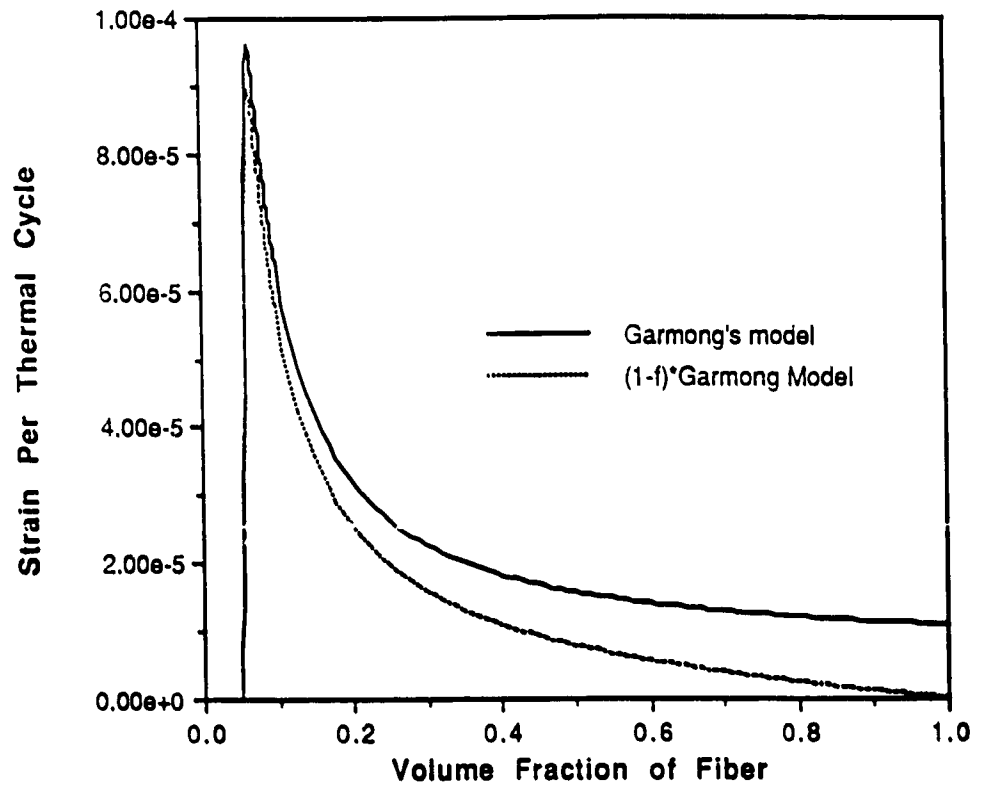


Figure 2.1 Garmong Thermal Cycling Deformation Model Result.

2.4.2 Yoda et al's Model

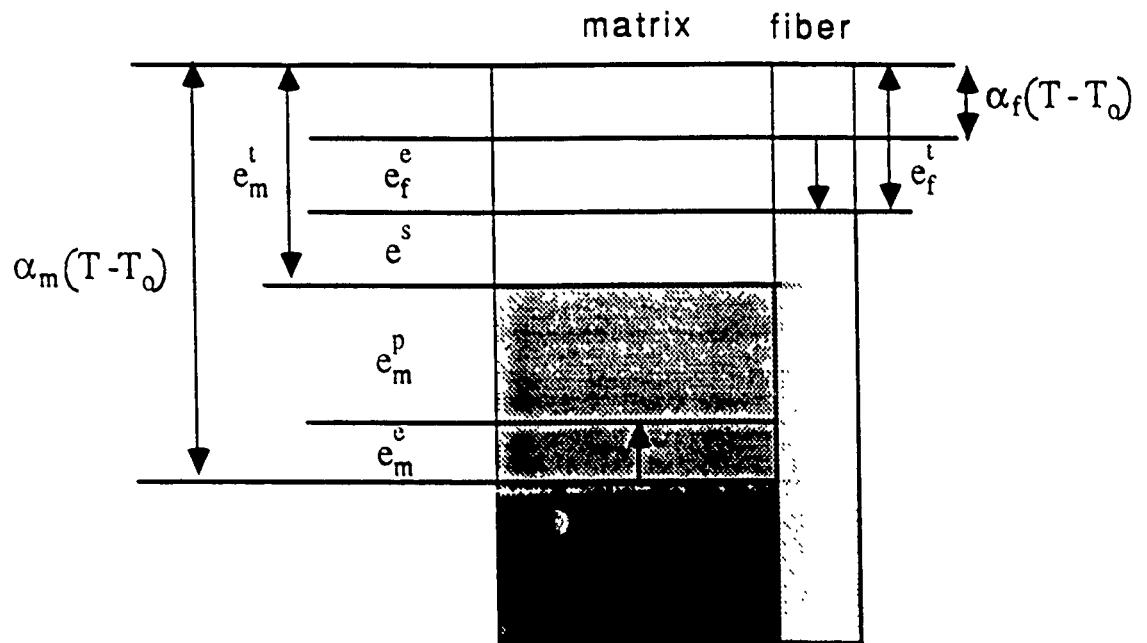


Figure 2.2 Yoda et al Thermal Cycling Deformation Model.

The Yoda et al model considers a uniaxial, continuous composite which is initially unstressed at a certain temperature (Yoda et al, 1978). The composite is reinforced with fibers stiffer and less thermal expansive than the matrix. When the composite is subjected to a temperature decrease of sufficient magnitude the matrix experiences elastic and plastic tensile stresses, while the fiber experiences an elastic compressive stress. The interfacial bond between the fiber and matrix is sufficiently weak as to permit relative motion. The difference between the total strain of the fiber and the total strain of the matrix is labeled e^s , the sliding strain.

$$e_m^t - e_f^t = e^s \quad (2.4.8)$$

The total strains in the individual phases can now be written as

$$e_m^t = \alpha_m (T - T_0) + e_m^e + e_m^p \quad (2.4.9)$$

$$e_f^t = \alpha_f (T - T_0) + e_f^e \quad (2.4.10)$$

Using Hooke's law and stress equilibrium, one finds the stresses in each phase as

$$\sigma_m = - \left(\frac{k}{V_m} \right) \left[(a_m - a_f) (T - T_0) + e_m^p - e^s \right] \quad (2.4.11)$$

$$\sigma_f = \left(\frac{k}{V_f} \right) \left[(a_m - a_f) (T - T_0) + e_m^p - e^s \right] \quad (2.4.12)$$

where

$$k = \frac{V_m V_f E_m E_f}{(V_m E_m + V_f E_f)} \quad (2.4.13)$$

Yoda et al next uses the principle of virtual work for the determination of the unknown $e_m^p - e^s$.

$$\delta W^e + \delta W^p + \delta W^s = 0 \quad (2.4.14)$$

Where the terms can be shown to be equal to

$$\delta W^e = k \left[(a_m - a_f) (T - T_0) + e_m^p - e^s \right] (\delta e_m^p - \delta e^s) \quad (2.4.15)$$

$$\delta W^p = V_m \sigma_0 \left| \delta e_m^p \right| \quad (2.4.16)$$

$$\delta W^s = V_f \left(\frac{l_f}{d_f} \right) \tau^* \delta e^s \quad (2.4.17)$$

During plastic deformation e^p_m varies such that

$$e^p_m - e^s = -(a_m - a_f)(T - T_0) + \left(\frac{V_m}{k} \right) \sigma_0 \quad (2.4.18)$$

During phase-boundary sliding e^s varies such that

$$e^p_m - e^s = -(a_m - a_f)(T - T_0) + \left(\frac{V_f}{k} \right) \frac{l_f}{d_f} \tau^* \quad (2.4.19)$$

Yoda et al next makes the assumption that the phase boundaries are sliding as if the interface is composed of a thin layer of Newtonian fluid.

$$\tau^* = \frac{1}{3} l_f \frac{\mu_0}{h} \left| \dot{e}^s \right| \exp(Q/R T) \quad (2.4.20)$$

where h is the layer thickness, μ_0 is the reference viscosity, Q is the heat of activation, R is the gas constant, and the dot denotes a time derivative. Notice that the interfacial viscosity becomes smaller when the temperature increases.

Substitution of (22) back into (21) yields a first order differential equation in e^s .

$$\beta \dot{e}^s + e^s + \gamma = 0 \quad (2.4.21)$$

where

$$\beta = \frac{1}{3} \left(\frac{V_f}{k} \right) \left(\frac{l_f^2}{d_f} \right) \left(\frac{\mu_0}{h} \right) \exp(Q/R T) \quad (2.4.22a)$$

and

$$\gamma = - \left[(a_m - a_f) (T - T_0) - e_m^p \right] \quad (2.4.22b)$$

Solving this equation Yoda et al finds the heating process interfacial slide strain to be equal to

$$\Delta e_+^s = \frac{V_m}{k} \sigma_0 \left[1 - \exp\left(-t_+/\beta_+\right) \right] \quad (2.4.23)$$

where t_+ is the high temperature residence time, σ_0 is the yield stress of the matrix, and V_m is the volume fraction of the matrix. Since the interfacial viscosity became large at low temperatures Yoda et al considered the low temperature interfacial sliding strain insignificant. Yoda et al also expected the plastic strains due to the cooling process and the heating process to cancel. Therefore, the composite strain per thermal cycle would be dominated by the heating process interfacial sliding strain

$$\Delta e_{\text{cycle}}^s = \Delta e_+^s = \frac{V_m}{k} \sigma_0 \left[1 - \exp\left(-t_+/\beta_+\right) \right] \quad (2.4.24)$$

There are several significant predictions of this model which conflict with the predictions of the Garmong Model. The Yoda model predicts composites with extremely well bonded interfaces will not experience thermal cycling deformation, while the Garmong model predicts a nonzero value. The Yoda model also predicts the amount of thermal cycling strain will increase with increasing high cycle temperature for a given minimum cycle temperature, opposite the trend in the Garmong result. Finally the models agree the thermal cycling strain will increase with decreasing fiber volume fraction. However the Yoda model predicts the thermal cycling strain will become infinite when the volume fraction of fiber is zero, while the Garmong model requires a minimum non-zero value of fiber volume fraction to initiate any thermal cycle strain, and the maximum thermal cycle strain predicted is finite.

Assuming values for the elastic modulus of the matrix, the elastic modulus of the fiber, and having measured the thermal cycling strain per thermal cycle, Yoda et al were able to calculate a matrix yield stress, σ_0 . The σ_0 so calculated seemed reasonable for the particular materials. The strain curve based on this calculation is shown in Figure 2.3. Because of the necessary back-calculation of σ_0 required for this model the results are primarily qualitative in explaining the interfacial slide mechanism.

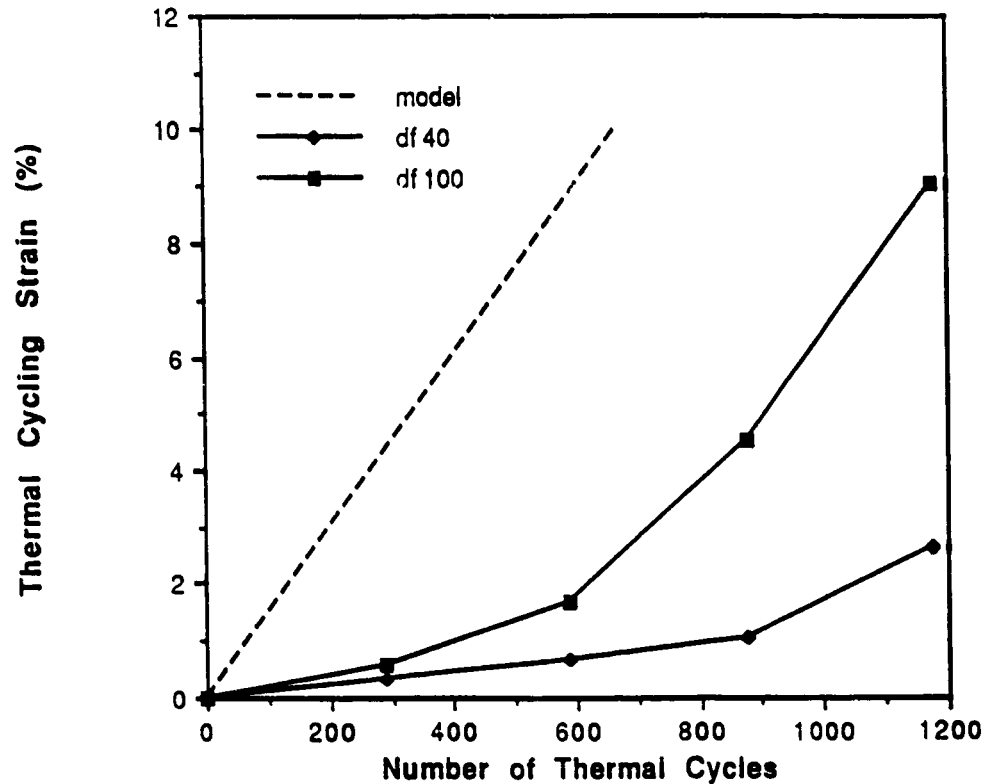


Figure 2.3 Yoda et al Experimental Thermal Cycling Strain Result Compared to Model Prediction.

2.4.3 Taya-Mori's Model

The Taya-Mori thermal cycling deformation model is different from the preceding two models in that the reinforcement may be of arbitrary aspect ratio. The model assumes the interface between the reinforcement and matrix to be perfectly bonded. Figure 2.3 shows the idealized time-temperature history of the composite.

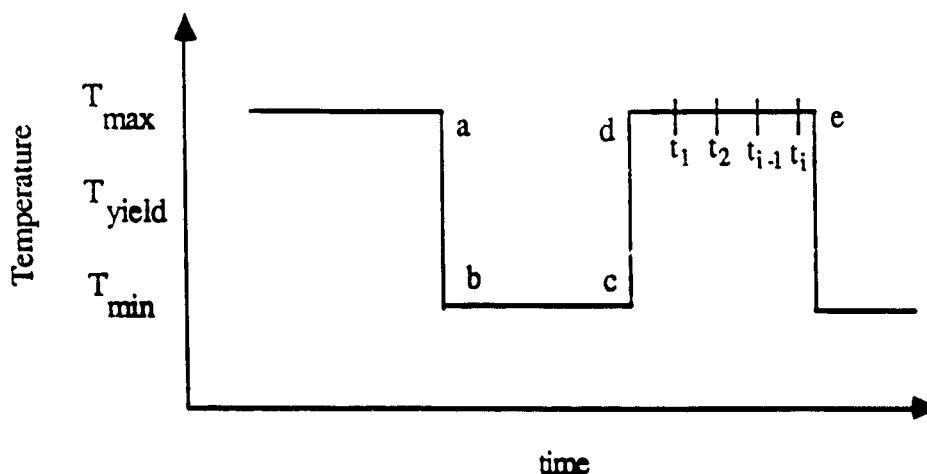


Figure 2.4 Temperature Time Curve for Taya-Mori Thermal Cycling Model

Because the fiber and the matrix have differing coefficients of thermal expansion any change in temperature will result in an average stress and strain in the matrix

$$\overline{\sigma_{D-\Omega}} = C_m \bar{e} \quad (2.4.25)$$

where C_m is the matrix stiffness tensor, and \bar{e} denotes the average strain in the unreinforced domain.

The total strain disturbance field in the composite due to the addition of a single particular fiber is denoted e . This field exists in both the fiber and matrix domains as a function of spatial coordinates and possibly time. The e field is in general the sum of elastic and inelastic strains. α^* denotes the thermal mismatch strain. This uniform strain field exists only in the fiber domain.

Using the above definitions, the stress in the fiber is given by the inner product of the elastic modulus tensor of the fiber and the sum of: the average strain in the composite, the total strain in the composite due to the presence of the fiber, and the negative of the thermal mismatch strain between the fiber and matrix.

$$\sigma = C_f (\bar{e} + e - \alpha^*) \quad (2.4.26)$$

where α^* is given by

$$\alpha^* = (\alpha_f - \alpha_m, \alpha_f - \alpha_m, \alpha_f - \alpha_m, 0, 0, 0) \{T_L - T_H\}$$

Using Eshelby's equivalent inclusion method the fiber is replaced by an equivalent inclusion made of matrix material. This allows the use of the matrix elastic modulus tensor. However a new strain component, e^* , needed to cause the proper transformation strains and thermal strains in the matrix material must be determined. Writing the fiber stress in terms of the matrix stiffness yields;

$$\sigma = C_m (\bar{e} + e - e^*) \quad (2.4.27)$$

Another independent equation is furnished by the definition of the Eshelby tensor S_{ijkl} . This fourth order tensor construction is used to determine the equilibrium strain field within an inclusion when placed within a matrix of like material with a mismatch in strain condition. Now the total strain disturbance due to the presence of the transformed fiber is due to the eigen strain e^* .

$$e = S e^* \quad (2.4.28)$$

The stress in the fiber can now be written as

$$\sigma = C_m \{ \bar{e} + (S - I) e^* \} \quad (2.4.29)$$

or using the fiber elastic modulus tensor

$$\sigma = C_f \{ \bar{e} + S e^* - \alpha \} \quad (2.4.30)$$

Since the internal stress must be self-equilibrating within the composite

$$\int_D \sigma \, dV = 0 \quad (2.4.31)$$

with some derivation one can write

$$\bar{e} + f(e - e^*) = 0 \quad (2.4.32)$$

where f is the volume fraction of fiber. Using equations (2.4.29), (2.4.30), and (2.4.32) we can write

$$C_f \cdot \alpha = (C_f - C_m) \cdot \{ (1 - f) S e^* + f e^* \} + C_m e^* \quad (2.4.33)$$

from which e^* can be computed. Once e^* is found the averaged elastic temperature stress can be found in the matrix and the fiber as

$$\bar{\sigma}_m = -f C_m (S e^* - e^*) \quad (2.4.34 \text{ a})$$

$$\bar{\sigma}_f = (1 - f) C_m (S e^* - e^*) \quad (2.4.34 \text{ b})$$

It is reasonable to expect that if the temperature change is large enough then plastic deformation will occur in the matrix. In order for the matrix to yield the Von Mises yield criterion must be satisfied. The yield stress used in the Von Mises equation is that measured for the minimum cycle temperature.

$$\frac{3}{2} \overline{\sigma_m^{\text{total}}} \overline{\sigma_m^{\text{total}}} = Y^2 \quad (2.4.35)$$

where $\overline{\sigma_m^{\text{total}}}$ at the initiation of yielding is the elastic stress due to temperature change. In the uniaxial composite case the yield criterion can be greatly simplified to

$$\overline{\sigma_3} - \overline{\sigma_1} = Y \quad (2.4.36)$$

Since the average stress deviator is a linear function of ΔT the critical temperature drop at which the average matrix stress meets the yield surface can be easily calculated. The calculation of the plastic strain at T_{\min} requires the definition of two additional quantities: e^{*P} , the eigenstrain associated with plastic deformation; and e^P , the longitudinal plastic strain. Where e^P has the form of

$$\overline{e^P} = e^P \left\{ -\frac{1}{2}, -\frac{1}{2}, 1, 0, 0, 0 \right\} \quad (2.4.37)$$

In an equation similar to equations (2.4.29) and (2.4.30) one can find the stress due to the plastic strain in the fiber in terms of the matrix or fiber stiffness tensors.

$$C_f \left\{ -f \left[S e^{*P} - e^{*P} \right] + S e^{*P} + e^{*P} \right\} = C_m \left\{ -f \left[S e^{*P} - e^{*P} \right] + S e^{*P} - e^{*P} \right\} \quad (2.4.38)$$

Equation (2.4.38) is solved explicitly for e^{*P} in terms of e^P . This result is substituted in an equation completely analogous to equation (2.4.34a).

$$\overline{\sigma}^P = -f C_m \left\{ S e^{*P} - e^{*P} \right\} \quad (2.4.39)$$

This result is used in the yield function definition

$$\left\{ \overline{\sigma}_3 + \overline{\sigma}_3 \right\} - \left\{ \overline{\sigma}_1 + \overline{\sigma}_1 \right\} = Y \quad (2.4.40)$$

Using the above substitutions equation (2.4.40) is then solved explicitly for e^P .

When the composite is heated from point c to point d in Figure 2.3 the negative of the elastic thermal stress are imposed. The stress state at point d is then equal to the stresses due to plastic strain calculated in Equation (2.4.39). These stresses will in general relax by creep. To calculate the creep behavior the incremental Dorn Creep Law is used.

$$\Delta e^c(t_j) = - \left\{ A \left(\frac{\sigma_m(t_{j-1})}{G} \right)^n \frac{G b D_o}{(\kappa T_H)} \exp \frac{-Q_v}{R T_H} \right\} \Delta t \quad (2.4.41)$$

A fictitious eigenstrain can be calculated from this incremental creep strain by

$$C_m \cdot \Delta e^c = (C_f - C_m) \cdot \left\{ (1-f) S e^{*} + f e^{*} \right\} + C_m e^{*} \quad (2.4.42)$$

where

$$\overline{\Delta e^c} = \left\{ \frac{-\Delta e^c(t_0)}{2}, \frac{-\Delta e^c(t_0)}{2}, e^c(t_0), 0, 0, 0 \right\}$$

The incremental stress response is now found in the x_3 and x_1 directions using

$$\Delta\sigma_m(t_1) = -f C_m \cdot (S e^* - e^*) \quad (2.4.43)$$

The incremental flow stress is now calculated and added to the flow stress at the start of the cycle increment, the incremental creep strain is added to the existing creep strain. The process is repeated until the finish of the high temperature residence time. Also during this time diffusional relaxation occurs at the composite interfaces. In this process matrix material which occupies locations on the interface with compressive tractions migrates to locations on the interface with tensile tractions. The severity of this interfacial diffusion mass transport is assumed sufficient to reduce the stress in the fiber to a hydrostatic state. That is

$$\langle \sigma_{11}^p \rangle_f + \langle \sigma_{11}^c \rangle_f + \langle \sigma_{11}^d \rangle_f = \langle \sigma_{33}^p \rangle_f + \langle \sigma_{33}^c \rangle_f + \langle \sigma_{33}^d \rangle_f \quad (2.4.44)$$

From Equation (22) the strain due to diffusion e^d is solved as

$$e^d = e^p + e^c \quad (2.4.45)$$

The macroscopic strain due to e^d is equal to the fiber volume fraction of the composite times e^d . The resulting macroscopic longitudinal strain for the composite for the entire thermal cycle is then

$$\langle e_L \rangle = (e_p + e_c) \quad (2.4.46)$$

While the transverse strain is given by

$$\langle e_T \rangle = -\frac{(e_p + e_c)}{2} \quad (2.4.47)$$

Figure 2.5 shows the results of this model for the material properties and thermal cycling conditions given in Table 2.3. This data was chosen to closely approximate the input parameters of the Garmong Model. The Taya-Mori results are in this case very close to the Garmong result. As was the case in the Garmong model without the matrix volume fraction multiplication, the Taya-Mori result has a nonzero strain per thermal cycle at a fiber volume fraction of one.

Table 2.3 Taya-Mori Model Input Parameters

α_m	= 24.7 x 10 ⁻⁶ / K
α_f	= 14.7 x 10 ⁻⁶ / K
v_f	= 0.33
v_m	= 0.17
V_f	= 0.5
E_m	= 6.9 x 10 ⁴ MN/m ²
E_f	= 2.1 x 10 ⁵ MN/m ²
σ_0 T _{min}	= 35 MN/m ²
G	= 2.62 x 10 ⁴
s	= 4.4
D_0AGb/k	= 3.1 x 10 ²⁶ /s
Q/R	= 17,600 K
T_{max}	= 700 K
T_{min}	= 300 K
T_{max} hold time = 60 seconds	

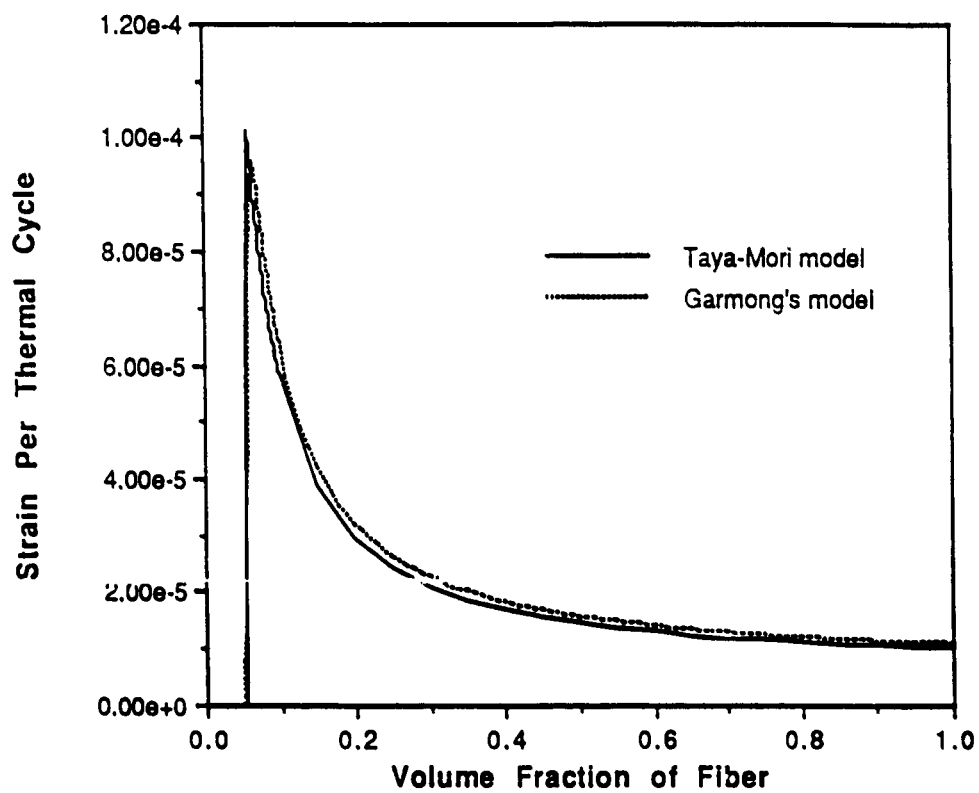


Figure 2.5 Taya-Mori Thermal Cycling Deformation Model Result.

Chapter 3 Test Specimen Processing

3.1 Material Production

3.1.1 Fiber Processing

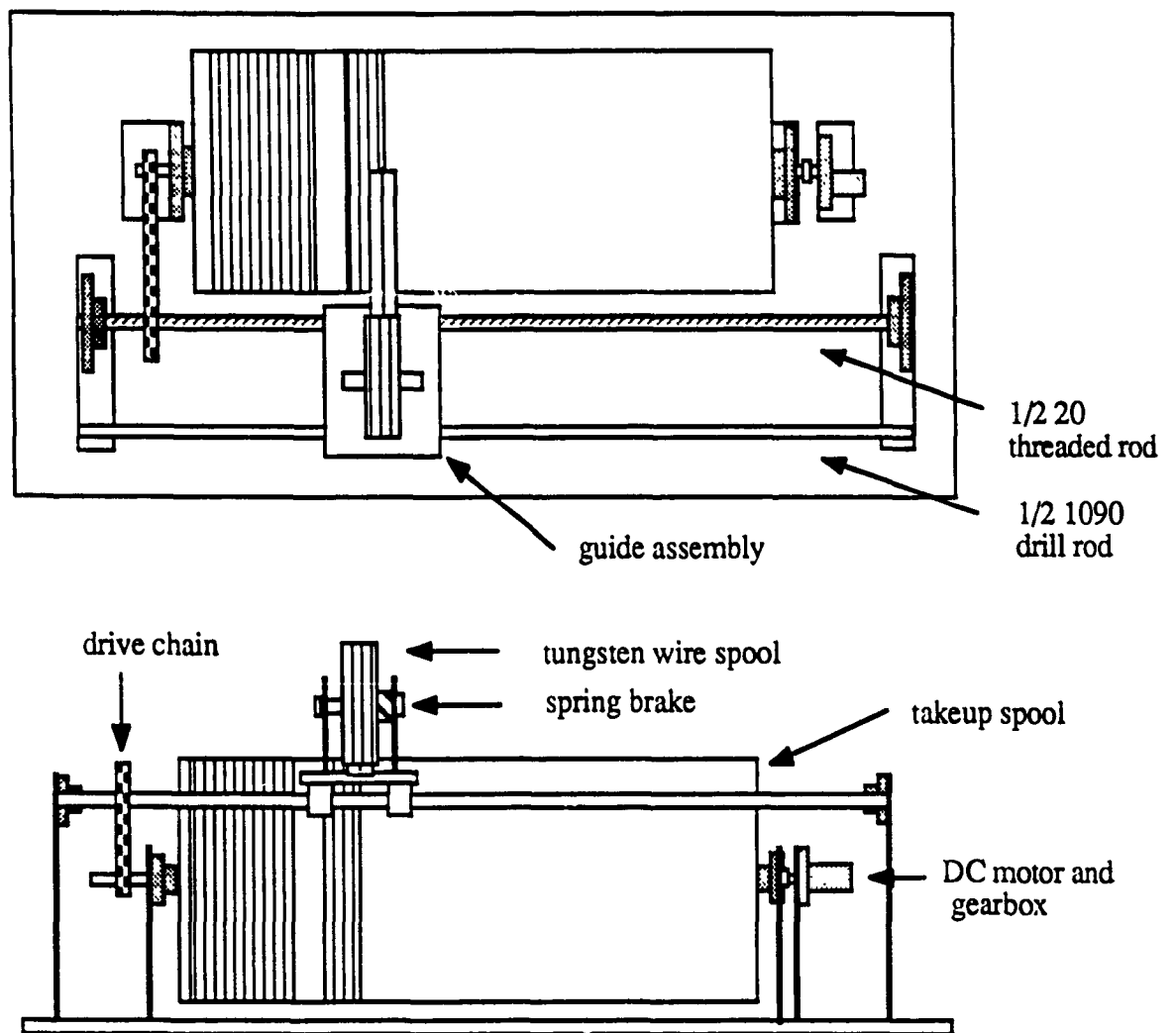


Figure 3.1. Filament Winding Machine

The tungsten fiber material was originally received as 250 micron diameter wire manufactured to ASTM specification F288-81. It was purchased from both the General Electric company and the Thermeonix Products company.

The tungsten wire was processed into an aligned form with a specially built Filament Winding Machine. This device is shown in Figure 3.1. The power for the machine is supplied to the take-up drum by a small electric motor and gearbox. The guide assembly is laterally advanced by a threaded rod rotated by a drive chain connected to the take-up drum. Heavy bearings and lateral reinforcement were used to ensure accurate fiber positioning. The machine take-up drum rotates at fifteen rpm for a linear take-up rate of 2,350 feet per hour. By switching gears in the guide assembly the lateral spacing of the tungsten wire can be adjusted to 60, 40, 30, 13.3, or 6.7 fiber lines per lateral inch. After the fiber was wound on the machine a thin coating of Duco cement was brushed on and allowed to dry. The fibers were cut along a gap in the take-up drum covering and then removed as 4.5 inch wide by 30 inch long fiber mats.

In the case of continuous fiber, the produced mats were sheared laterally into 2.79 cm long, 11.43 cm wide aligned fiber tapes retaining the polymer cement binder. Later these tapes were stacked with the matrix material into a composite preform. In the case of the aligned short fibers the fiber mats were sheared laterally into lengths of 5 mm and 1.25 mm then the duco cement was removed with alternating baths of acetone and water. The individual short fibers were then aligned with a special tool and stacked with the matrix material.

3.1.2 Matrix Processing

The matrix material was received as a 15 micron nominal diameter powder. In order to fashion this powder into a form useful for composite fabrication a tape casting processing method originally developed by Sue Perrick in the Materials Science Department at the University of Washington was employed.

In the tape casting processing method 12 grams of Butvar + B79 resin polymer flakes were dissolved in 250 cc's of toluene. Six grams of Santicizer 160 polymer plasticizer was added and the mixture was well stirred. Both the Butvar and Santicizer materials were produced by the Monsanto Corporation. 400 grams of metal powder was then added and stirred vigorously for 15 minutes. The resultant mixture was poured onto an 18 inch wide by 18 inch long smooth Teflon sheet. The mixture was placed under a ventilation hood. After approximately four hours the toluene evaporated leaving a tough pliable powder cloth consisting of a high volume percent of metal powder particles entrained in a firm polymer network. The powder cloth was sliced into 4.5 by 4.5 inch sheets and removed from the Teflon assembly with a 5 inch wide putty knife. The resulting powder cloths were then stacked with the correct arrangement of fibers to make the composite preforms.

The production of the AF hybrid composite differed only in the inclusion of 10 volume percent of hand ground Al_2O_3 fibers. The Al_2O_3 fibers had a nominal diameter of 19 micron and were produced by Dupont.

3.1.3 Composite Assembly

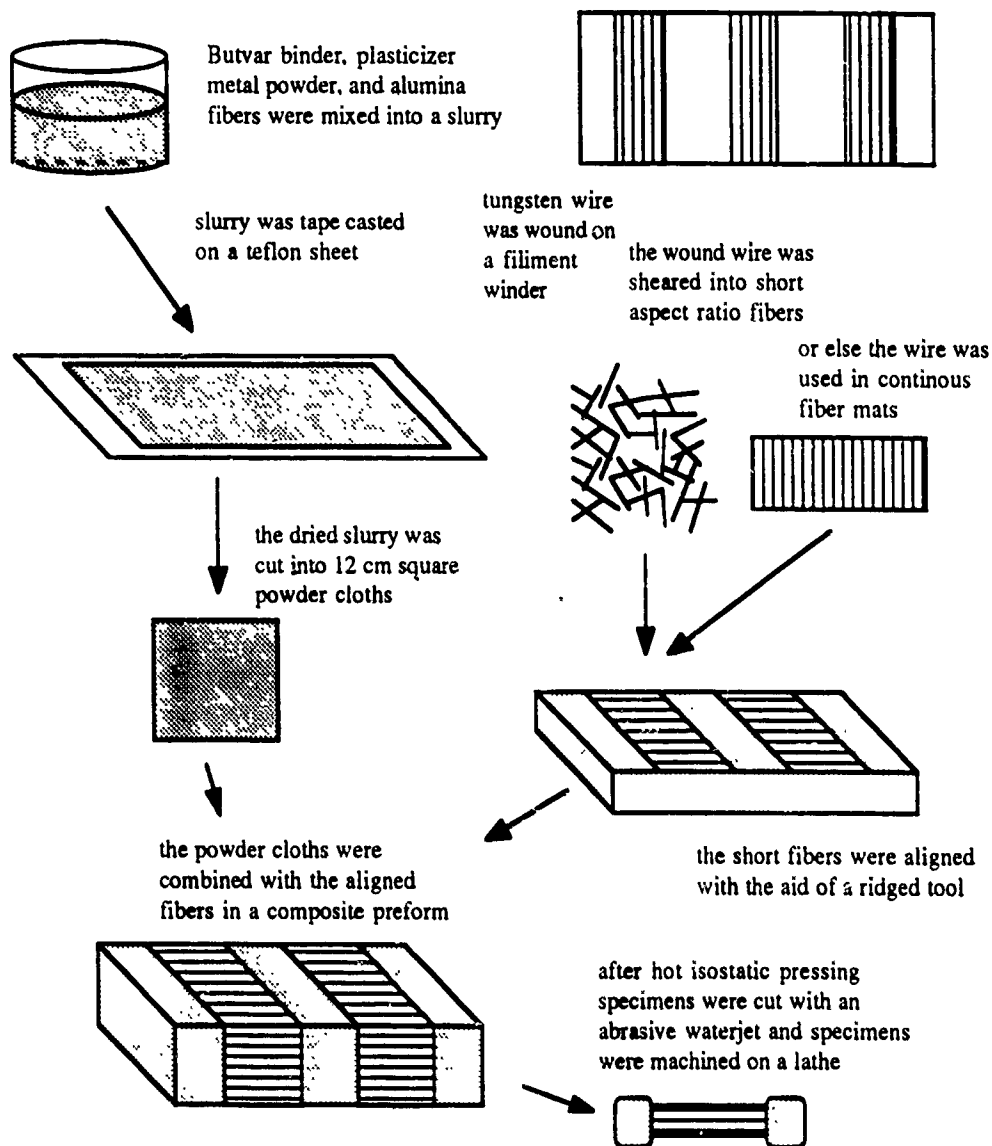


Figure 3.2 Composite Specimen Fabrication.

In the composite assembly process matrix and fiber materials were brought together to form a composite preform. The preform assembly method was different for the continuous fiber case than for the aligned short fiber case. In both cases the 4.5 inch wide by 4.5 inch long preform contained aligned reinforcement fibers in two 1.1 inch long parallel zones. This arrangement was chosen so that two specimens could be

machined from a longitudinal slice of the resulting billets both having unreinforced grip sections. Reinforced grip sections were considered undesirable due to the increased difficulty in machining.

In the continuous fiber case the 1.1 inch long 4.5 inch wide aligned fiber tapes were stacked in the two reinforcement zones between powder cloths. A section of powder cloth was used in every second layer to fill in between the fiber reinforced zones so that the reinforced zones did not become thicker than the unreinforced zones. The resulting preform typically used 32 powder cloth sheets and 18 layers of aligned continuous fibers.

In the aligned short fiber cases an alignment tool was made by forming a sculpting compound into a five inch square flat plate, after which a 1/2-13 threaded rod was drawn across the plate to produce a set of parallel v-notch grooves. After hardening the fiber free zones in the composite were cut into deep smooth channels. Then during preform assembly 20 grams of tungsten fibers were evenly distributed within the alignment tool grooves. Next a powder cloth was placed over the fiber filled alignment tool backed by a support made with a plastic foam pad attached to an aluminum plate. The set up was then inverted and the support removed. At this point the powder cloth lay covered with many aligned short fibers in the two reinforcement zones. The powder cloth was then sprayed with an adhesive and stacked. Again in this case it was necessary to occasionally place a section of powder cloth in the unreinforced zones.

In addition to the composite material a monolithic FeCrAlY preform was produced using only metal powder cloths.

3.1.4 Polymer Burn-off

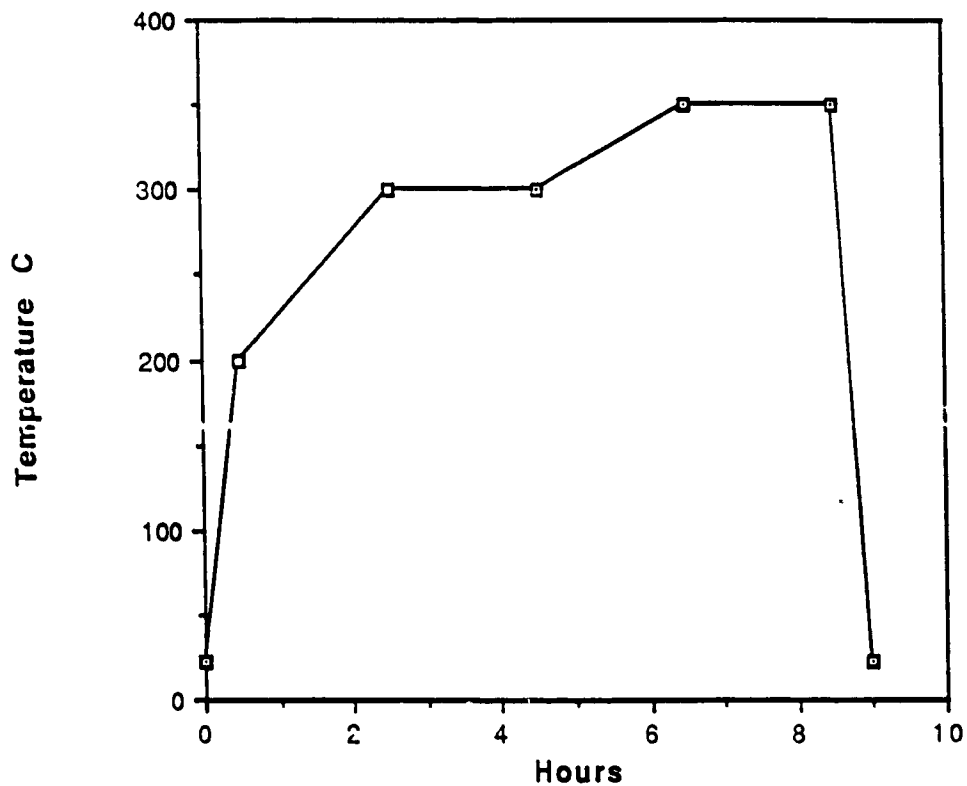


Figure 3.3 Burn-off Time Temperature Schedule.

A polymer burn-off operation is necessary to remove the various polymer materials used in the creation of the composite preforms. During this burn-off operation two important processes which affect the eventual composite quality may be active. The desirable process is the diffusion and reaction of atmospheric oxygen with the polymer material producing CO_2 and H_2O gaseous reaction products. The undesirable competing process is the pyrolyzation of the polymer material by off-gassing volatiles. A badly executed pyrolyzation process can create a dense

carbonaceous mass requiring much higher temperatures to remove. These higher temperatures may not be possible since damaging oxidation will occur in the matrix powder. Therefore the burn-off procedure must be carefully chosen and in this study it proved to be the most difficult and sensitive processing operation.

In order to get some experience with the specific materials used in this study a number of trial burn-off procedures were performed. It was found that if temperatures were held below 300 C the rate of oxidation of the metal powder was negligible, however the combustion of the polymer was not completed. At 350 C the metal oxidation became more significant but the polymer was fully removed. Therefore the routine used for the composite preforms was a rapid temperature climb to 200 C followed by a slow two hour ramp to 300 C. The temperature was then held at 300 C for two hours after which the temperature was ramped over two hours to 350 C and then rapidly cooled to room temperature. The entire burn-off procedure required approximately 9 hours. The resulting composite compact was of high quality and quite clean.

3.1.5 Hot Isostatic Press Processing

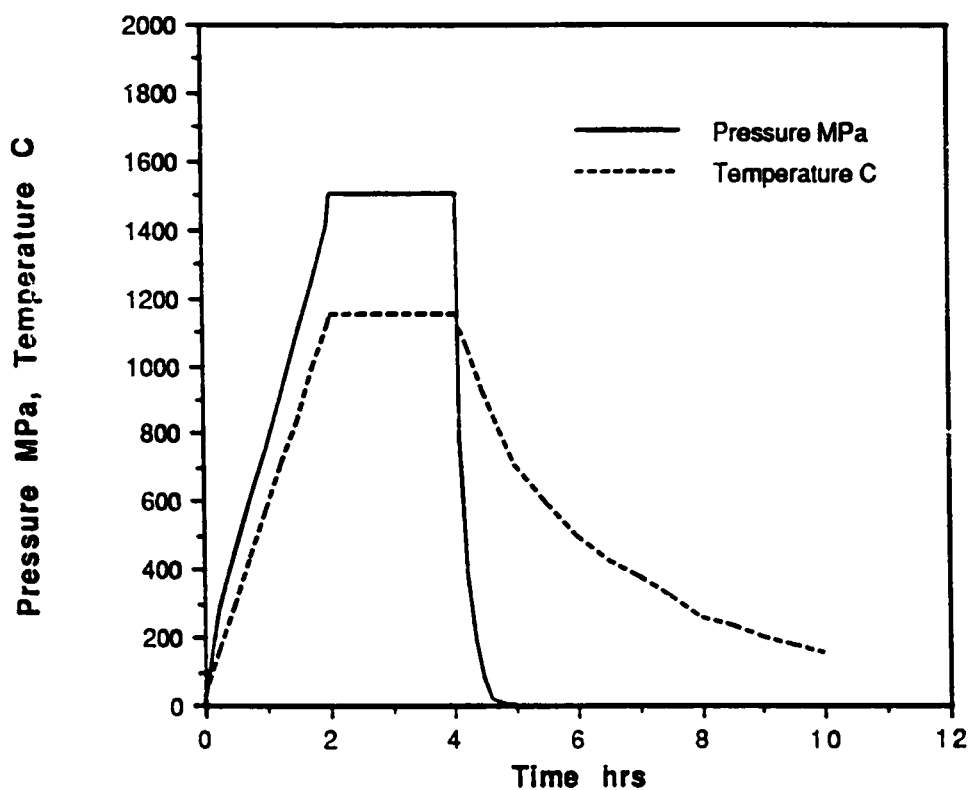


Figure 3.4 Hot Isostatic Press Time Temperature Pressure Schedule.

During a Hot Isostatic Press (HIP) operation high temperatures and large hydrostatic pressures are applied to a powder metallurgy product sealed in an evacuated canister. The high temperatures and pressures enable the creation of highly consolidated materials with diffusion processes.

The particular HIP schedule used for the material in this study is a modification of that developed by T. Morimoto. In the chosen process, the temperature and pressure

rose to 1150 C and 1500 MPa in two hours. These conditions were held for two hours after which the pressure was rapidly released. The temperature was then allowed to slowly decay over night. The temperature was released slowly so as to allow creep and diffusion processes to relax internal stresses for as long as possible during cool-down.

3.2 Specimen Fabrication

The thermal cycling test specimens were fabricated by machining processes. Specimen blanks were made by cutting the as-HIPed composite billets with an abrasive water-jet. These blanks were then turned on an lathe with tungsten carbide tools.

3.2.1 Abrasive Water-jet Cutting

The abrasive water-jet cutting method entrains hard granular solids in a focused supersonic water flow. This method is gaining increasing industrial use because of its ability to easily cut materials for which cutting has otherwise been difficult or expensive. The selection of water-jet cutting was necessitated in this particular study by the difficulty inherent in machining the W-FeCrAlY composite system. Diamond sawing had proven to be extremely slow with high blade wear because of the metal matrix, while conventional power hacksawing was unsuccessful because of the hard reinforcement.

The abrasive water-jet machine had a high pressure pump which supplied 241 MPa water to a chamber. The outlet of this chamber was a special sapphire with a smooth 0.33 mm wide hole. Downstream of this hole the water velocity was supersonic. Abrasive particles were entrained in this flow which then passed through a silicon carbide nozzle with a 1.1 mm diameter orifice. The exit flow from this nozzle was well collimated for approximately 2 cm.

The feed rate for cutting the test material was 1.52 cm per minute. The cutter then used 316 grams per minute of 100 grit garnet abrasive. With these cutting conditions four 11.5 cm long cuts were completed every hour using 0.5 kg of abrasive per cut. Usually six specimen blanks, each blank producing two specimens, were cut from each billet.

3.2.2 Specimen Machining

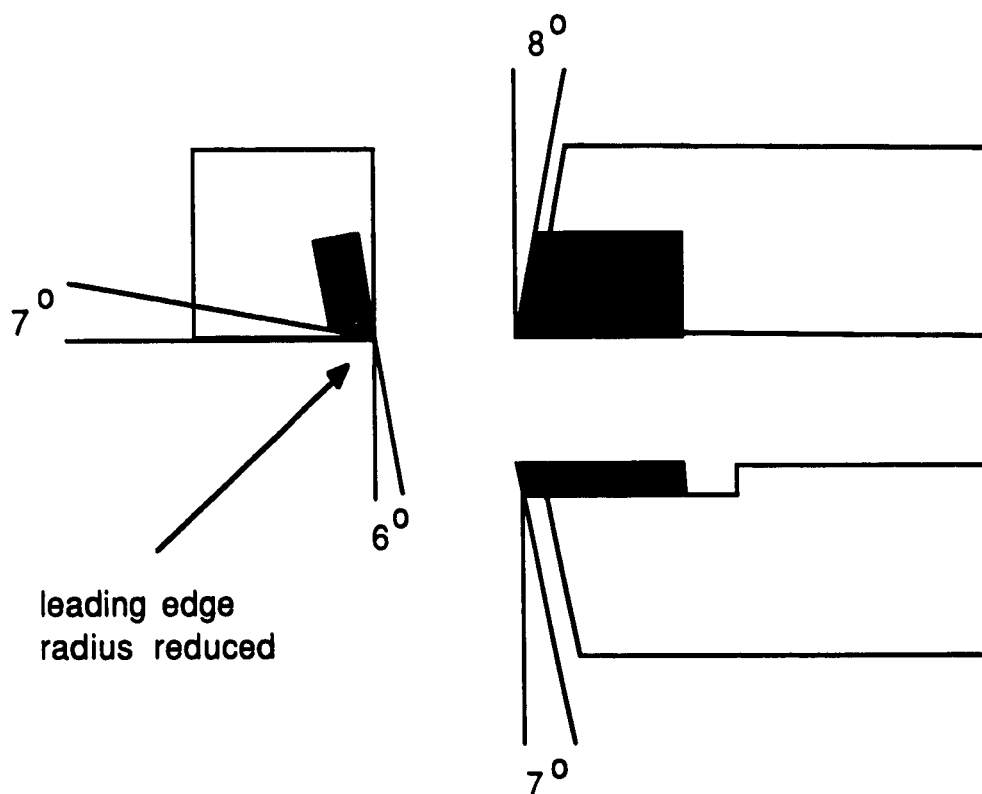


Figure 3.5 Tungsten Carbide Cutting Tool Geometry.

The specimen blanks were turned on a lathe. Turning was selected as the primary specimen fabrication method because of its desirable economics. Additionally the method was expected to provide specimen surfaces well suited for thermal spray attachment.

The specific cutting tools used for the specimens were several DO-ALL DO-2, AR-6 tungsten carbide single point turning tools. The tools had been modified by reducing the leading edge. The DO-ALL catalog quotes a Rockwell C hardness of 92.0 and a transverse rupture strength of 2.240 GPa for this tool. Using these tools the specimens were machined at 125 rpm. The depth of roughing cut was 0.635 mm

while the feed was 40.6 micron per revolution. All cutting was performed dry. A particular cutting tool usually lasted for only 500 linear meters before resharping was necessary.

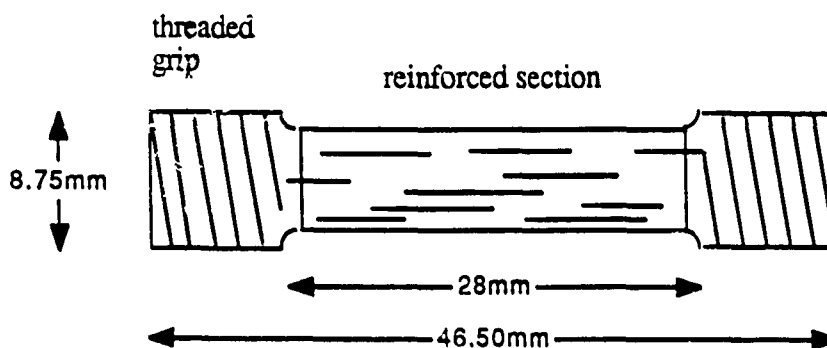


Figure 3.6 Machined Thermal Cycling Test Specimen.

3.2.3 Specimen Coating

A thermal spray coating was used to protect the tungsten reinforcement at the machined surface of the specimens from high temperature oxidation. The thermal spray application was particularly simple in this case since the specific metal powder which was used for the matrix was also used for the thermal spray coating. It was considered desirable for the thermal spray layer to be deposited in such a way as to produce a microporous structure since the reduction in spray layer stiffness would make the coating more thermal cycling resistant and better able to accommodate large specimen strains. However, the porosity could not become interconnected or the layer would have a high oxygen transport.

The specimens were thermal sprayed at Flame Spray Northwest, a small shop located in Seattle, Washington. The specimens were first prepared for thermal spraying by a 35 mesh garnet grit sandblast. The material was then applied with a Bay State Plasma gun using a 50 psi working and powder flow pressure, 600 amps, and 30 volts. The finished coatings were nominally 0.2 mm thick.

3.3 Initial Specimen Characteristics

3.3.1 Volume Fraction of Reinforcement

The volume fraction of tungsten reinforcement in the various composite types were determined using density measurements. The density specimens were produced by cutting off the unreinforced sections of the as-coated specimens. These cylindrical density specimens were then put into a lathe and the thermal spray coating was removed with emery cloth, after which the specimen ends were ground square.

The mass of the specimens were measured in a precision pan balance reproducible to 0.01 gram. The length and diameter of the cylindrical specimens were measured with a micrometer. The density of the matrix was found experimentally as 6.87 gm/cm^3 . This result includes the presence of matrix porosity. The density of the matrix for the AF hybrid case was calculated from the weight percent of Al_2O_3 in the initial mixture and a Al_2O_3 specific gravity of 3.73 gm/cm^3 . The density of W-1% ThO_2 was found in the literature as 18.98 (Snow and Dunham, 1975). Using this information the results shown in Table 3.1 were obtained.

Table 3.1 Produced Composite Materials

<u>material</u>	<u>fiber aspect ratio</u>	<u>tungsten volume percent</u>	<u>Al_2O_3 volume percent</u>
CF	infinite	31.9%	0.0
ASF-20	20	19.5%	0.0
AF	20	18.4%	10.0
ASF-5	5	19.4%	0.0

Chapter 4 Thermal-Mechanical Testing

4.1 Tensile Testing

4.1.1 Tensile Test Apparatus and Procedures

Tensile testing was performed on a set of uncycled specimens to determine the basic mechanical behavior of the W-1%ThO₂ reinforced FeCrAlY material. The test specimens included a monolithic FeCrAlY specimen which had been processed along with the composite material. In order to tensile test the specimens it was necessary to reduce the specimen diameter to 4.45 mm. If the diameter was not decreased the tensile failure occurred in the unreinforced threaded grips rather than the reinforced test section.

The specimens were tested at room temperature with a MTS hydraulic testing machine under load control. The uniform stress rate was approximately 100 MPa per minute. The strain in the specimens was determined with two strain gauges connected in series with two temperature compensation gauges so as to cancel both bending strains and heat errors. The strain gauges used were Micro Measurements EA-06-125BT-120 with a gauge length of 3 mm and a gauge width of 1.4 mm.

4.1.2 Room Temperature Tensile Test Results

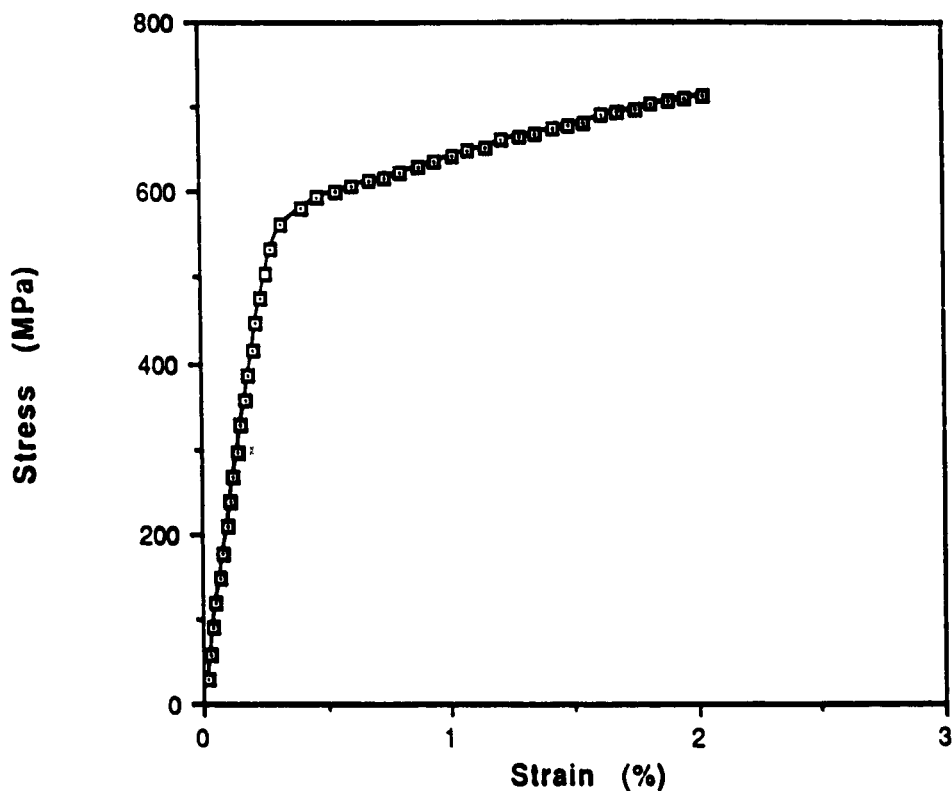


Figure 4.1 FeCrAlY Matrix Stress Strain Diagram.

Figure 4.1 shows the results of a room temperature tensile test on the monolithic FeCrAlY specimen. The modulus was found to be 210 GPa. The 0.2% offset stress was found to be 590 MPa. The tensile specimen fractured at only 2.1% engineering strain.

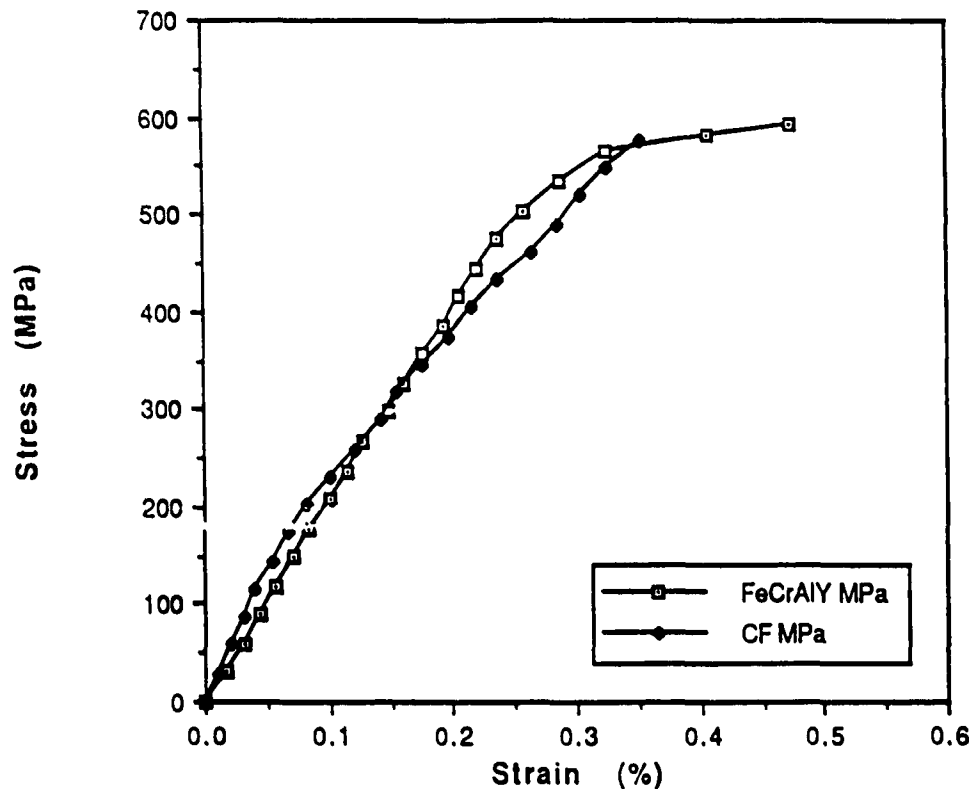


Figure 4.2 FeCrAlY CF Comparative Stress Strain Diagram.

Figure 4.2 compares the tensile results of the monolithic FeCrAlY matrix with the 31.9 volume fraction W-1%ThO₂ reinforced FeCrAlY matrix continuous fiber composite. The initial stiffness of the composite is greater than that of the monolithic metal. Calculating a linear regression on the first four composite data points yields a elastic modulus of approximately 280 GPa. Assuming a fiber elastic modulus of 358 GPa, and then using the previously determined matrix elastic stiffness of 210 GPa with a fiber volume fraction of 31.9 yields a calculated rule of mixtures elastic modulus result of 259 GPa. When linear regression was applied to the last four composite data points the modulus was found to be 128 GPa. This result is close to

the product of the volume fraction of the fiber times the stiffness of the fiber, 114.2 GPa. These would be the expected results for a composite which experiences accelerated matrix yielding due to the presence of significant thermal residual stresses.

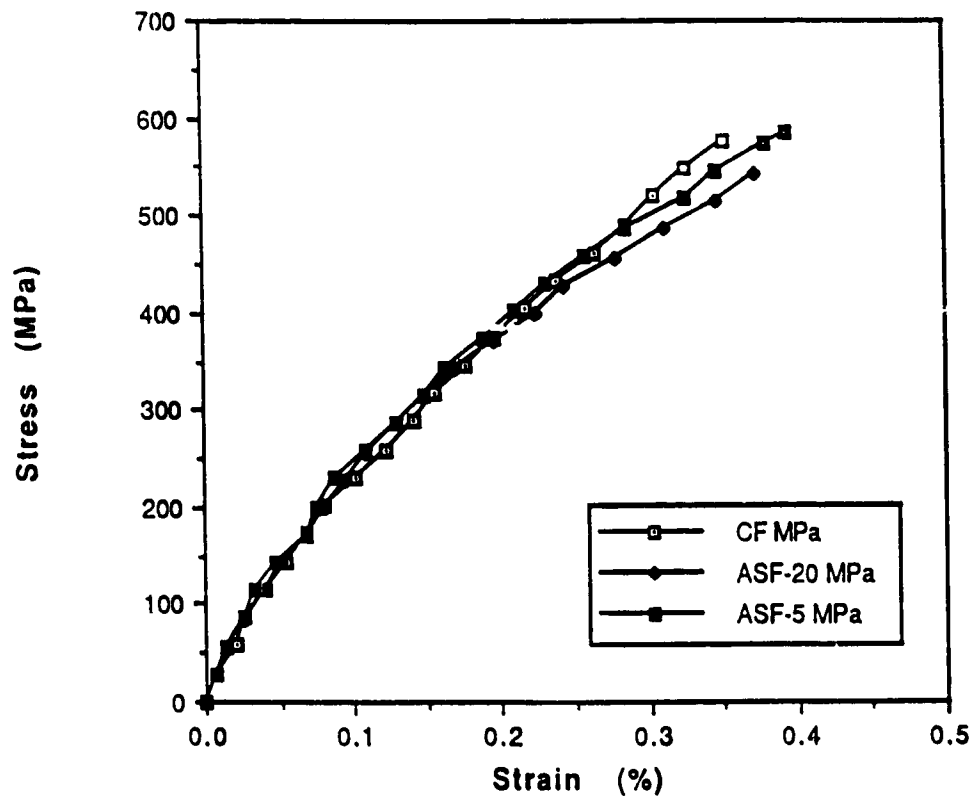


Figure 4.3 Composite Stress Strain Diagram.

Figure 4.3 shows the remarkable similarity in tensile results for the three nonhybrid composite specimens. This result is in contrast to the tensile comparison between the AF and ASF-20 specimens show in Figure 4.4. In this case the 10 volume percent Al_2O_3 reinforced hybrid shows a measurably superior performance. While the AF specimen is stiffer, the final moduli of the AF and ASF-20 are quite similar. This

result would be consistent with both specimens having extensive matrix plastic flow with the AF specimen having a higher flow stress due to the inclusion of the Al_2O_3 ground fibers.

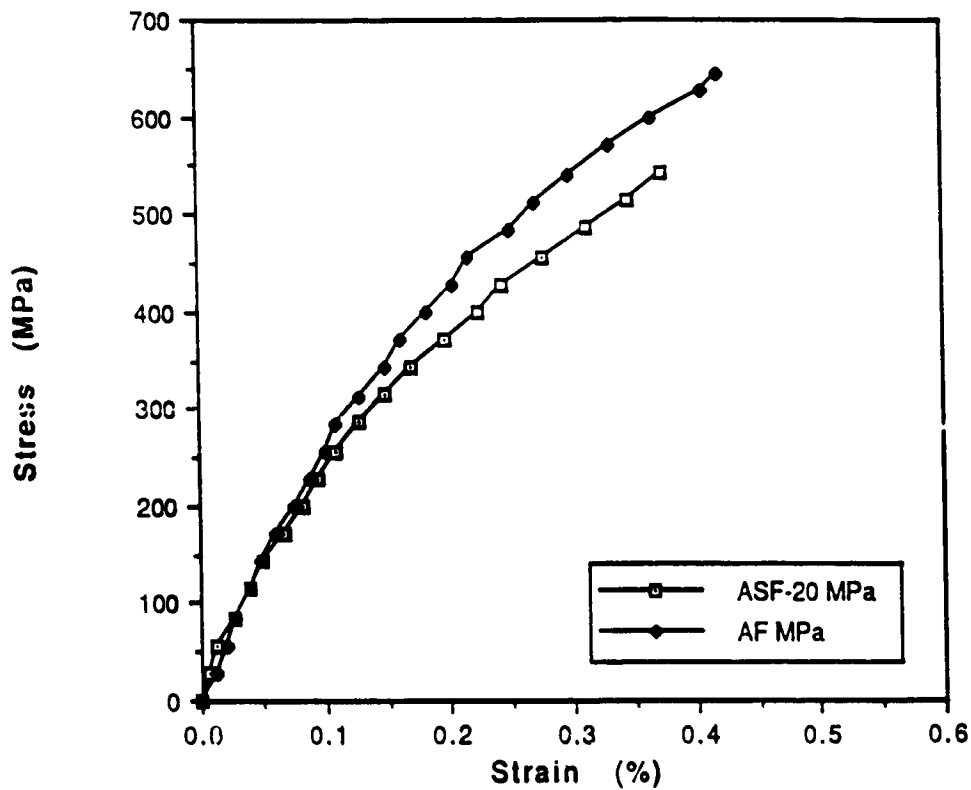


Figure 4.4 Comparative Stress Strain Diagram, ASF-20, AF.

4.2 Thermal Cycling Testing

4.2.1 Thermal Cycling Test Apparatus and Procedures

After fabrication, the thermal sprayed specimens were made ready for thermal cycling testing by inspection for cracks, thermal spray spalls, non-coated locations, and end asperities. The specimens were then measured in length and diameter. The length measurement was performed with a calibrated two inch micrometer. The specimen was placed in the measurement section of the micrometer and gently rotated and translated until a minimum reading was established. This seating procedure was performed several times until a consistent result was determined. This procedure was quite sensitive to the presence of any protruding asperities on the specimen end face. If such an asperity were found it was removed with sand paper and the seating procedure was performed again. Due to the quality of the initial machining the specimen end faces were uniformly normal to the specimen longitudinal axes. The specimens were measured in lateral diameter at the specimen longitudinal midsection. To make this measurement a calibrated one inch micrometer was positioned at the specimen midsection and the specimen was rotated while the micrometer reading was reduced. This procedure was done several times to arrive at a stable value. The procedure was sensitive to the presence of thermal spray irregularities since the micrometer would bind on the relatively thick coating locations.

After the inspection and measurement procedures were completed a set of samples were exposed to thermal cycling conditions in the Metallurgical Thermal Cycler.

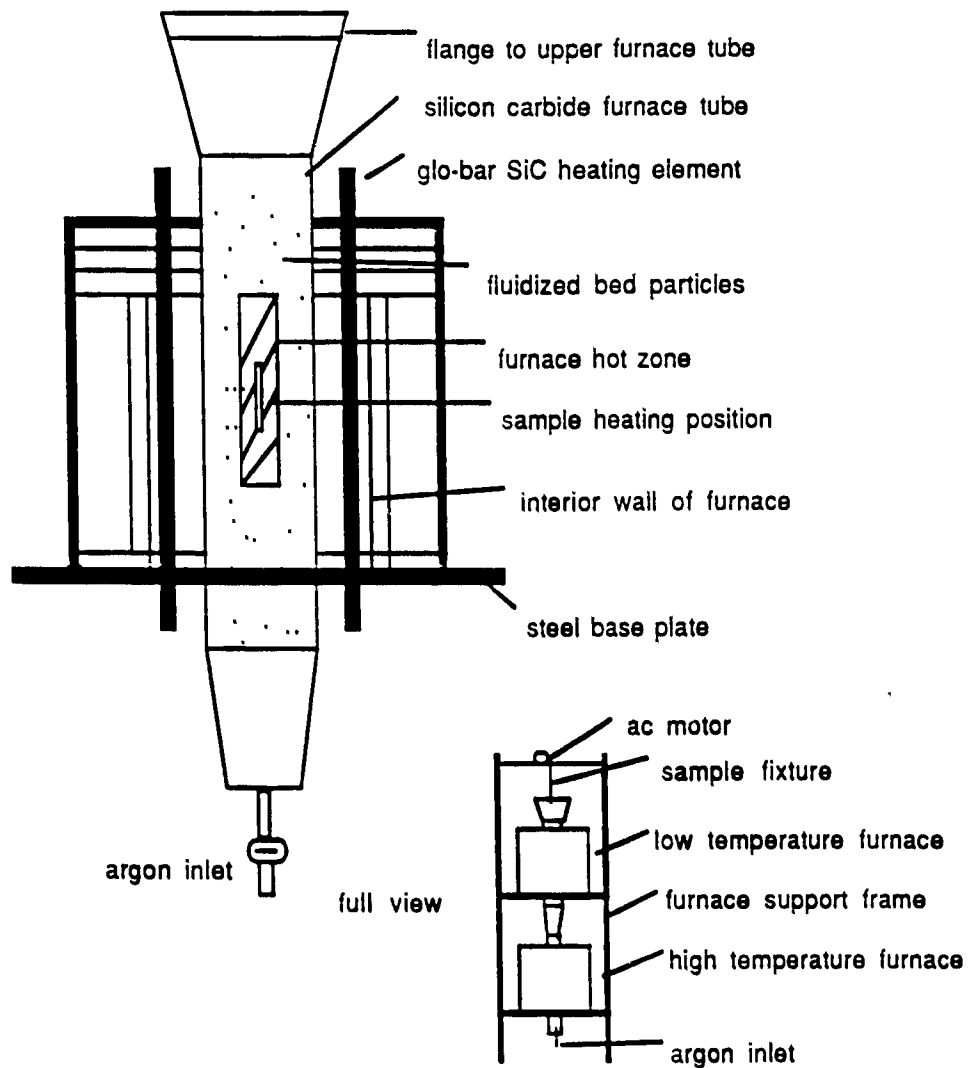


Figure 4.5. Metallurgical Thermal Cycler.

The Metallurgical Thermal Cycler was built to thermal cycle metal matrix composite sheets in air. The maximum width of sheet the machine can accommodate is nine centimeters. The thermal cycler may also be used for thermal cycling ceramic specimens, isothermal exposure tests, and high temperature material processing.

The maximum operating temperature of the high temperature furnace is 1400 C, the maximum operating temperature of the low temperature furnace is 850 C, and the minimum controllable set point temperature for both furnaces is presently 500 C. In

the current configuration radiation heat transfer dominates in the high temperature furnace while convective heat transfer dominates in the low temperature furnace.

The specimens are shuttled from high to low hot sections by a dc motor connected to a timer and a switching circuit. The residence time at each furnace can be set as some even divisor of 30 minutes with the minimum residence time equal to six minutes. The motor can shuttle up to five pound samples from one furnace hot zone to the other in 10 seconds. During the shuttle the specimen remains enclosed by the silicon carbide furnace tubes and the stainless steel connecting flanges. The presence of the flanges minimizes the shock cooling between furnaces.

The furnaces themselves are heated by silicon carbide resistance elements connected in series. The globars have an eight inch hot section. There are six globars in the high temperature furnace and eight globars in the cooler furnace.

The furnaces are insulated with high temperature insulating blanket, the characteristics of the blanket are such that at temperatures in excess of 1350 C the insulation will sinter. This will with time require the replacement of the insulation.

The furnaces are supported by a steel frame which is made from half inch steel plate and one inch threaded rod. The overall height of the frame is 12.5 feet.

4.2.2 Creep Thermal Cycling Machine

The Creep Thermal Cycling Machine was built to thermal cycle metal matrix composite specimens in air (Armstrong and Taya, 1990). The machine subjects the stationary specimen to a thermal cycle by reciprocating two constant temperature furnaces. The machine is able to provide a 2270 kg tensile dead load and a maximum specimen temperature of 1400 C. Figure 4.6 shows the basic configuration of the machine.

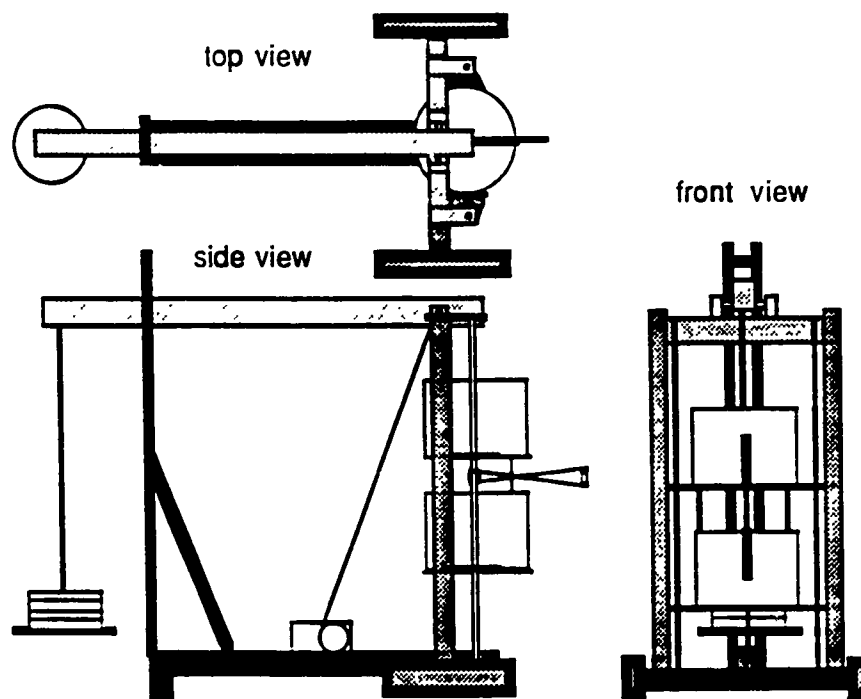


Figure 4.6 Creep Thermal Cycling Machine.

The machine supplies the tensile load to the specimen with a loading lever reacting against a load frame. These parts are primarily constructed of 10.2 cm by 5.2 cm by 6.35 mm wall thickness A500 grade steel rectangular tube. During testing the specimen grips and connecting rods are periodically exposed to high temperatures. Therefore, the specimen grips are constructed of iron based superalloy, while the less severely exposed connecting rods are constructed of stainless steel. Both are heavily

insulated with a thick layer of high temperature blanket. This blanket protects the load train materials from high temperature oxidation and creep while at the same time reducing the power demanded to keep the off duty furnace at its set temperature. The insulating blanket also serves a further function of preventing the metal grips from shorting out the furnace power circuit.

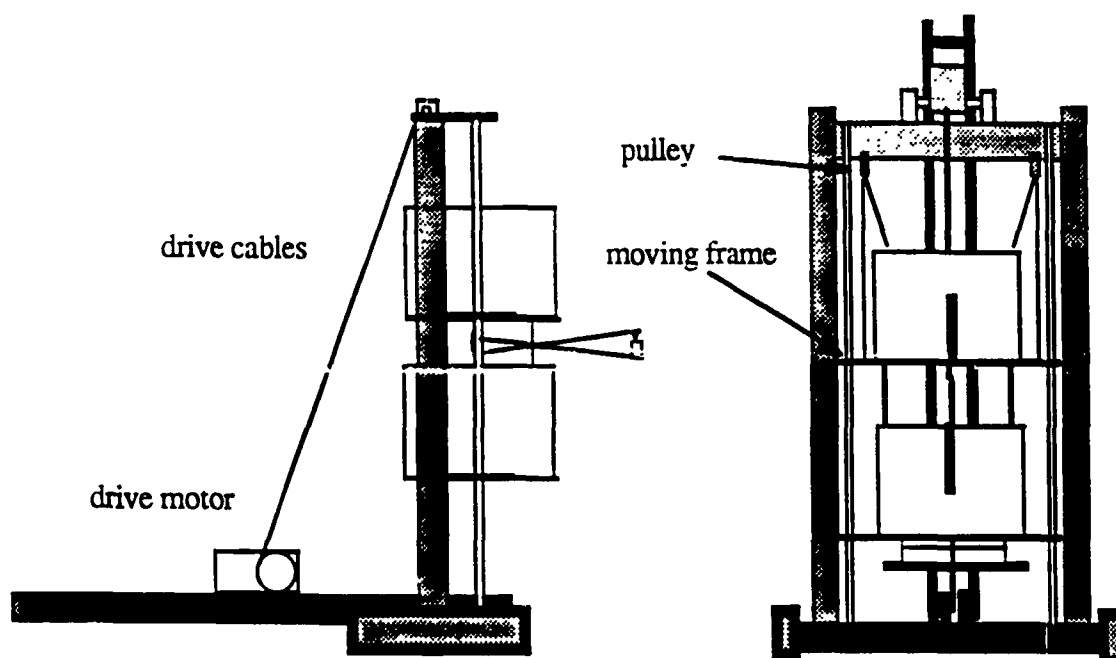


Figure 4.7 Furnace Transport System.

Figure 4.7 shows the furnace transport system. The furnaces are fixed to a moving frame which slides on steel rods fixed to the columns of the reaction frame. The drive to the moving frame is provided by a 1/4 horsepower DC electric motor driving two take-up reels. The take-up reels wind 3.2 mm diameter swaged steel cables which are routed through pulleys attached to the top reaction frame beam. Five seconds are required to transport a furnace from the hold station to the specimen station. The specimen station hold time can be varied independently for each furnace from a minimum of 30 seconds to a maximum of eight minutes in 30 second increments. The design and manufacture of the furnace transport sequencing

electronics was performed by Donald Keim of the Mechanical Engineering Department of the University of Washington.

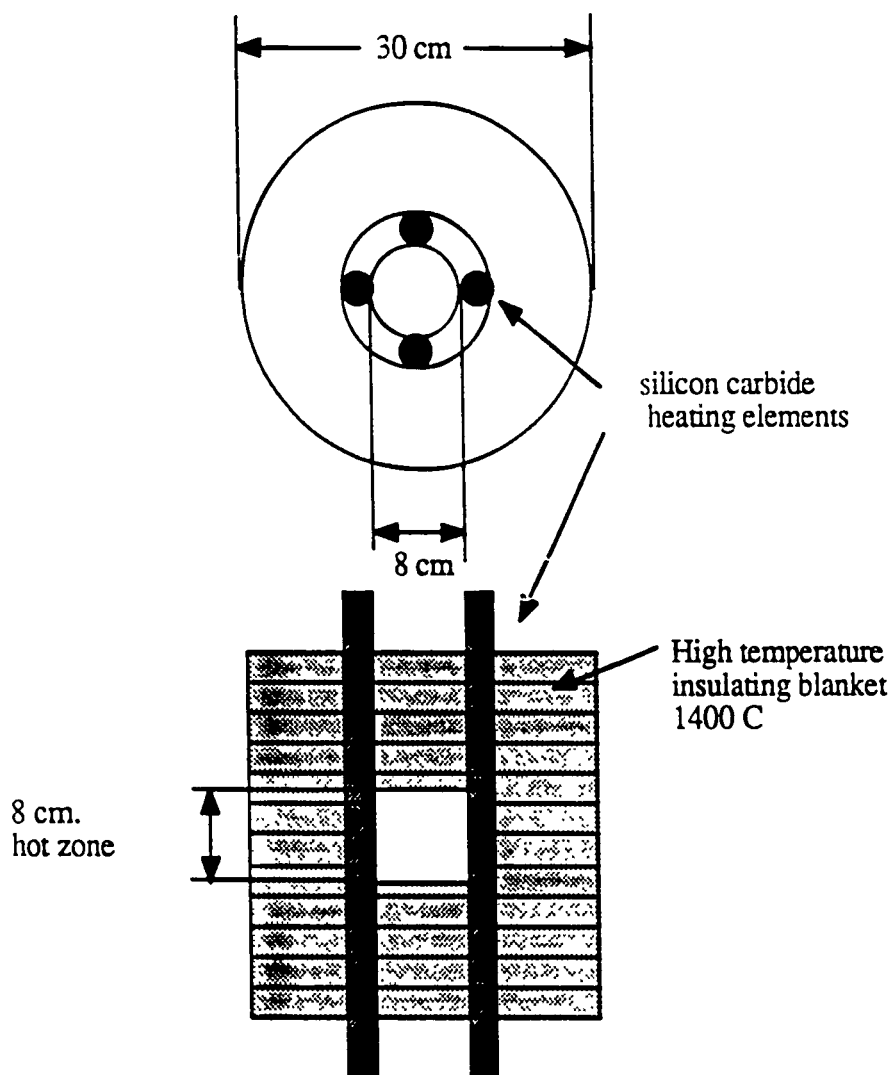


Figure 4.8 Silicon Carbide Resistance Element Furnace.

The machine is equipped with two 30 cm high by 30 cm diameter high temperature furnaces as shown in Figure 4.8. Each furnace is powered by four 35.6 cm long silicon carbide glo-bar heating elements. The elements have a hot section length of 10.2 cm and a outside diameter of 2.54 cm. The furnaces have internal insulation composed of many layers of high temperature blanket. The furnaces are maintained

at a set temperature with a pair of Barber Coleman 560 silicon controlled rectifier (SCR) controllers.

Figure 4.9 shows two time-temperature plots measured with a thermocouple attached to a W-FeCrAlY specimen surface. The one data set was taken with forced air cooling the specimen, the other data set did not.

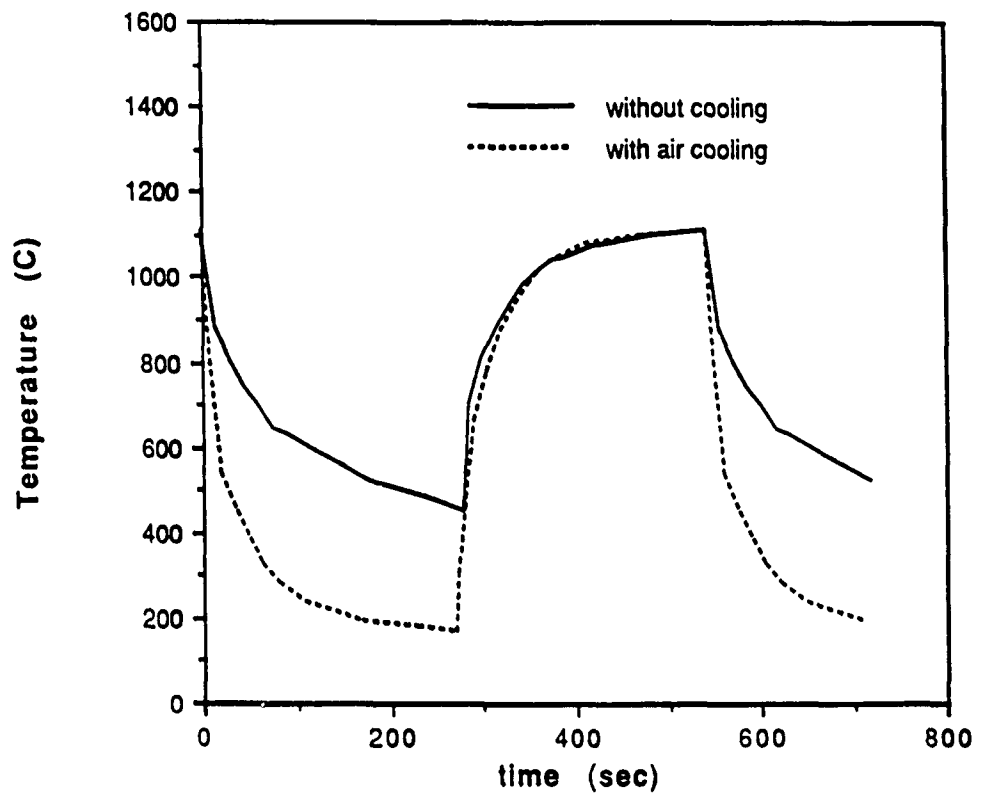


Figure 4.9 Creep Thermal Cycler Time-Temperature History.

The results show that the air cooled 1110 C to 165 C thermal cycle had an initial heating and cooling rate of approximately 22 C per second. The data taken without air cooling showed a similar initial heating rate but a reduced initial cooling rate. In both cases the initial heating and cooling rate moderated as the temperature of the specimen changed.

4.3 Thermal Cycling Dimensional Change Results

Table 4.1 Longitudinal Thermal Cycling Strain

<u>Test Specimen</u>	<u>100 Cycles</u>	<u>500 Cycles</u>	<u>750 Cycles</u>
CF-1100-352	.005	.024	*
CF-1100-534	.002	.008	*
CF-1100-800	not tested	damaged	*
ASF-20-1100-352	.004	.015	*
ASF-20-1100-352 retest		.016	
ASF-20-1100-534	.011	.025	*
ASF-20-1100-800		.007	*
ASF-5-1100-352	-.001	.000	.007
ASF-5-1100-534	.001	.003	.015
ASF-5-1100-800	not tested	.004	not tested
AF-1100-352	-.002	-.001	.007
AF-1100-534	-.001	.002	.012
AF-1100-800	not tested	.001	not tested

* indicates excessive damage

The data above was obtained by measuring the total test specimen length before and after thermal cycling with a hand held micrometer. The longitudinal thermal cycling strain was then computed as the as-cycled total length minus the before-cycling length quantity divided by the before cycling gauge length. The resolution of this method is probably not better than 20 micron. With a specimen gauge length of 28 mm the smallest resolvable difference in the data is approximately 0.001. Any differences in

the data smaller than 0.001 are therefore obscured by experimental error. This is particularly important to realize when examining the results for the ASF-5, and AF specimens for the 100 and 500 thermal cycle cases.

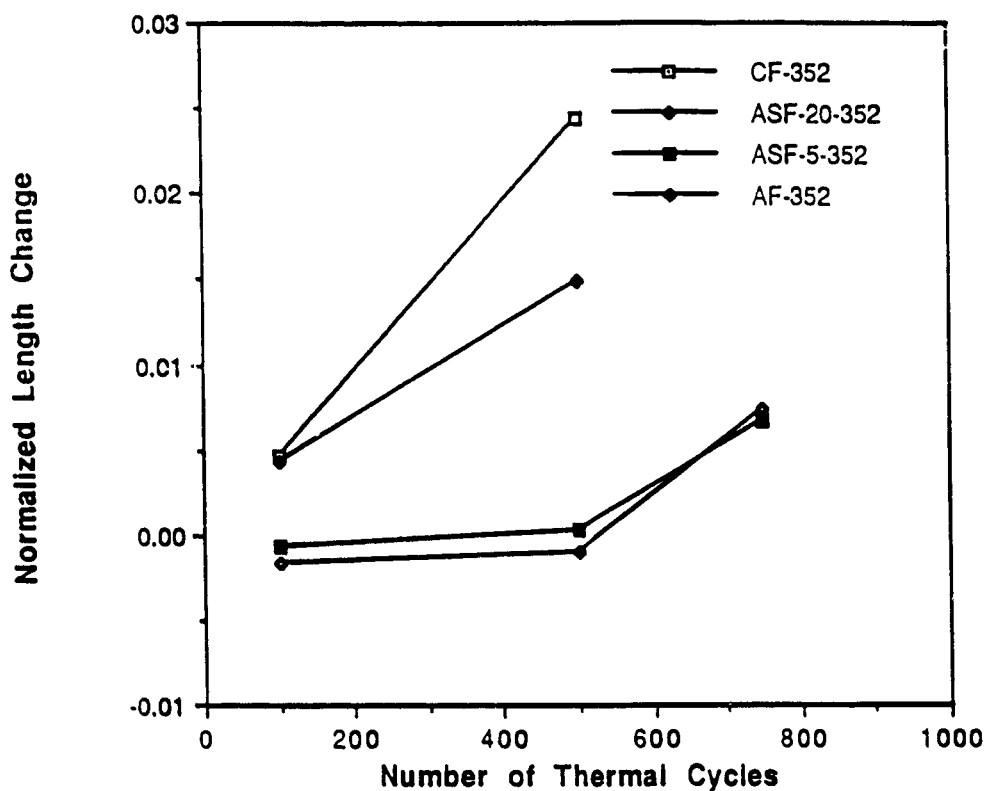


Figure 4.10 Normalized Length Change Versus Number of Thermal Cycles, 1100-352 C.

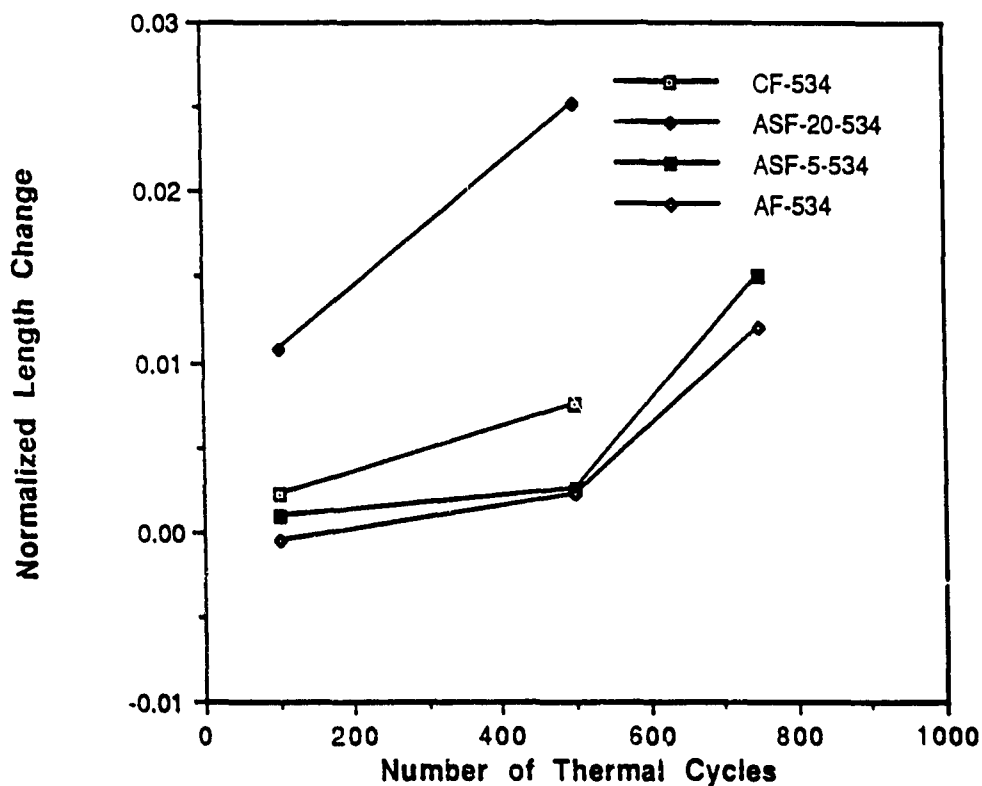


Figure 4.11 Normalized Length Change Versus Number of Thermal Cycles, 1100-534 C.

Figures 4.10 and 4.11 show that the CF and ASF-20 specimens developed much greater longitudinal deformation under thermal cycling than did the ASF-5 and AF specimens. These figures also show that the ASF-5 and AF specimens developed a higher rate of deformation as the number of cycles increased.

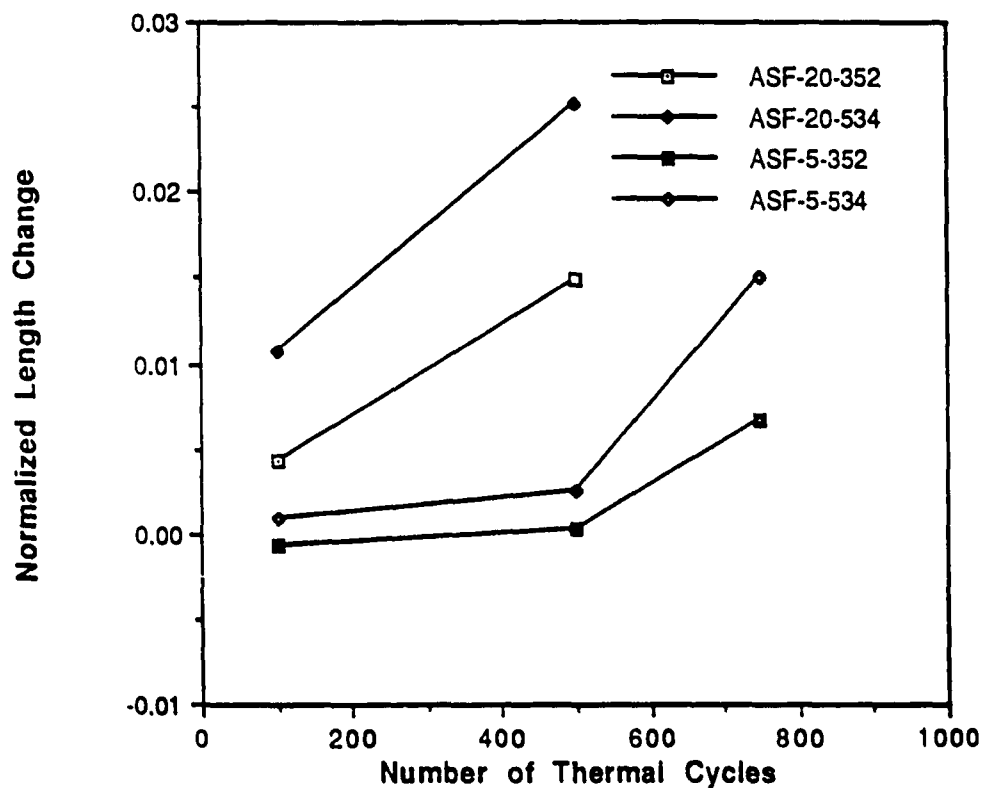


Figure 4.12 Normalized Length Change Versus Number of Thermal Cycles, ASF-20, ASF-5 Comparison.

Figure 4.12 shows that the ASF-5 specimens developed less deformation due to thermal cycling than the ASF-20 specimens. This result is significant since the two different materials were produced in the same way and contained nearly identical volume fractions of reinforcement. The only variance in the materials was that the aspect ratio of the tungsten reinforcement of the ASF-20 specimens was twenty while the aspect ratio of the tungsten reinforcement of the ASF-5 was five.

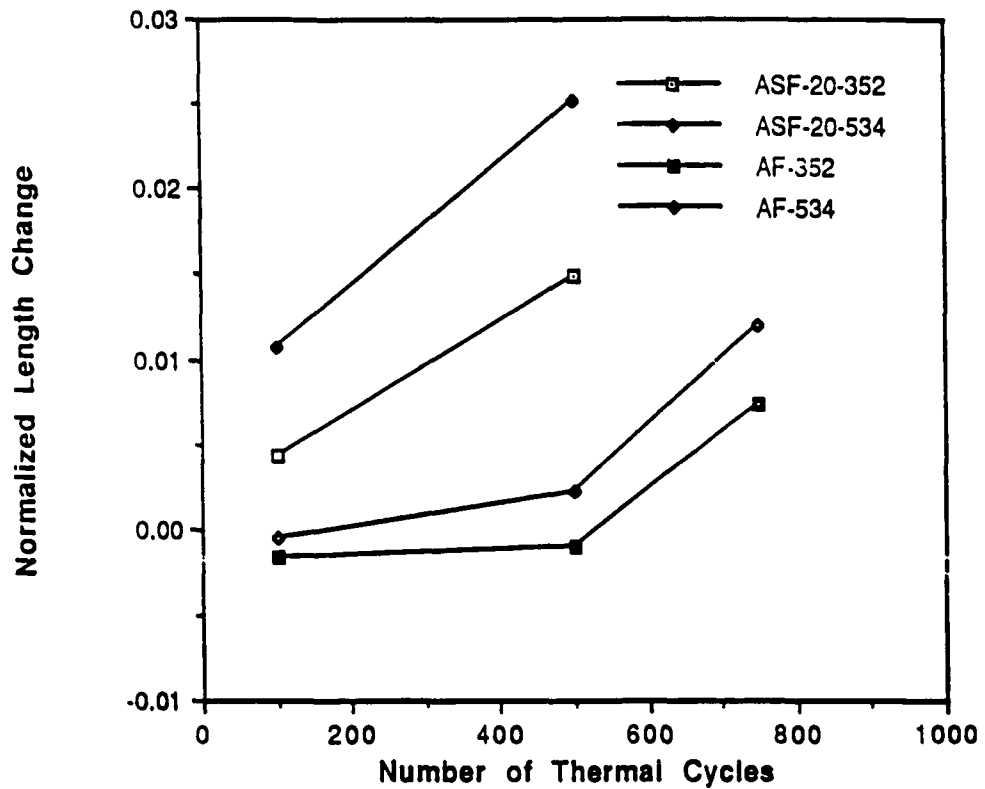


Figure 4.13 Normalized Length Change Versus Number of Thermal Cycles, ASF-20, AF Comparison.

Figure 4.13 compares the thermal cycling longitudinal deformation of the ASF-20 and AF specimens. The only difference between the specimens was the addition of 10 volume percent Al_2O_3 ground fibers to the AF matrix. This figure shows much lower deformation in the AF specimens.

Table 4.2 Normalized Thermal Cycling Area Deformation

<u>Test Specimen</u>	<u>100 Cycles</u>	<u>500 Cycles</u>	<u>750 Cycles</u>
CF-1100-352	.018	*	*
CF-1100-534	.009	.046	
CF-1100-800			*
ASF-20-1100-352	.022		*
ASF-20-1100-352 retest			.135
ASF-20-1100-534	.049	.110	
ASF-20-1100-800			.056
ASF-5-1100-352	.003	.026	.055
ASF-5-1100-534	.007	.030	*
ASF-5-1100-800			.059
AF-1100-352	.003	.008	.406
AF-1100-534	.004	.022	.125
AF-1100-800			.033

* indicates excessive damage

The normalized area change was computed as the as-cycled test section area minus the before-cycling test section area quantity divided by the before-cycling before-cycling test section area. The test section area was computed by finding the maximum and minimum diameters at the longitudinal center of the specimen, and then using these values to calculate the area of an ellipse. The measurement resolution for this data is difficult to determine since the primary source of measurement error is the expansion of the thermal spray layer due to oxidation. The data is perhaps best considered a qualitative performance index of the different

composite types since the thermal spray layer degradation should be similar between specimens subjected to the same number of thermal cycles.

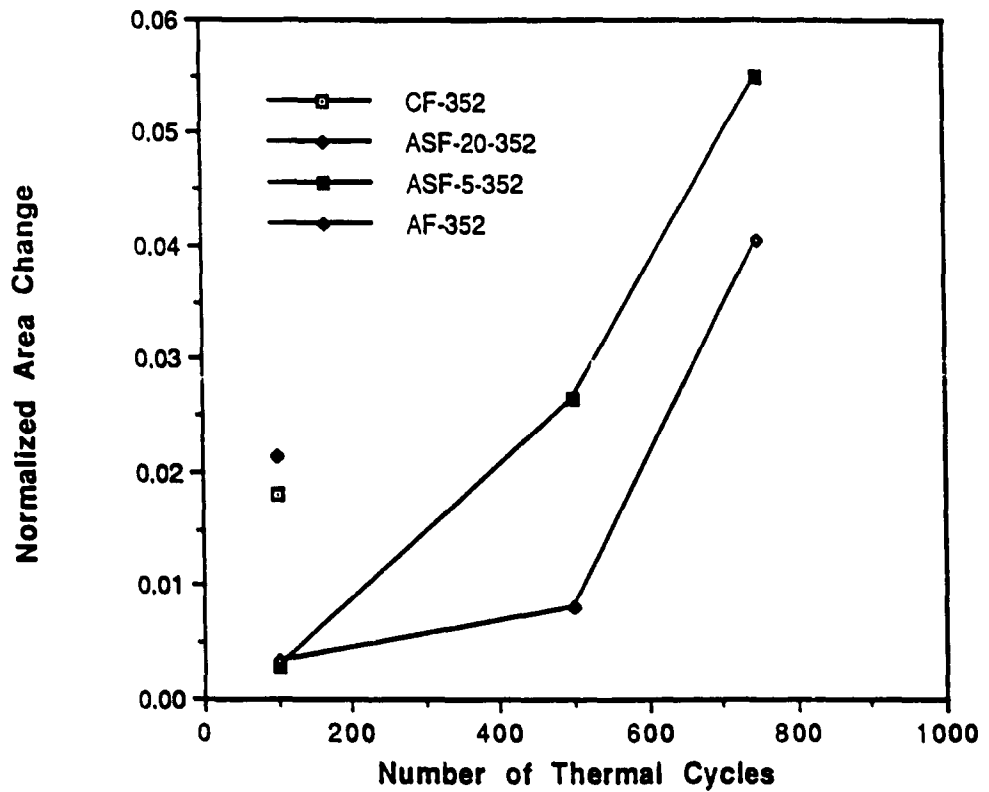


Figure 4.14 Normalized Area Change Versus Number of Cycles, 1100-352 C.

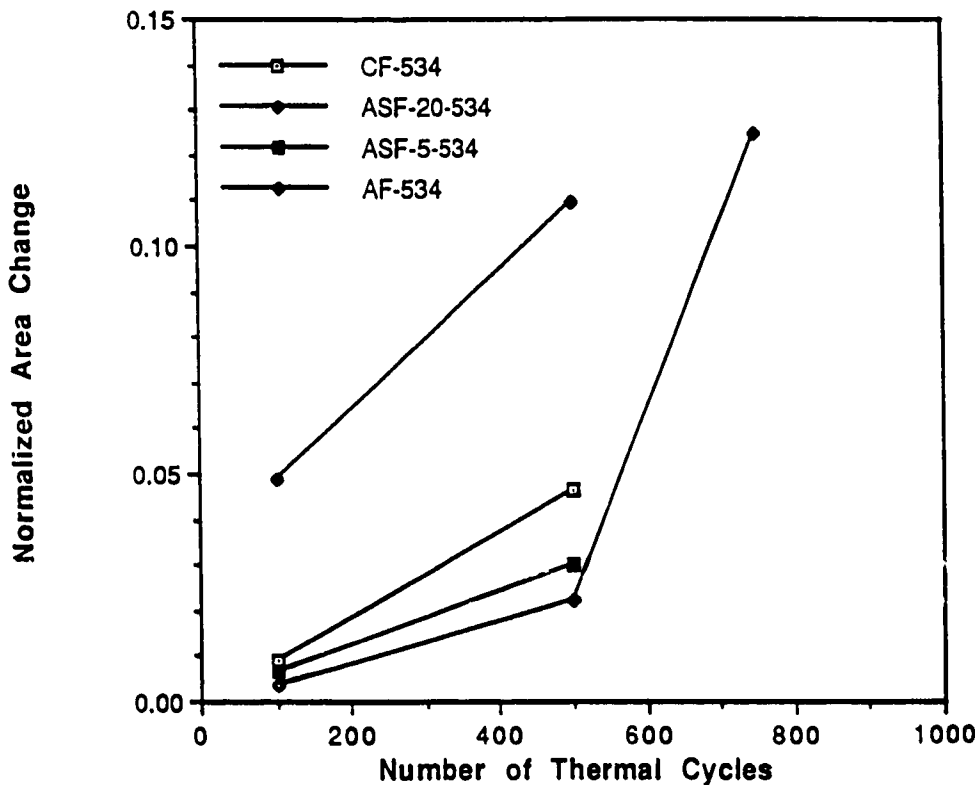


Figure 4.15 Normalized Area Change Versus Number of Cycles, 1100-534 C.

The preceding two figures demonstrate that the trends in the reduced area change data are quite similar to the trends in the reduced length change data. The reduced area data however is less complete since it was possible to measure the as-cycled length of some specimens while it was not possible to measure transverse area due to the degradation of the specimen coating.

Chapter 5 Material Analysis

5.1 Damage Processes

5.1.1 Growth of Reaction Phases

The following set of scanning electron microscopy (SEM) photographs were taken at Tohoku University, Sendi, Japan (Echigoya et al, 1990). The photographs document microstructural changes in the four test materials as the number of thermal cycles increase. All of the specimens in this set of photographs were thermal cycled between 1100 C and 352 C in the metallurgical thermal cycler.

Figure 5.1 details the microstructural features present in the SEM photographs. Perhaps the most apparent microstructural development is the growth of an attached reaction zone on the W-1%ThO₂ reinforcing fibers. This feature is particularly well displayed in the three ASF-5 photographs. During its growth the attached reaction zone develops numerous radial cracks. These cracks do not appear to propagate beyond the attached reaction zone - unmodified fiber interface. The extremely tight closure of the cracks indicate that the attached reaction zone is quite brittle. The hardness of the attached reaction zone will be discussed later in this chapter.

The as-received photographs of each composite type exhibit a very fine uniformly dispersed precipitate. This precipitate is most likely YFe₉ which has been well documented in the metallurgical literature (Wukusick and Collins, 1964). However after the specimens have been subjected to a number of thermal cycles the fine precipitate becomes depleted near the reinforcement. The radius of fine precipitate depletion becomes larger with increasing number of thermal cycles. This effect is particularly visible in the AF, 500 cycles 1100-352 C case, in which the depletion zone is approximately 80 microns wide.

The 500 cycle specimens display an irregularly shaped phase uniformly dispersed within the YFe₉ depletion zone. This phase can be expected to have significant mechanical effects since it inhabits the reinforcement-matrix interfacial zone. An atomic weight percent analysis of this phase will be presented in the next section.

Perhaps the microstructural feature which has the greatest mechanical significance is the circumferential debonded zone at the attached reaction zone-matrix interface. This feature is well developed in the CF and ASF-20 specimens after 500 thermal cycles. The AF and ASF-5 specimens on the other hand appear to take 1000 cycles for an equivalent degree of damage.

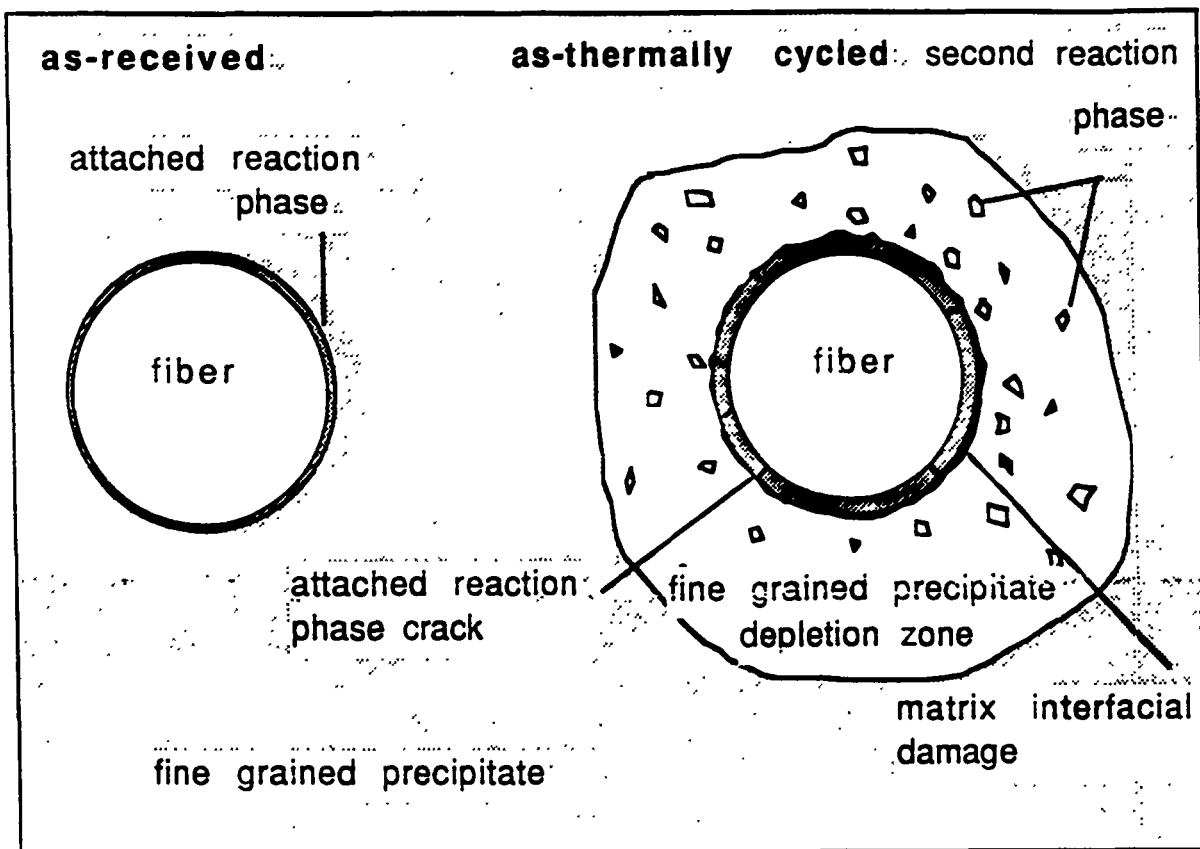


Figure 5.1 Microstructural Features Observed During Microscopy.

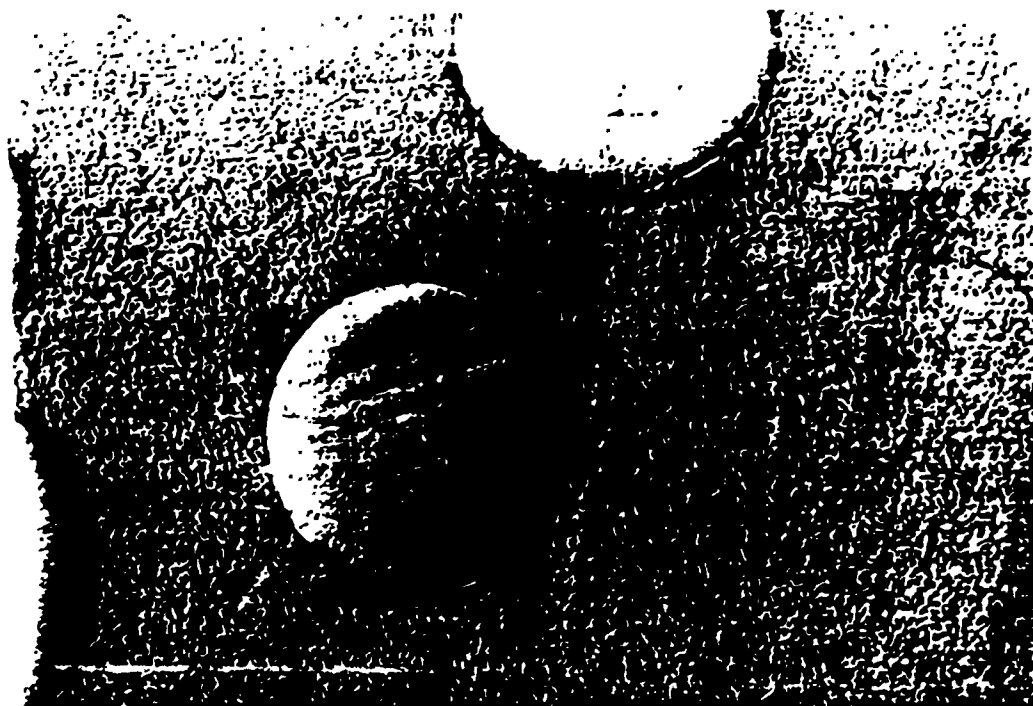


Figure 5.2(a) CF, as-received, Normal View.

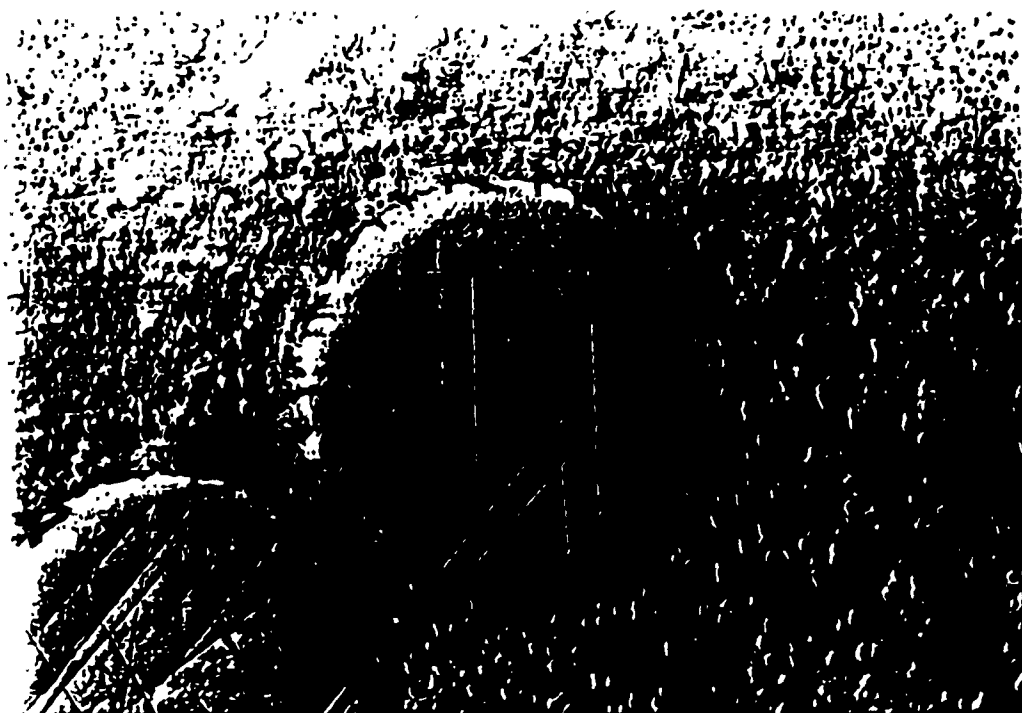


Figure 5.2(b) CF, 500 cycles 1100-352 C. Normal View.

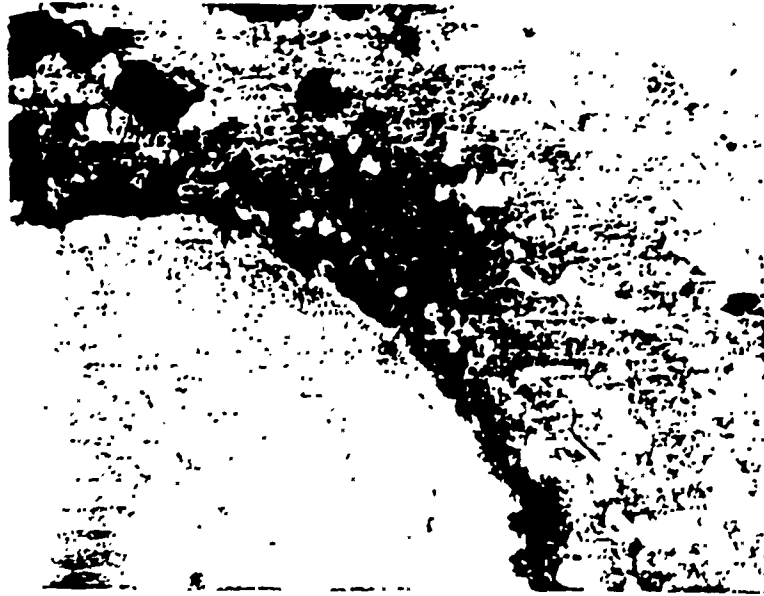


Figure 5.3 ASF-20, 500 cycles 1100-352 C. Normal View.



Figure 5.4(a) ASF-5, as received, Normal View.



Figure 5.4(b) ASF-5, 500 cycles 1100-352 C, Normal View.

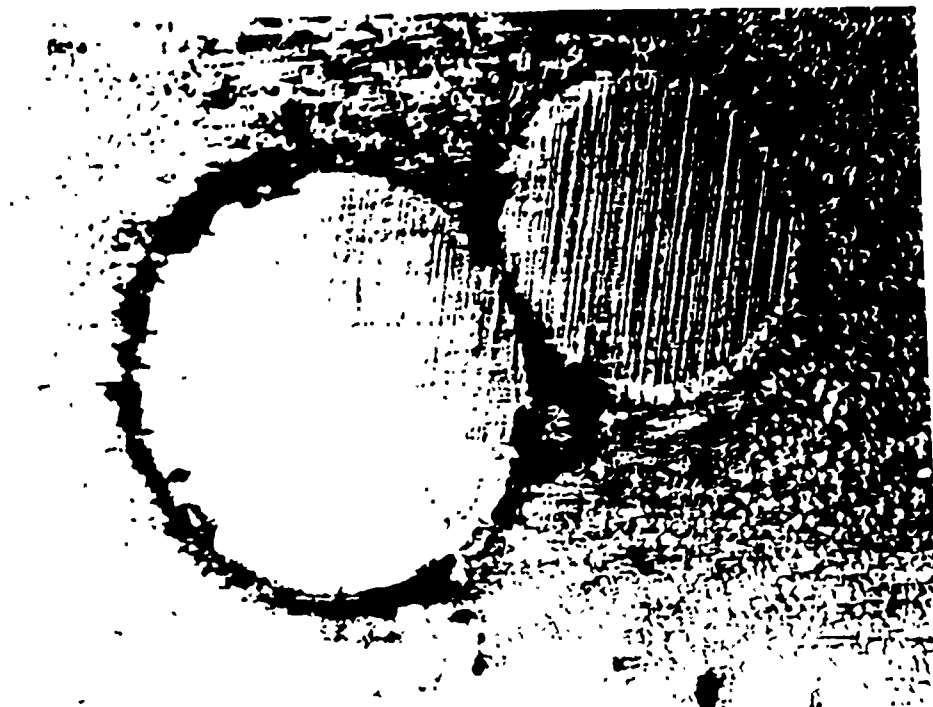


Figure 5.4(c) ASF-5, 1000 cycles 1100-352 C, Normal View.

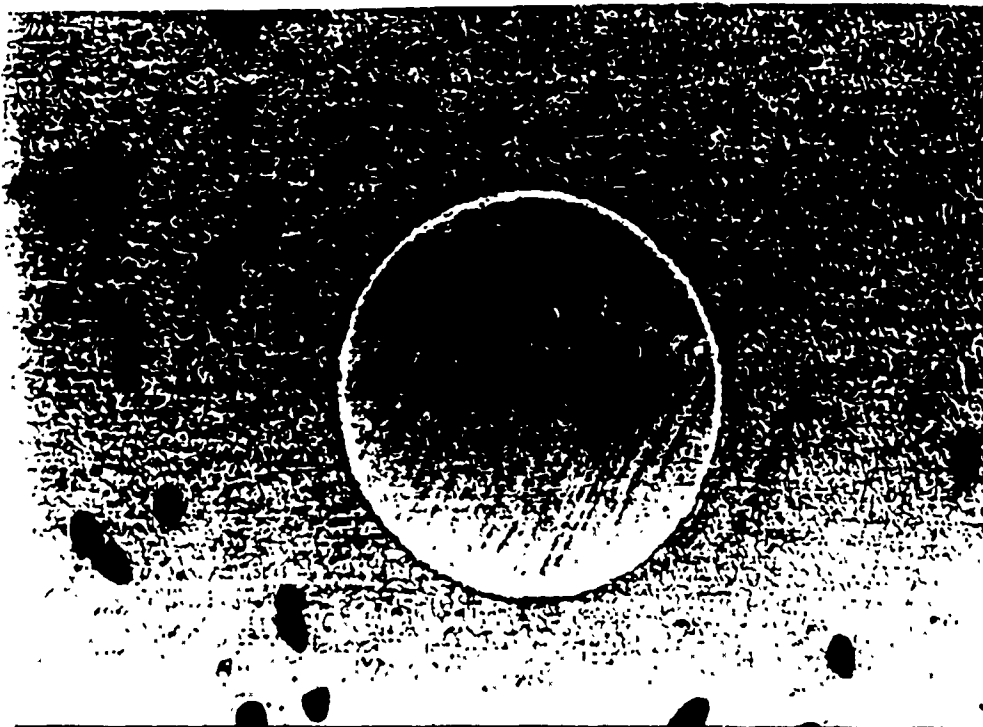


Figure 5.5(a) AF, as received, Normal View.

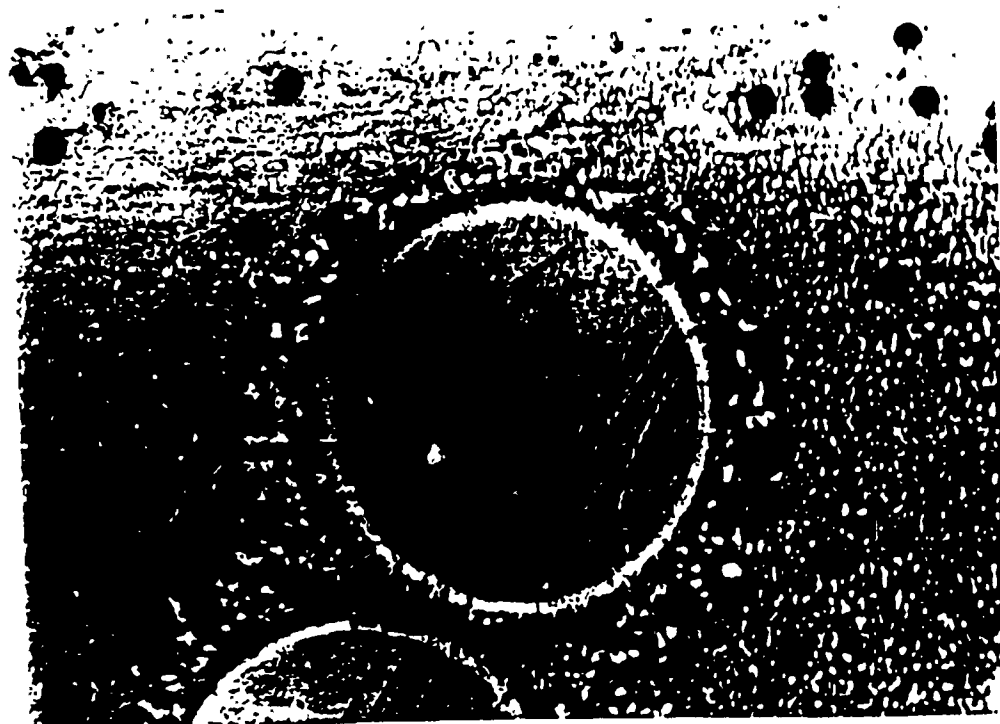


Figure 5.5(b) AF, 500 cycles 1100-352 C. Normal View.



Figure 5.5(c) AF, 1000 cycles 1100-352 C, Normal View.

Figure 5.6 displays the density of radial cracks in the attached reaction zone. These measurements were taken from SEM photographs of polished surfaces normal to the fiber longitudinal axis. This data follows the trend of the dimensional change data with the ASF-5 and AF specimens developing less attached reaction zone damage than the CF and ASF-20 specimens. The data also shows the rate of interface cracking per thermal cycle to be increasing with increasing number of thermal cycles in the ASF-5 and AF cases.

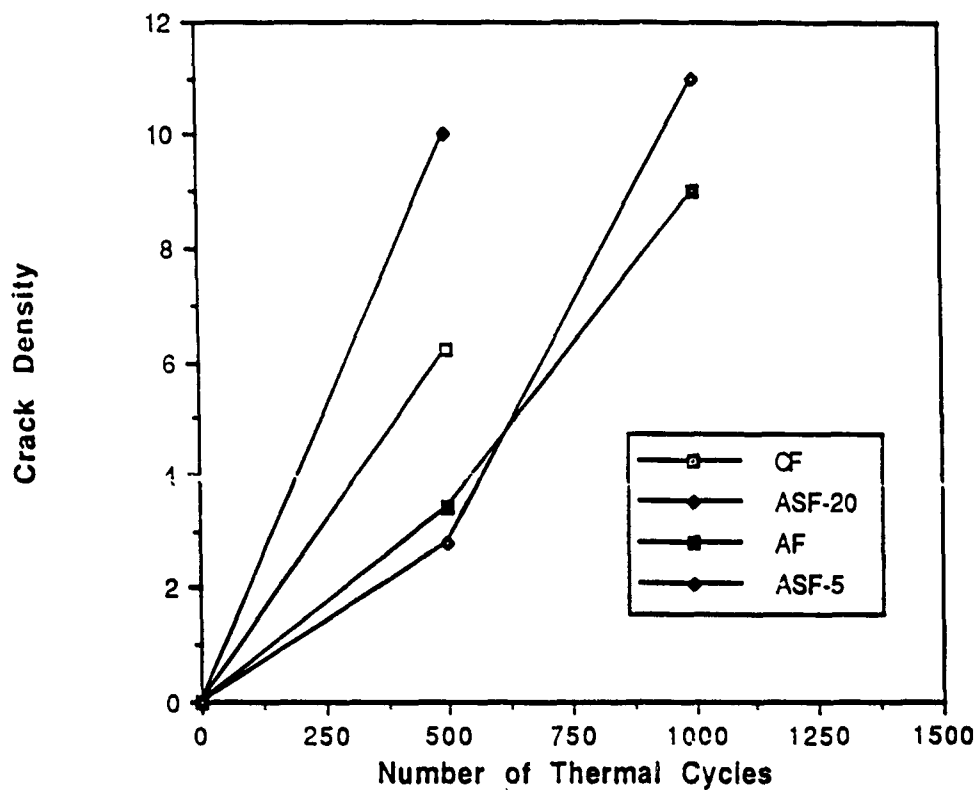


Figure 5.6 Reaction Zone Crack Density Versus Number of Thermal Cycles.

The growth of the attached reaction zone was measured as a function of number of thermal cycles. The results shown in Figure 5.7 indicate that the thickness of the attached reaction zone grew linearly with the number of cycles and the AF hybrid specimen exhibited the smallest growth rate. The CF, ASF-20, and ASF-5 materials exhibited numerically identical results.

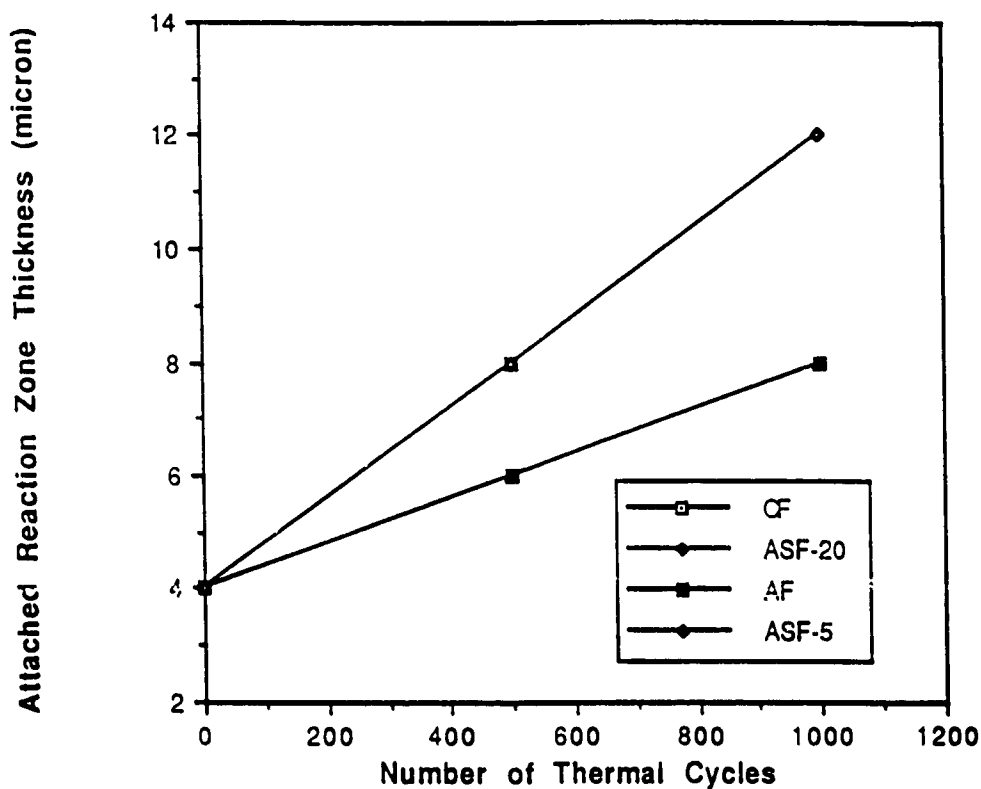


Figure 5.7 Attached Reaction Zone Thickness Versus Number of Thermal Cycles.

Figures 5.8 and 5.9 were developed at Tohoku University by energy dispersive X ray spectroscopy (EDS) (Echigoya et al, 1990). All of the figures indicate the retention of an essentially unmodified tungsten reinforcement phase. Attached to the unmodified fiber is a circumferential attached reaction zone with an approximate composition of 82W-11Fe-6Cr-2Al. A transmission electron diffraction pattern identified the crystal structure of this phase to be face centered cubic with a lattice parameter of 1.06 nm. The unmodified matrix has a nominal composition of 67Fe-25Cr-8Al-0.50Y.

In the 500 thermal cycle specimens an additional reaction phase is well developed with an approximate composition of 64-CR-24Fe-13W-2Al. This phase was shown in the preceding photographs as the coarse precipitate within the YFe₉ depletion zone, and will be referred to as the second reaction phase.

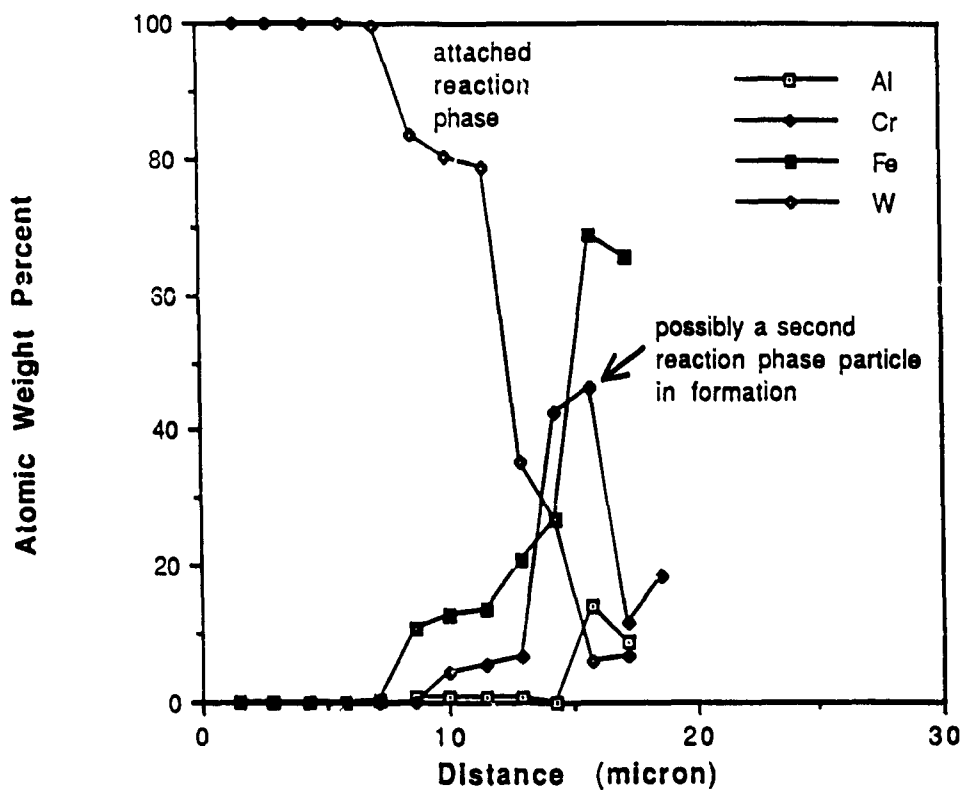


Figure 5.8(a) Atomic Weight Percent Versus Distance, CF, as received.

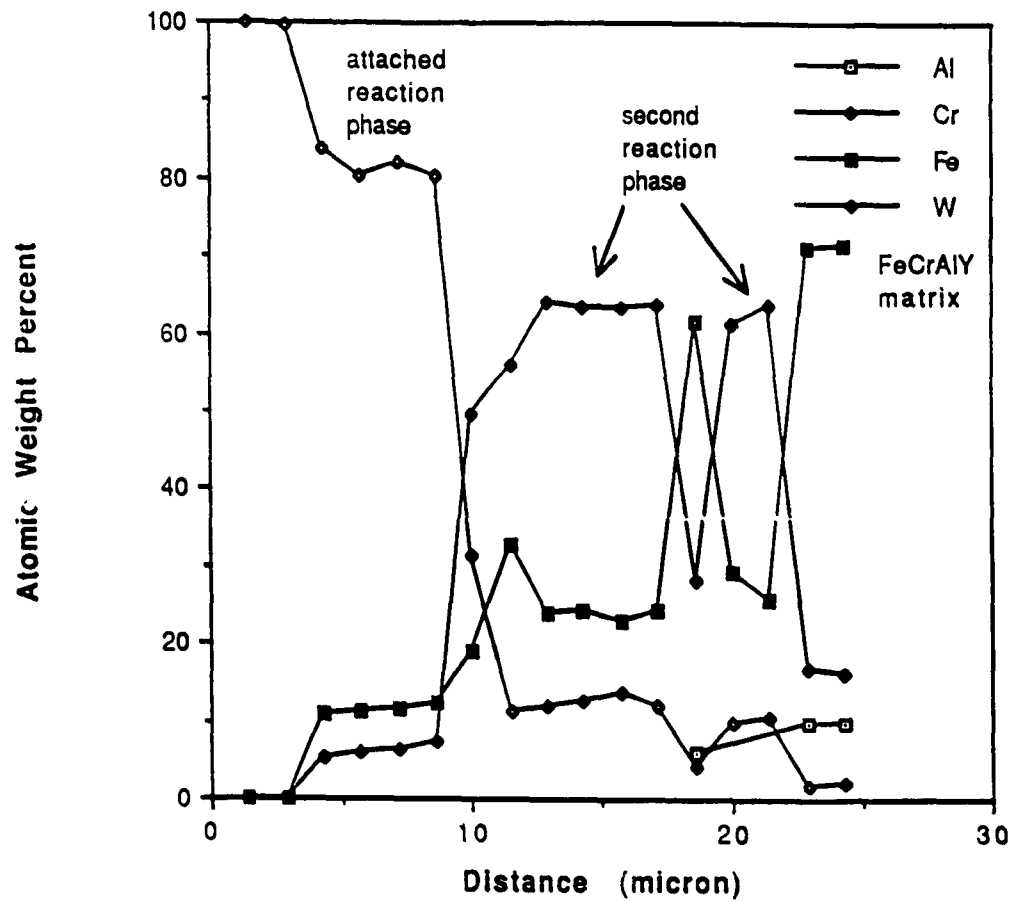


Figure 5.8(b) Atomic Weight Percent Versus Distance, CF, 500 cycles
1100-352 C.

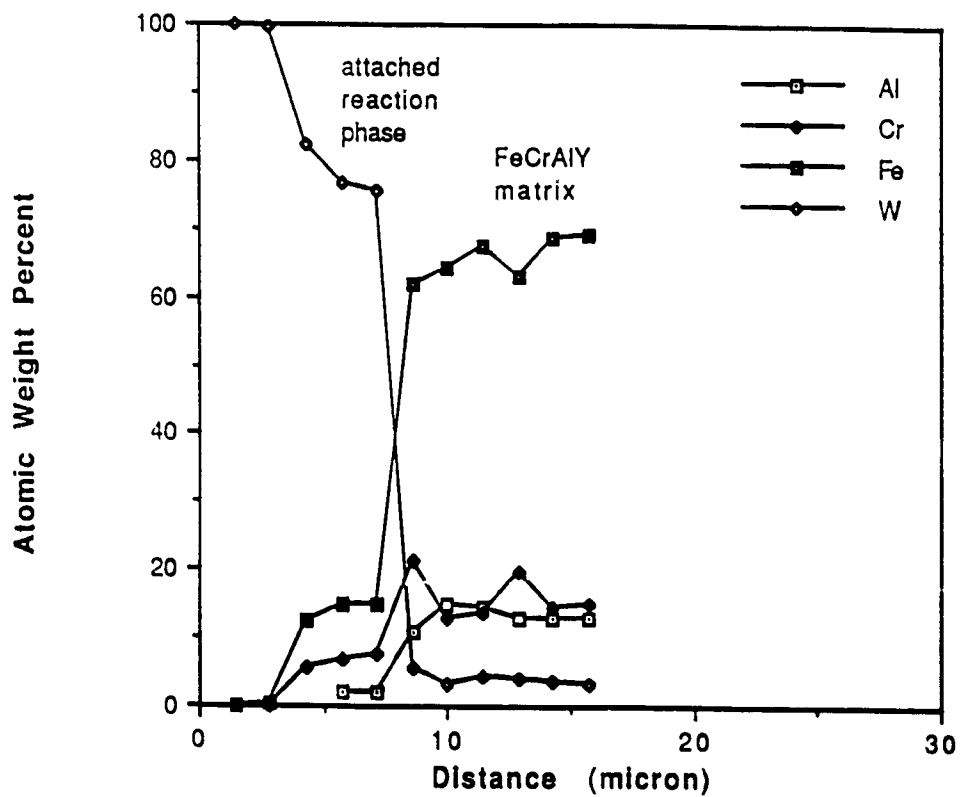


Figure 5.9(a) Atomic Weight Percent Versus Distance, AF, as received.

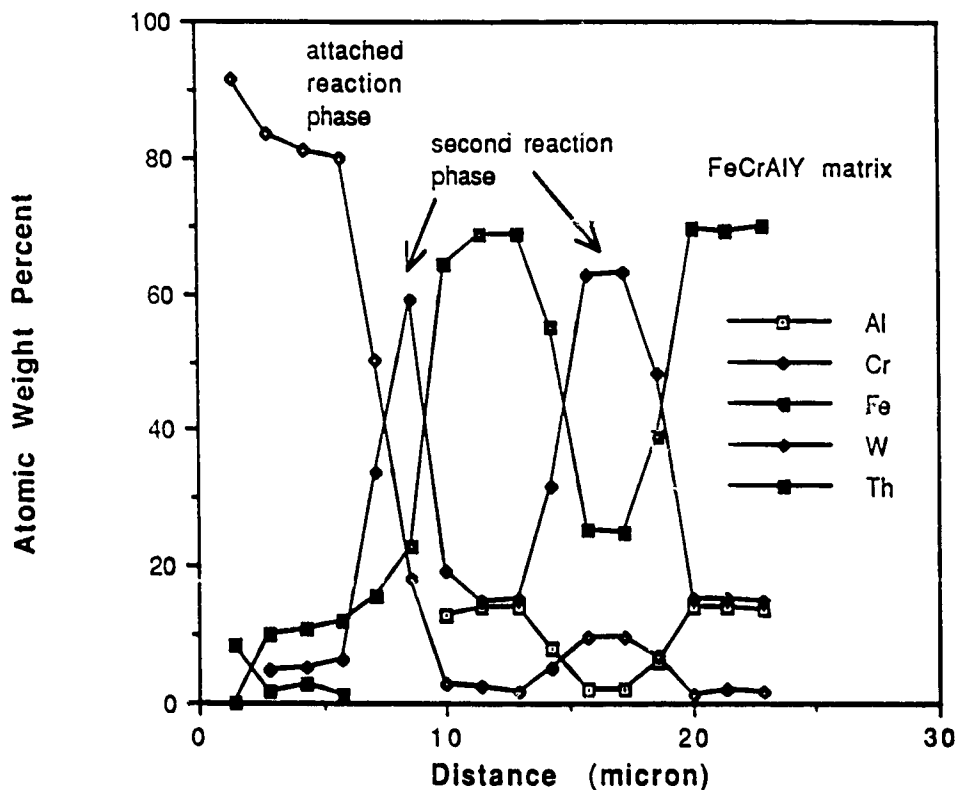


Figure 5.9(b) Atomic Weight Percent Versus Distance, AF, 500 cycles
1100-352 C.

Figure 5.10 contrasts the chromium weight percent for the CF, as-received and the CF, 500 thermal cycle cases. Figure 5.11 does the same for the AF material type. In these two figures it is quite apparent that the high chromium second reaction phase has greatly increased in extent with the increase in number of cycles.

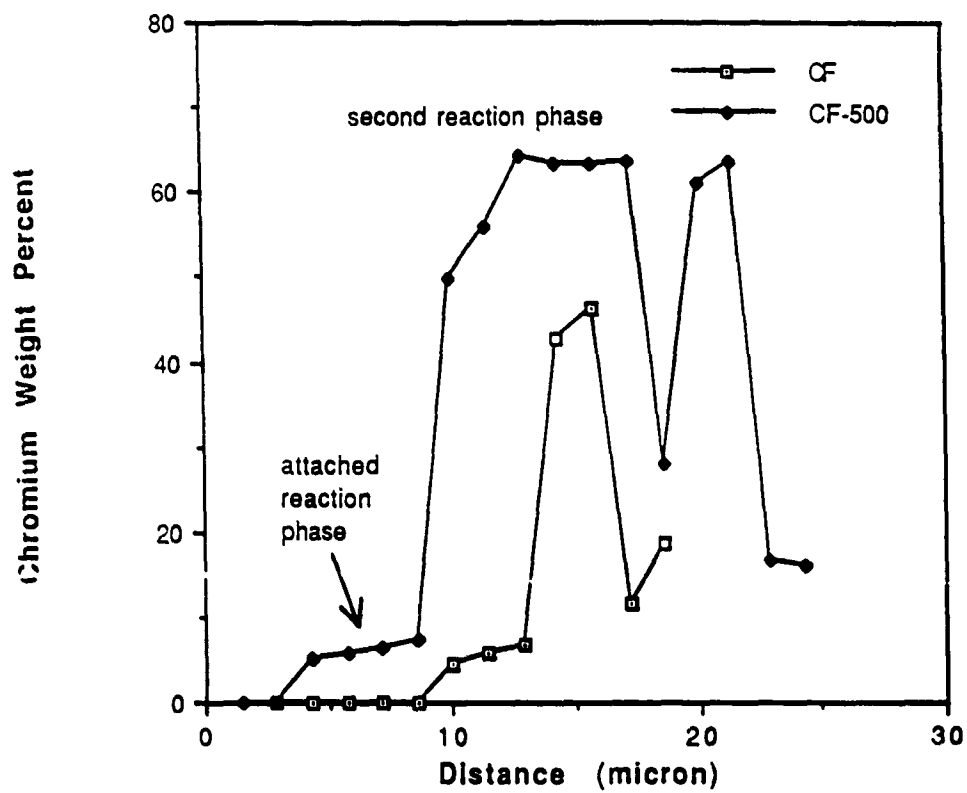


Figure 5.10 Chromium Weight Percent Versus Distance, CF.

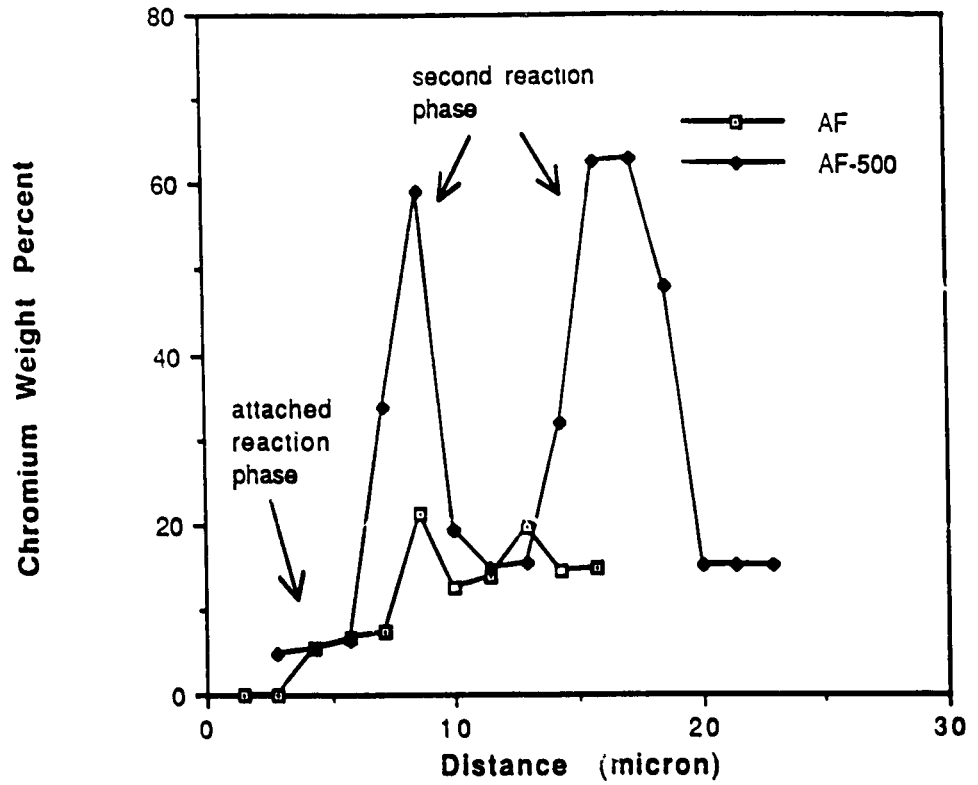


Figure 5.11 Chromium Weight Percent Versus Distance, AF.

Figure 5.12 shows the Vickers microhardness test indentions in the AS7-5 specimen cycled 500 times between 1100 C and 352 C. Figure 5.13 is a similar photograph of the AF 500 cycles 1100 C to 352 C specimen. The photographs indicate that the attached reaction zone is quite hard by the comparatively small size of the microhardness indentions, and by the reduction in severity of abrasive scratches.

Figure 5.14 shows the Vickers microhardness data where the fiber is on the left and the matrix is on the right. This data also indicates that the attached reaction zone is quite hard. The high hardness and thin crack morphology displayed in the SEM photographs indicates that the attached reaction zone is brittle at low temperatures.



Figure 5.12 Microhardness Indentations of ASF-5, 500 cycles 1100-352 C.



Figure 5.13 Microhardness Indentations of AF, 500 cycles 1100-352 C.

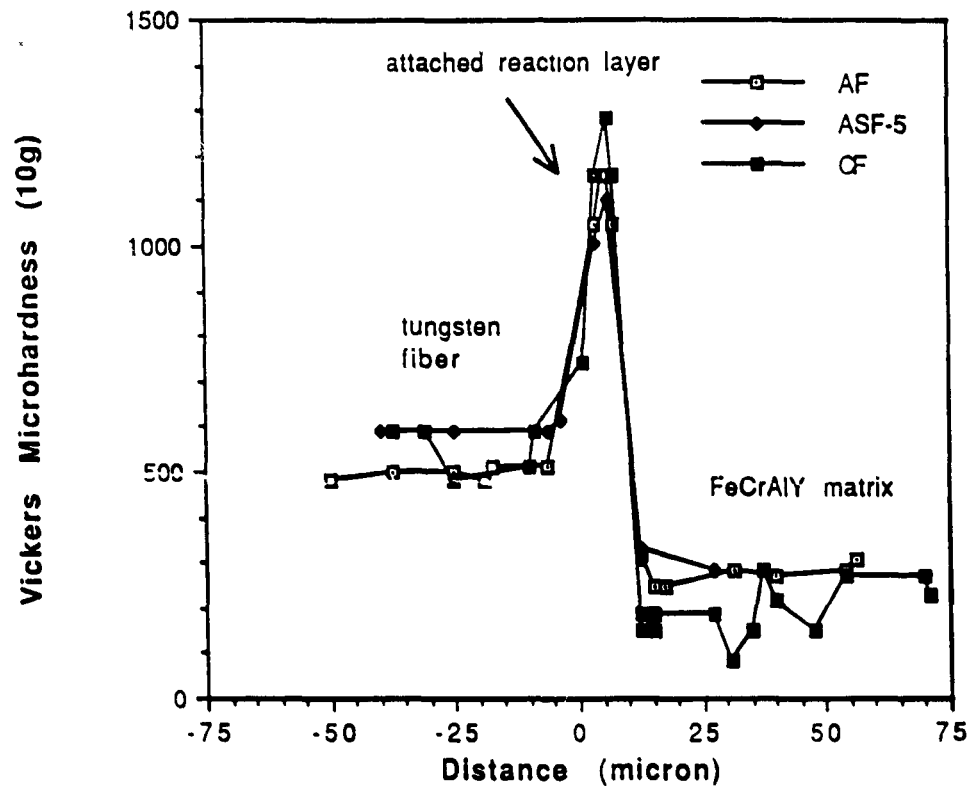


Figure 5.14 Vickers Microhardness Versus Distance.

5.1.2 Transmission Electron Microscopy Study

The following four transmission electron microscopy (TEM) photographs were also prepared at Tohoku University (Echigoya et al, 1990).

Figure 5.15 shows the attached reaction zone. This phase is seen to be free of dislocations or intergranular porosity. The lack of a significant amount of dislocations is a further indication that the attached reaction phase is brittle.

Figure 5.16 is a TEM photograph of attached reaction zone-matrix interfacial region in the ASF-20, 500 cycles, 1100 C to 352 C specimen. The dislocation configuration has a particularly high density and defined orientation along the attached reaction zone interface in the lower left hand corner of the photograph. Previous work has indicated that these dislocations have been punched out from the interface in order to relax the high stress at the interface due to the mismatch in coefficient of thermal expansion mismatch (Taya and Mori, 1987; Taya et al, 1990).

Figure 5.17(a) shows an interfacial location similar to that of Figure 5.16 in the AF, 500 cycle specimen. Echigoya et al. claim that the interfacial dislocation density is less in this case than in the ASF-20, 500 cycle case (Echigoya et al, 1990). Figure 5.17(b) shows the dislocation morphology near the alumina fiber-matrix interface in the same specimen. Again in this case the dislocation density is very high. The presence of this high dislocation density near the alumina fibers effects a reduction in thermal mismatch strain near the larger tungsten fibers (Echigoya et al, 1990) and at the same time increases the flow strength of the hybrid matrix as a whole. This results in a decrease in the severity of thermal cycling damage along the primary reinforcement in the AF case.



Figure 5.15 AF, 500 Cycles. Attached Reaction Layer.

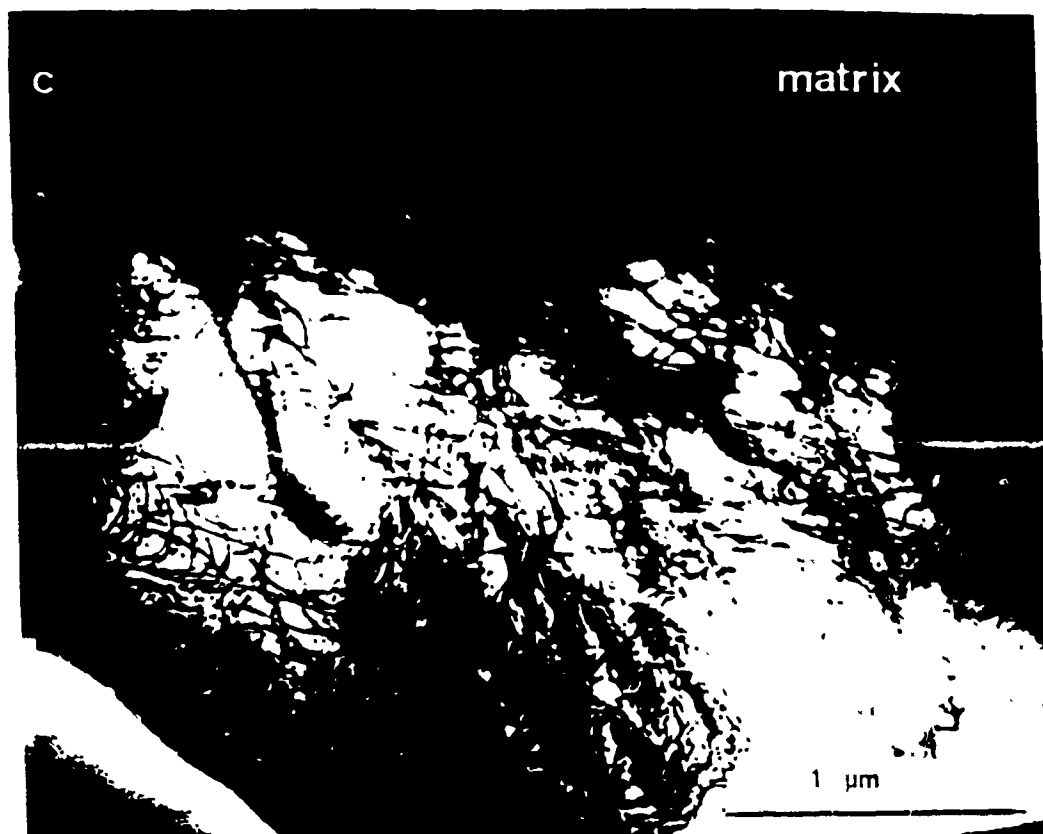


Figure 5.16 ASF-20, 500 Cycles. Matrix and Attached Reaction Zone.



Figure 5.17(a) AF. 500 Cycles. Matrix and Attached Reaction Zone.

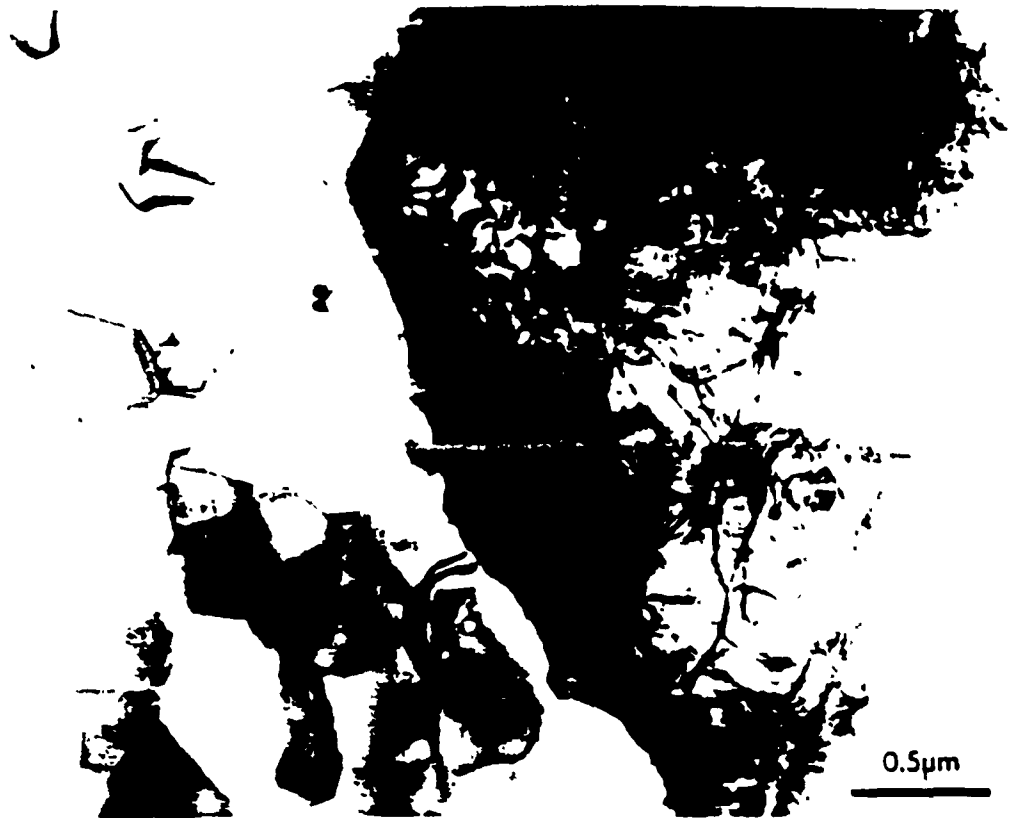


Figure 5.17(b) AF, 500 Cycles, Matrix and Alumina Fiber.

5.1.3 Thermal Spray Layer Damage

The thermal spray layer-matrix interface for the ASF-20, 100 cycles, 1100 C to 352 C specimen is shown in Figure 5.18(a). In this case the thermal spray bond quality is sufficiently good that it is difficult to identify the location of the interface. The 500 cycle specimens however, exhibit a degraded thermal spray layer-matrix interface. This degradation of the thermal spray layer bond is due to a combination of thermal-mechanical fatigue and oxidation processes. The weakened bond results in the thermal spray layer spalling and associated loss of specimen oxidation protection shown in Figure 5.18(c).

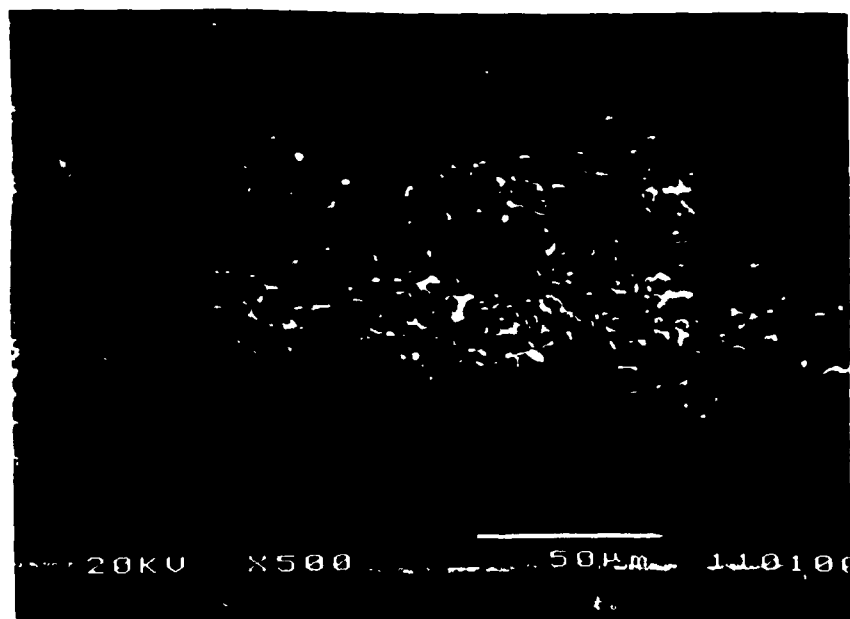


Figure 5.18(a) ASF-20, 100 cycles, Thermal Spray Layer.

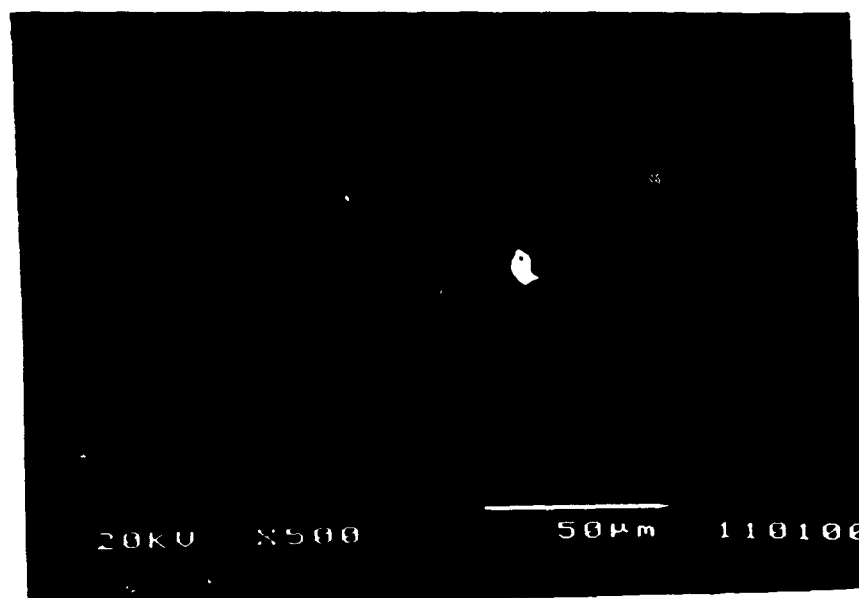


Figure 5.18(b) ASF-20, 500 cycles, Thermal Spray Layer.

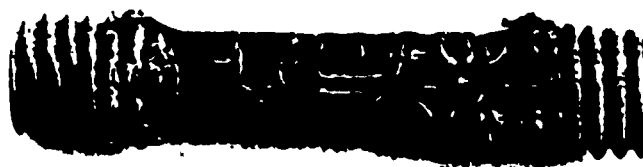


Figure 5.18(c) ASF-20, 500 cycles, Specimen Exterior.

5.2 Interfacial Microporosity Growth

Scanning electron microscopy (SEM) showed the as-received reinforcement-matrix interface was of high quality for each of the four material types. However, a small amount of porosity was present in the matrix adjacent to the fiber interface in the form of half micron diameter pores which outlined a 10 to 15 micron wide spherical substructure. This spherical substructure is the same size as the smaller metal powder particles used to form the matrix. Therefore, the as-received porosity is most likely due to insufficient time-temperature-pressure during the HIP treatment and the presence of a thin oxide layer on the surface of the powders due to the burn-off treatment.

Figure 5.19 shows the matrix-attached reaction phase interface near the fiber end and 800 micron from the fiber end for the ASF-5, 500 cycle specimen. In the ASF-5 material, 800 micron from fiber end is approximately the geometric center of the reinforcing fiber. These figures show that the ASF-5 case exhibits much less damage after 500 cycles than did the CF and ASF-20 cases. The damage near the fiber end is of the form of many complex, thin, branched cracks. The damage can be seen to occasionally terminate on pores, and some of the damage outlines second reaction phase particles. The same specimen exhibits very different morphology 800 micron from the fiber end. This region contains a significant amount of second reaction phase particles and the previously mentioned residual porosity from the HIP operation, but has little damage porosity.

Figure 5.20 shows the ASF-5, 750 cycle case exhibited much more significant damage. The damage has the form of many thin branched cracks connecting large highly irregular pores. Numerous irregular, rough surfaced cracks are continuous between the attached reaction zone and the damaged matrix. Again in this case, the degree of damage is less in the fiber center than near the fiber end.



Figure 5.19(a) ASF-5, 500 cycles, 1100-352 C, Lateral Section View, Fiber End.



Figure 5.19(b) ASF-5, 500 cycles, 1100-352 C, Lateral Section View, 800 Micron from Fiber End.

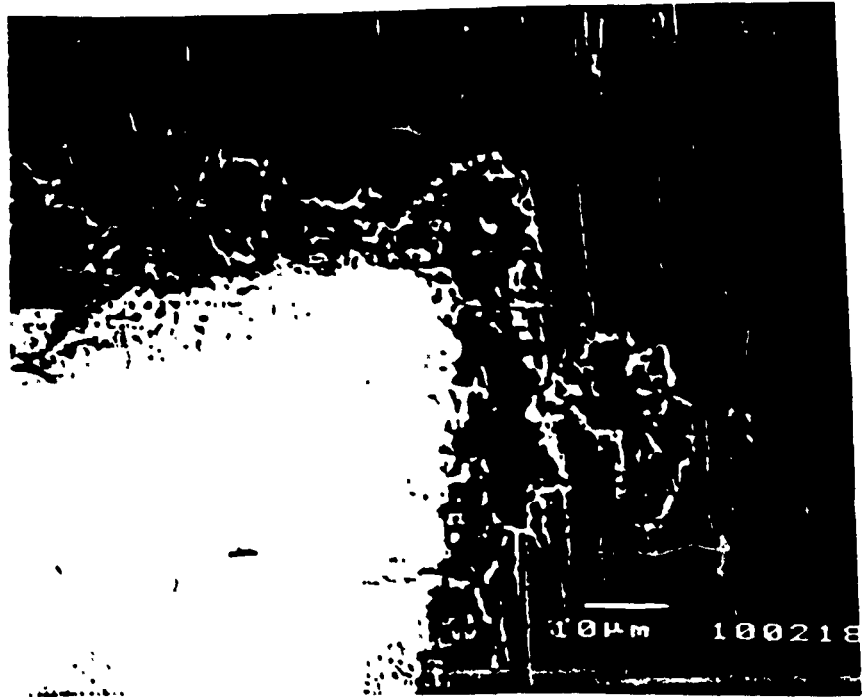


Figure 5.20(a) ASF-5, 750 cycles, 1100-352 C, Lateral Section View, Fiber End.

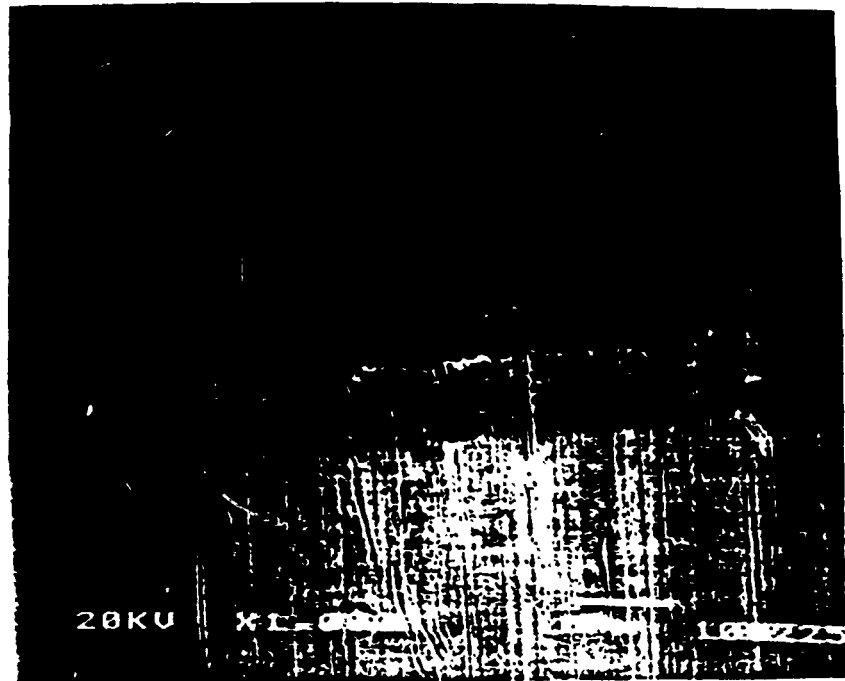


Figure 5.20(b) ASF-5, 750 cycles, 1100-352 C, Lateral Section View, 800 Micron from Fiber End.

The AF specimens exhibited a much lower rate of damage accumulation than did the ASF-20 specimens. This result is quite interesting since the AF material differs from the ASF-20 material only by the addition of misoriented, Al_2O_3 short fibers. In this case 800 micron from the fiber end is only about 30% of the distance to the fiber geometric center.

Figure 5.21 shows the AF, 500 cycle case had a small amount of damage near the fiber end. This damage was in the form of numerous thin connected cracks which often encircled second phase particles. This damage was similar to the fiber end damage exhibited by the ASF-5, 500 cycle specimens. The 800 micron from the fiber end location was undefected.

In Figure 5.22, the AF, 750 cycle case shows significant damage. This damage is in the form of a void layer approximately 10 to 20 micron wide. The AF material differs from the ASF-5 material in that the damage morphology is quite similar near the fiber end and 800 micron from fiber end locations.



Figure 5.21(a) AF, 500 cycles. 1100-352 C, Lateral Section View, Fiber End.



Figure 5.21(b) AF, 500 cycles, 1100-352 C, Lateral Section View, 800 Micron from Fiber End.



Figure 5.22(a) AF, 750 cycles, 1100-352 C. Lateral Section View, Fiber End.



Figure 5.22(b) AF, 750 cycles, 1100-352 C. Lateral Section View, 800 Micron from Fiber End.

In Figure 5.23, the ASF-20, 500 cycle specimen exhibits a far greater amount of damage porosity than the ASF-5, 500 cycle, and AF, 500 cycle specimens. The damage is in the form of numerous one to ten micron wide, irregular, connected pores. The damage morphology 800 micron from the fiber end is quite similar to the damage morphology at the fiber end.



Figure 5.23(a) ASF-20, 500 cycles, 1100-352 C, Lateral Section View, Fiber End.

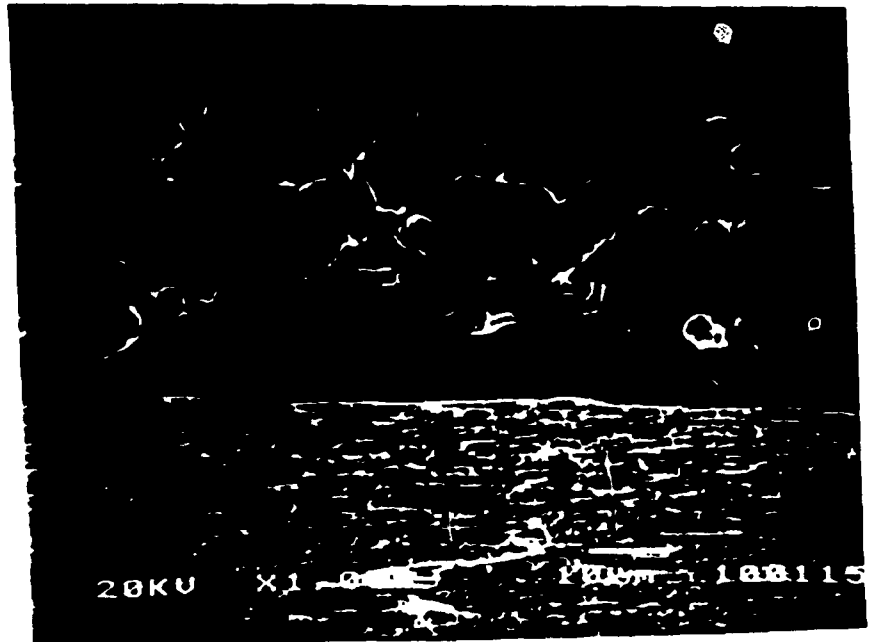


Figure 5.23(b) ASF-20, 500 cycles, 1100-352 C, Lateral Section View, 800 Micron from Fiber End.

The CF. 500 cycle specimen evidences massive matrix damage at the fiber ends. This damage is of the form of an approximately 40 micron wide elongated pore at the fiber end normal to the fiber longitudinal axis. This case also has a significant amount of damage at second reaction phase particle-matrix interfaces. In the same specimen the interfacial area 800 micron from the fiber end shows much less damage. Although along the fiber lateral interface an occasional large diameter pore is present.

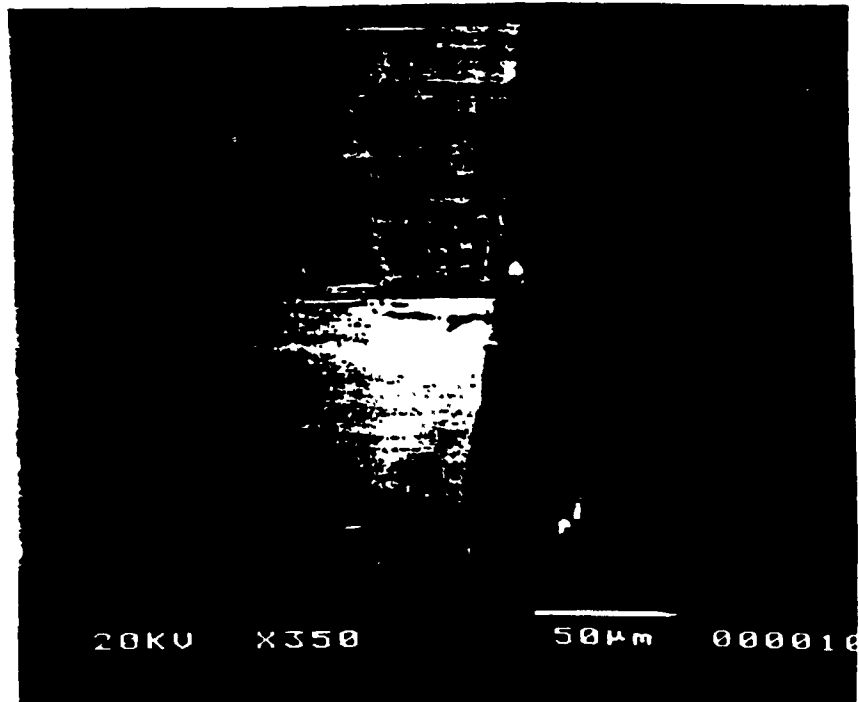


Figure 5.24(b) CF, 500 cycles. 1100-352 C. Lateral Section View, Fiber End.

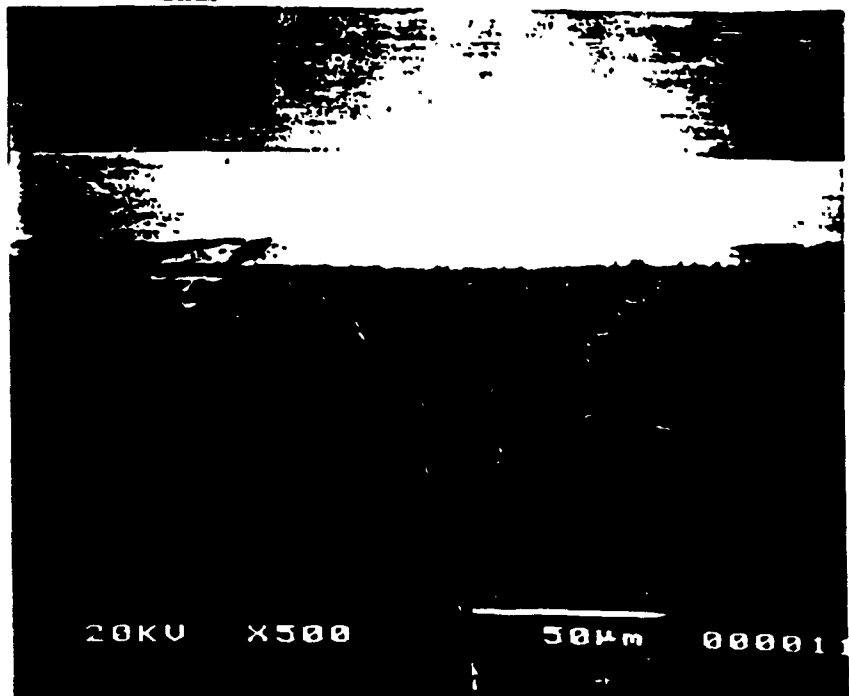


Figure 5.24(b) CF, 500 cycles. 1100-352 C. Lateral Section View, 800 Micron from Fiber End.

To quantitatively measure the damage state of the as-cycled materials approximately ten, 1000 magnification, overlapping SEM photographs were obtained starting at the end of the fiber. Light prints were made from the negatives of these photographs, and the damage present was colored black. This step was necessary to provide high contrast. The enhanced contrast photographs were then cut normal to the fiber interface into strips displaying 20 micron of fiber length. The strips were then individually scanned with a Apple Scanner connected to a Macintosh computer. The scanning software created a binary file which coded pixels as either black or white. Each black pixel represented an area of 0.0675 square micron of damage. A program was then developed with the help of another graduate student, Doug Graesser, which was able to count the number of black pixels present in the scan file. This procedure was followed for approximately 1000 microns of fiber length. The result of the computation then gave the amount of damage porosity present along a 20 micron long increment of fiber length for 50 total increments. Figure 5.25 shows how the area of SEM photographic coverage compared with the total length of fibers for the three material types scanned.

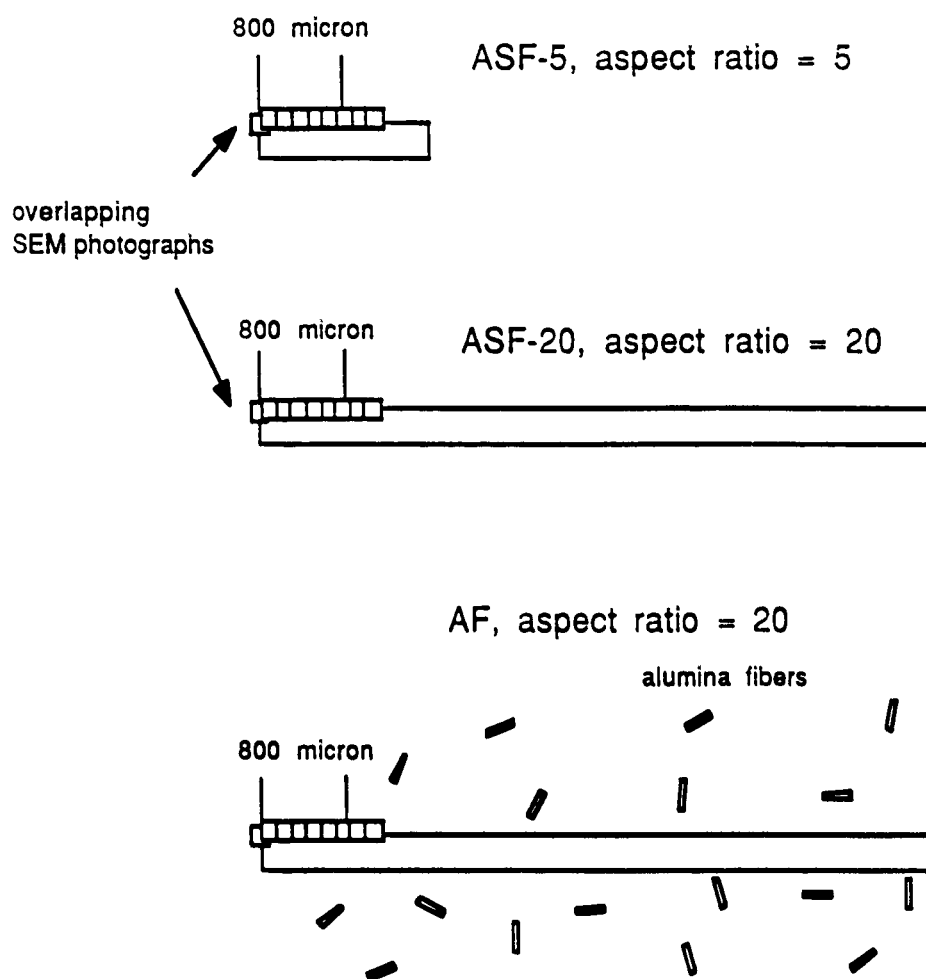


Figure 5.25 Damage Quantifying SEM Photograph Locations.

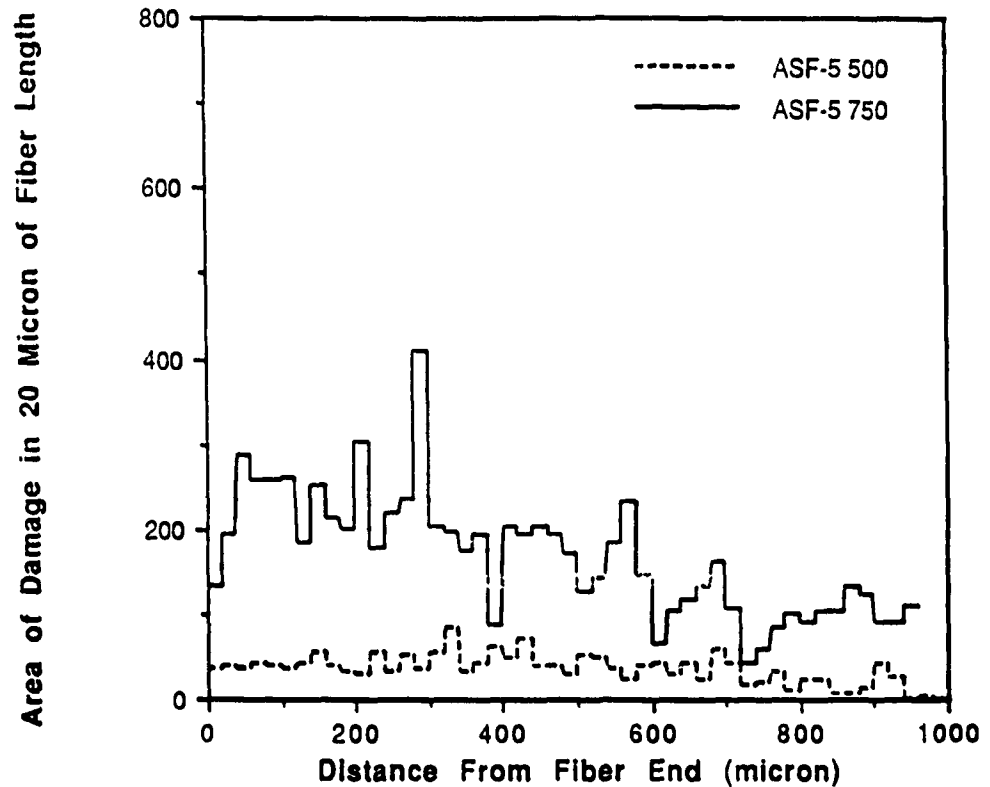


Figure 5.26 Interfacial Porosity as a Function of Distance from Fiber End, ASF-5, 500 and 700 cycles.

Figure 5.26 compares the results of this procedure for the ASF-5, 500 cycle, and the ASF-5, 750 cycle cases. In this material the region from 800 to 1000 microns from the fiber end corresponds to the geometric center of the fiber. This result shows both the 500 and 750 cycle cases had less damage porosity present near the fiber center than near the fiber end. The results also show that the 750 cycle case had much more damage present than did the 500 cycle case.

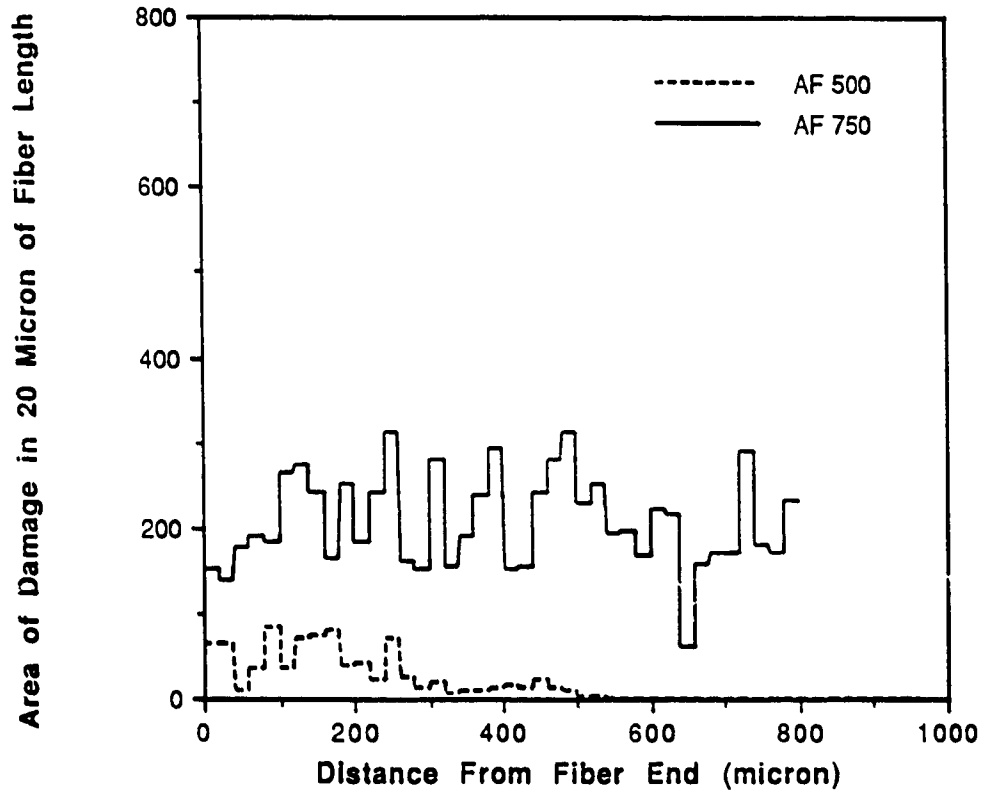


Figure 5.27 Interfacial Porosity as a Function of Distance from Fiber End, AF, 500 and 700 cycles.

Figure 5.27 shows that the AF, 500 cycle case has almost all of its damage porosity near the end of the fiber. After 750 cycles much more damage porosity is present and this porosity is distributed nearly equally along the 1000 micron measurement section.

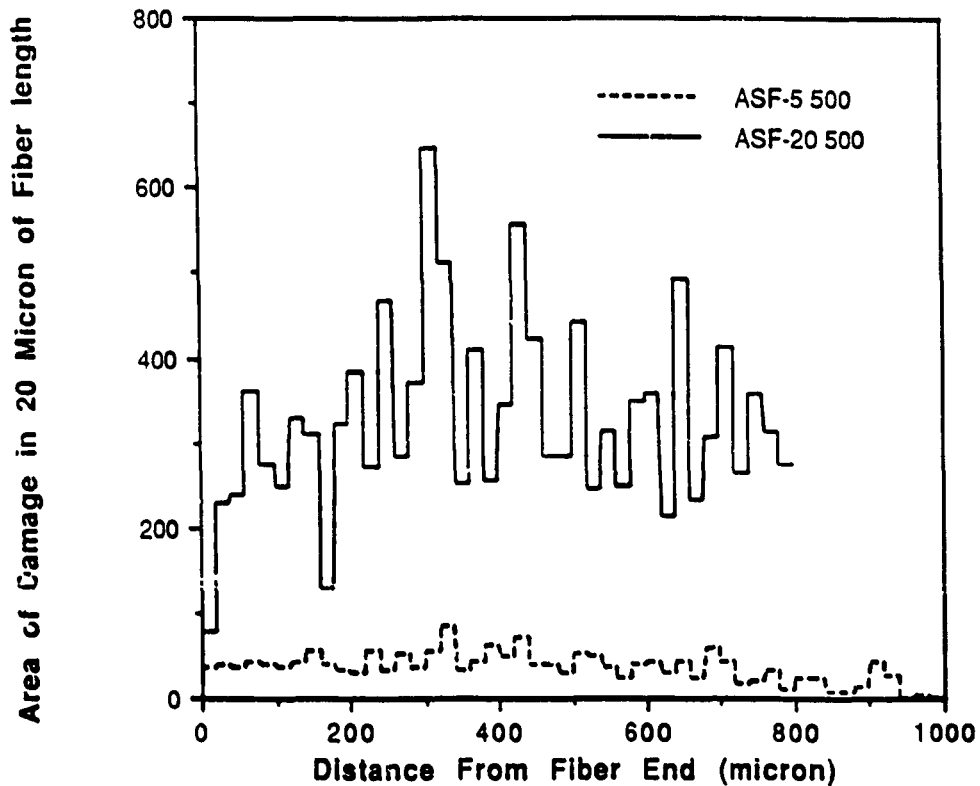


Figure 5.28 Interfacial Porosity as a Function of Distance from Fiber End, ASF-5 and ASF-20, 500 Cycle Comparison.

Figure 5.28 shows that much more damage porosity was present in the ASF-20, 500 cycle case than the ASF-5, 500 cycle case. This result indicates that fiber aspect ratio has a strong influence on the damage development process.

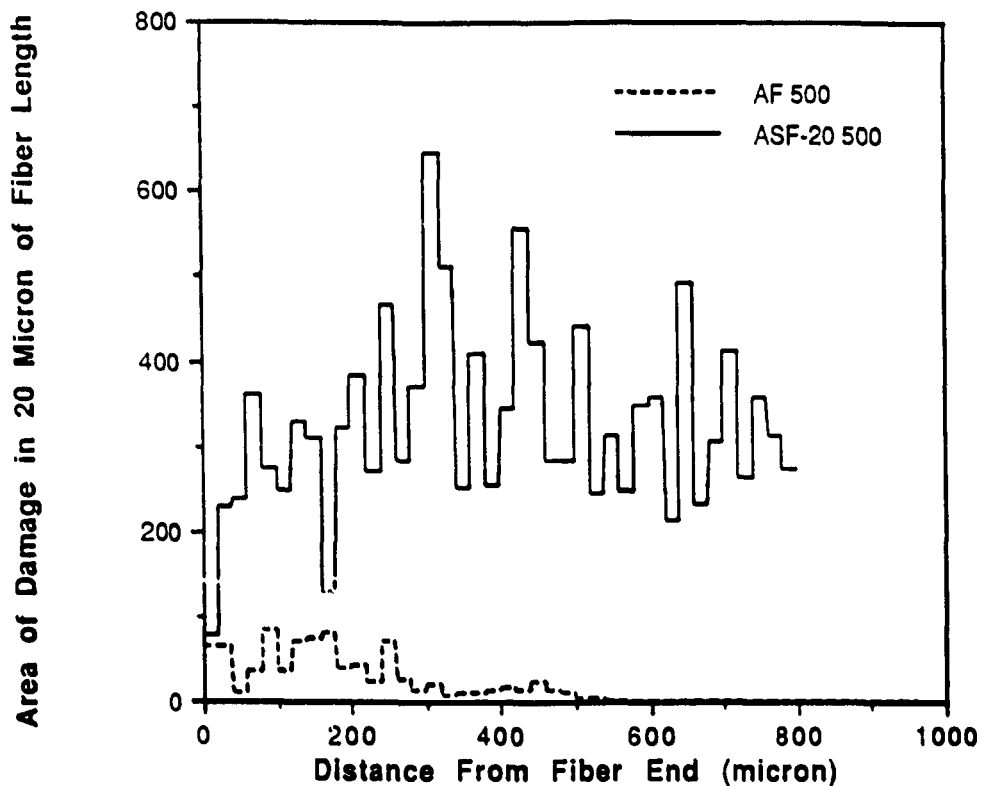


Figure 5.29 Interfacial Porosity as a Function of Distance from Fiber End, AF and ASF-20, 500 Cycle Comparison.

Figure 5.29 shows the AF hybrid specimen had significantly less damage porosity after 500 cycles than did the similar non-hybrid ASF-20 material. This indicates the addition of a small volume fraction of low expansion, small dimension whiskers can significantly delay the development of interfacial damage in these materials.

The evidence presented in this section suggests that thermal cycling induced interfacial damage accumulates in large fiber aspect ratio composite materials in the following way. The damage initiates near the fiber end at the location of maximum stress and plastic flow (Appendix A). When the initial location of interfacial damage becomes defected the locations toward the center of the fiber experience increased stress and plastic flow and become defected in turn. Locations towards the fiber end from the advancing damage front continue to develop increased porosity until they are sufficiently defected so as to preclude further changes. Figure 5.30 illustrates this process.

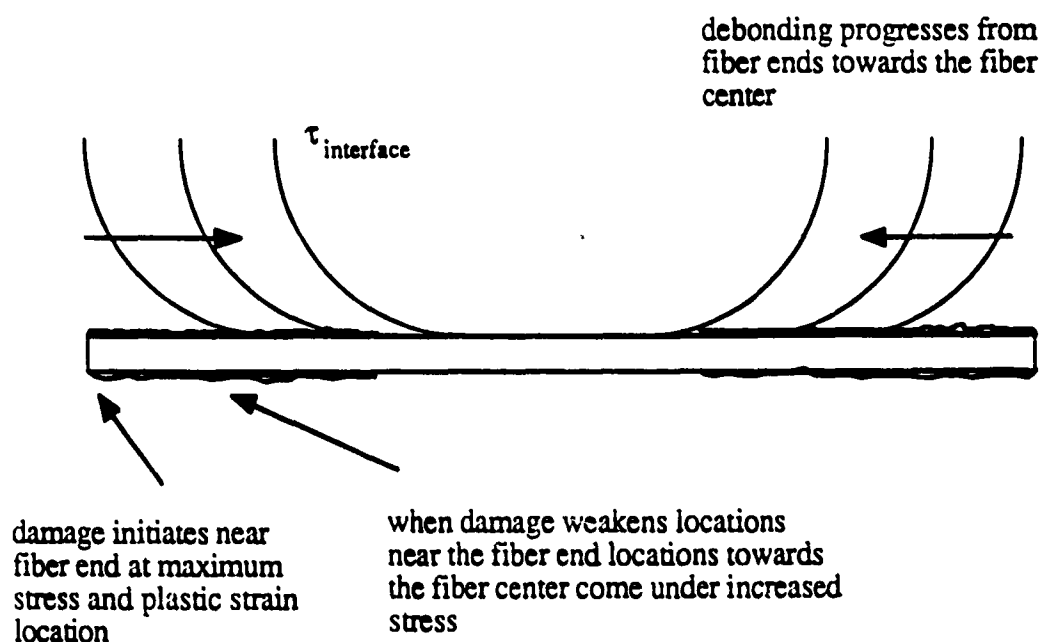


Figure 5.30 The Damage Accumulation Process.

The development of thermal cycling damage in the small aspect ratio composite was qualitatively different from the large aspect ratio composites. In this case the thermal

cycling damage was much more uniform along the fiber length. The increased uniformity can be explained with the Shear Lag Model (Appendix A), and the increased relative importance of three-dimensional effects.

Chapter 6 Mechanical Analysis

6.1 Thermal Cycling Deformation Model

As reviewed in Chapter 2 there are two important types of existing analytical models. One type models the initial stage of thermal cycling deformation when the matrix and reinforcement are well bonded (Garmong, 1974; Taya and Mori, 1987). The other type models the second stage of thermal cycling deformation when the matrix and reinforcement are free to slide (Yoda et al, 1978). In this section we will develop an analytical model to predict the dimensional change during the initial, well bonded stage. In later sections the predictions of this model will be compared to experiment, and the analysis will be generalized to include the case of composites with damaged interfaces.

The present model is an extension of the Taya-Mori model reviewed in Chapter 2. During the initial cool-down and low temperature hold time, the models are exactly the same. However, the present model differs from the Taya-Mori model during the heating process in that it accounts for high temperature plastic straining. Additionally, the present model differs from the Taya-Mori model during the high temperature hold time in that the interfacial diffusion is assumed to be negligible and the composite retains significant thermal stresses at the end of the high temperature residence time.

6.1.1 Eshelby's Model

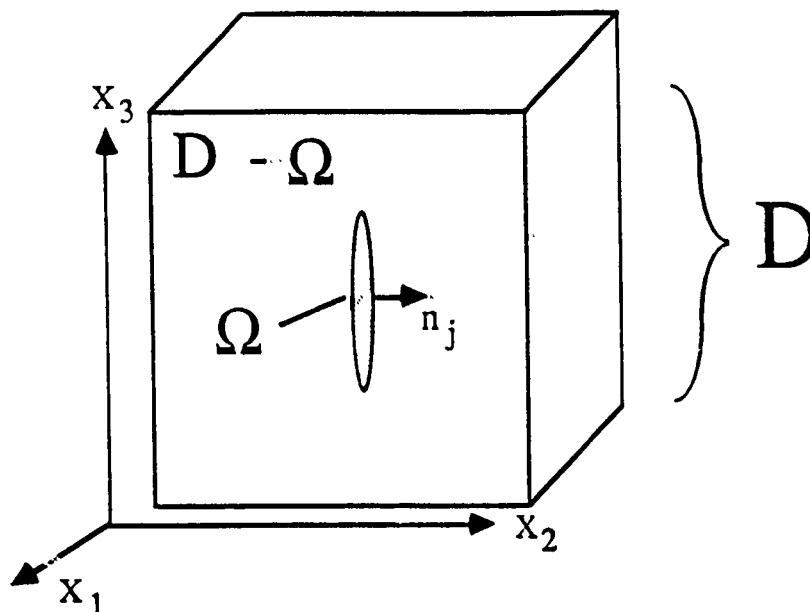


Figure 6.1 Eshelby Domains.

The analytical model developed in this chapter is based on the work of Eshelby (Eshelby, 1957). This work developed a convenient method for the calculation of the stress and strain fields in an infinite elastic solid which contained a single ellipsoidal inclusion with the same stiffness as the matrix. This inclusion assumes an inelastic strain e_{ij}^* by some plastic or thermal process. In order to calculate the elastic fields inside and outside of this inclusion after this inelastic process, the following idealized processes are used:

- i) Remove Ω from the matrix.
- ii) Allow the unconstrained transformation (e_{ij}^*) to take place in Ω . The matrix and inclusion are both stress free at this point.

- iii) Apply a surface traction $(-\sigma_{ij}^* n_j)$ to Ω to restore it to its original size and shape. Put it back into the hole in the matrix and rejoin the material across the cut. The stress is now zero in the matrix domain $(D-\Omega)$ and has a known value in the inclusion (Ω) . The surface tractions have become built in as a layer of body forces spread over the interface between the matrix and inclusion.
- iv) Remove this layer of body force by applying an equal but opposite layer of body force $(\sigma_{ij}^* n_j)$. The additional elastic field thus introduced is found by integration of the Green's Function of a point force.

The body force applied at step (iv) is related to the eigenstrain in step (ii) by:

$$\sigma_{ij}^* = C_{ijkl} e_{kl}^*$$

The displacement due to $\sigma_{ij}^* n_j$ is given by:

$$u_i(x) = \int_{\Omega} (x') \sigma_{jk}^* n_k G_{ij}(x-x') dS \quad (6.1.1)$$

where $G_{ij}(x-x')$ is Green's function, which gives the displacement at a point x along the x_i axis due to a force applied at a point x' along the x_j axis. It is given as:

$$G_{ij}(x-x') = \frac{1}{4\pi\mu} \frac{\delta_{ij}}{|x-x'|} - \frac{1}{16\pi\mu(1-\nu)} \frac{\partial^2}{\partial x_i \partial x_j} |x-x'| \quad (6.1.2)$$

where ν and μ are Poisson's ratio and the shear modulus of the matrix respectively.

After applying the Gauss divergence theorem to equation (6.1.1) and using equation (6.1.2) and with significant manipulation the displacement can be written as:

$$u_i(\mathbf{x}) = \frac{x_m e_{jk}^*}{8\pi(1-\nu)} \int_{\Sigma} \frac{\lambda_m g_{ijk}}{g} dw$$

where:

$$\lambda_m = \frac{l_m}{a_m^2} \text{ no summation over } m$$

$$g = \frac{l_1^2}{a_1^2} + \frac{l_2^2}{a_2^2} + \frac{l_3^2}{a_3^2}$$

$$l_i = \frac{x_i' - x_i}{|\mathbf{x}' - \mathbf{x}|}$$

$$g_{ijk}(l) = (1 - 2\nu)(\delta_{ij} l_k + \delta_{ik} l_j + \delta_{jk} l_i) + 3l_i l_j l_k$$

and dw is a surface element of a unit sphere Σ centered at a point \mathbf{x} . The corresponding strain is:

$$e_{ij} = S_{ijkl} e_{kl}^* \quad (6.1.3)$$

$$\text{where } S_{ijkl} = \frac{1}{16\pi(1-\nu)} \int_{\Sigma} \frac{\lambda_i g_{jkl} + \lambda_j g_{ikl}}{g} dw.$$

S_{ijkl} is known as Eshelby's tensor and is tabulated in Appendix A.

The strain in the inclusion is the sum of the inelastic strain, $-e^*_{ij}$, and the strain due to the opposite layer of body force, e_{ij} .

$$\sigma_{ij}^I = C_{ijkl} (e_{kl} - e_{kl}^*). \quad (6.1.4)$$

Therefore, the stress in the inclusion can be easily obtained from equations (6.1.3) and (6.1.4) if e_{ij}^* is known.

If the inclusion has a different stiffness than the matrix, the subdomain (Ω) is called an "inhomogeneity". If the inhomogeneity also contains an eigenstrain, it is called an "inhomogeneous inclusion". Eshelby showed that by replacing the inhomogeneity of stiffness C_{ijkl}^I by a homogeneity of stiffness C_{ijkl} and a fictitious eigenstrain e_{ij}^* the inhomogeneous inclusion problem can be solved easily.

6.1.2 Analytical Model for Thermal Cycling Strain

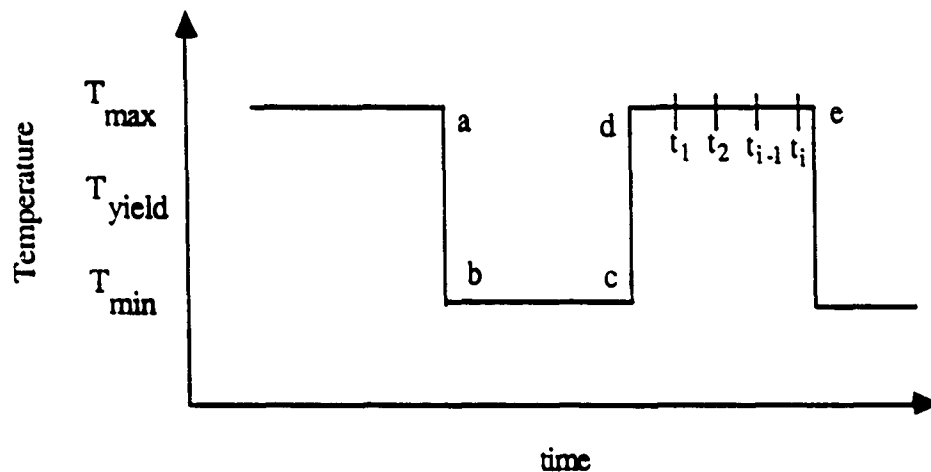


Figure 6.2 Idealized Time-Temperature Excursion Curve.

The particular equivalent inclusion problem of interest to this study occurs when a composite is subjected to a number of thermal cycles like the one shown in Figure

6.2. In beginning this formulation it is assumed that the composite has resided at high temperature sufficiently long to become stress free. The formulation which follows is exactly the same as in the Taya-Mori Thermal Cycling Model until the heating process, c to d.

Cool-down Process a to b:

It is intuitively clear that because the reinforcement of the composite has a different stiffness and coefficient of thermal expansion from that of the matrix an internal average matrix stress will appear when the composite is cooled from a to b. This average matrix stress in this composite is given by

$$\overline{\sigma_{D-\Omega}} = C_m \bar{e} \quad (6.1.5)$$

where C_m is the matrix stiffness tensor, and \bar{e} denotes the average strain in the matrix caused by the presence of the reinforcement. Now let one particular reinforcing fiber be considered the ellipsoidal inhomogeneity. The stress in this particular fiber is given by

$$\sigma = C_f (\bar{e} + e - \alpha^*) \quad (6.1.6)$$

where α^* is given by

$$\alpha^* = (\alpha_f - \alpha_m, \alpha_f - \alpha_m, \alpha_f - \alpha_m, 0, 0, 0) \{T_L - T_H\}$$

Using Eshelby's equivalent inclusion method allows the stress in the fiber to be rewritten as

$$\sigma = C_m (\bar{e} + e - e^*) \quad (6.1.7)$$

Using the definition of Eshelby's tensor given in Equation 6.3, the stress in the fiber can now be written as

$$\sigma = C_m \left\{ \bar{e} + (S - I) (e^*) \right\} \quad (6.1.8)$$

or using the fiber elastic modulus tensor

$$\sigma = C_f \left\{ \bar{e} + S e^* - \alpha^* \right\} \quad (6.1.9)$$

Since the thermal stress must be self-equilibrating within the composite

$$\int_D \sigma \, dV = 0 \quad (6.1.10)$$

with some derivation one can write

$$\bar{e} + f (e - e^*) = 0 \quad (6.1.11)$$

where f is the volume fraction of fiber. Using equations (6.1.8), (6.1.9), and (6.1.11) we can write

$$C_f \alpha^* = (C_f - C_m) \cdot \left\{ (1 - f) S e^* + f e^* \right\} + C_m e^* \quad (6.1.12)$$

from which e^* can be computed. Once e^* is found the averaged elastic temperature stress can be found in the matrix and the fiber as

$$\bar{\sigma}_m = -f C_m (S e^* - e^*) \quad (6.1.13)$$

$$\bar{\sigma}_f = (1 - f) C_m (S e^* - e^*) \quad (6.1.14)$$

The stresses just outside the fiber can be found as

$$\sigma_{pq}^{(out)} = \sigma_{pq}^{in} + C_{pqmn} \left\{ -C_{klj} \left(e_{ij}^* + \alpha_{ij}^* \right) n_1 n_2 \frac{(\lambda + 2\mu) \delta_{km} - (\lambda + \mu) n_k n_m}{\mu(\lambda + 2\mu)} + e_{mn}^* + \alpha_{mn}^* \right\} \quad (6.1.15)$$

It is reasonable to expect that if the temperature change is large enough, plastic deformation will occur in the matrix. In order for the matrix to yield, the Von Mises yield criterion must be satisfied. It is given by

$$\frac{3}{2} \overline{\sigma^{total}_m} \overline{\sigma^{total}_m} = Y^2 \quad (6.1.16)$$

where σ^{total} at the initiation of yielding is the elastic stress due to temperature change. The uniaxial composite case gives rise to a transversely isotropic stress state, therefore the yield criterion can be greatly simplified to

$$\overline{\sigma_3^{total}} - \overline{\sigma_1^{total}} = Y \quad (6.1.17)$$

Since the average stress deviator is a linear function of ΔT the critical temperature drop at which the average matrix stress meets the yield surface can be easily calculated. The calculation of the plastic strain at T_{min} requires the definition of two additional quantities: e^{*P} , the eigenstrain associated with plastic deformation; and e^P , the longitudinal plastic strain. e^P has the form of

$$\vec{e}^P = e^P \left\{ -1/2, -1/2, 1, 0, 0, 0 \right\}_1 \quad (6.1.18)$$

In an equation similar to equations (6.1.6) and (6.1.7) one can find the stress due to the plastic strain in the fiber in terms of the matrix or fiber stiffness tensors.

$$C_f \left\{ -f \left[S e^{*P} - e^{*P} \right] + S e^{*P} + e^{*P} \right\} = C_m \left\{ -f \left[S e^{*P} - e^{*P} \right] + S e^{*P} - e^{*P} \right\} \quad (6.1.19)$$

Equation (6.1.19) is solved explicitly for e^{*P} in terms of e^P . This result is then substituted in an equation completely analogous to equation (6.1.14).

$$\overline{\sigma}^P = -f C_m \left\{ S e^{*P} - e^{*P} \right\} \quad (6.1.20)$$

This result is then used in the yield function definition

$$\left\{ \overline{\sigma}_3 + \overline{\sigma}_3 \right\} - \left\{ \overline{\sigma}_1 + \overline{\sigma}_1 \right\} = Y \quad (6.1.21)$$

Using the above substitutions equation (6.1.21) is then solved explicitly for e^P .

Heating Process, c to d:

As the composite is heated from c to d the negative of the elastic temperature stress calculated in equation (6.1.13) is applied. This heat-up stress is superimposed on the stress state existing after the cool-down plastic yielding. The result of the superimposition is a stress state equal to the stress due to low temperature plastic yielding. Often this stress state will be outside of the matrix yield surface since the stress due to yielding can be larger than the yield surface, and since yield surfaces generally become smaller with increasing temperature. Therefore a high temperature yield strain, e^{HTP} , is calculated the same way as the low temperature yield strain, e^P . In this way Equation (6.2.22) provides a solution to the plastic strain which will bring the matrix flow stress onto the high temperature yield surface.

$$\left\{ \overline{\sigma}_3 + \overline{\sigma}_3 \right\} - \left\{ \overline{\sigma}_1 + \overline{\sigma}_1 \right\} = Y_{High Temp} \quad (6.1.22)$$

High Temperature Hold Process, d to e:

At the completion of the high temperature plastic straining the composite will sustain stresses which lie on the high temperature yield surface. These stresses will in general relax by creep. To calculate the creep behavior, the incremental Dorn Creep Law is used.

$$\Delta e^c(t_i) = - \left\{ A \left(\frac{\sigma_m(t_{i-1})}{G} \right)^n \frac{G b D_o}{(\kappa T_H)} \exp \frac{-Q_v}{R T_H} \right\} \Delta t \quad (6.1.23)$$

A fictitious eigenstrain corresponding to this incremental creep strain can be calculated by

$$C_m \cdot \Delta e^c = (C_f - C_m) \cdot \left\{ (1-f) S e^* + f e^* \right\} + C_m e^* \quad (6.1.24)$$

where

$$\vec{\Delta e^c} = \left\{ \frac{-\Delta e^c(t_0)}{2}, \frac{-\Delta e^c(t_0)}{2}, e^c(t_0), 0, 0, 0 \right\}$$

The incremental stress response is now found in the x_3 and x_1 directions using

$$\Delta \sigma_m(t_1) = -f C_m \cdot (S e^* - e^*) \quad (6.1.25)$$

The incremental flow stress is now calculated and this new incremental flow stress is added to the flow stress at the start of the cycle increment, and the incremental creep

strain is added to the existing creep strain. Finally the new flow stress is calculated and the process is repeated until the finish of the high temperature residence time.

The longitudinal, and lateral thermal cycle strain is now found as the product of the matrix volume fraction and the sum of the strains due to; cool-down plasticity, heat-up plasticity, and creep.

$$e_L = \{1 - f\} \{e^P + e^{HTP} + e^C\} \quad (6.1.26)$$

At the finish of the first high temperature hold time a residual stress state will in general exist. These residual stresses will superimpose with the elastic cool-down stresses during the second cool-down cycle. The effect of these stresses is to reduce the magnitude of the plastic cool-down strain. Since the low temperature yield function is assumed to remain constant, the initial conditions for the following heating cycle remain the same. Therefore the magnitudes of the high temperature plastic strain and the high temperature creep strain will be the same as in the first cycle. The net effect of the initial residual stresses is to reduce the net strain accumulation in the second and all subsequent thermal cycles. The total deformation strain accumulated by the composite is the number of thermal cycles times the strain deformation computed in the second thermal cycle.

$$\epsilon_L^{N \text{ thermal cycles}} = N \epsilon_L^{\text{second thermal cycle}} \quad (6.1.27)$$

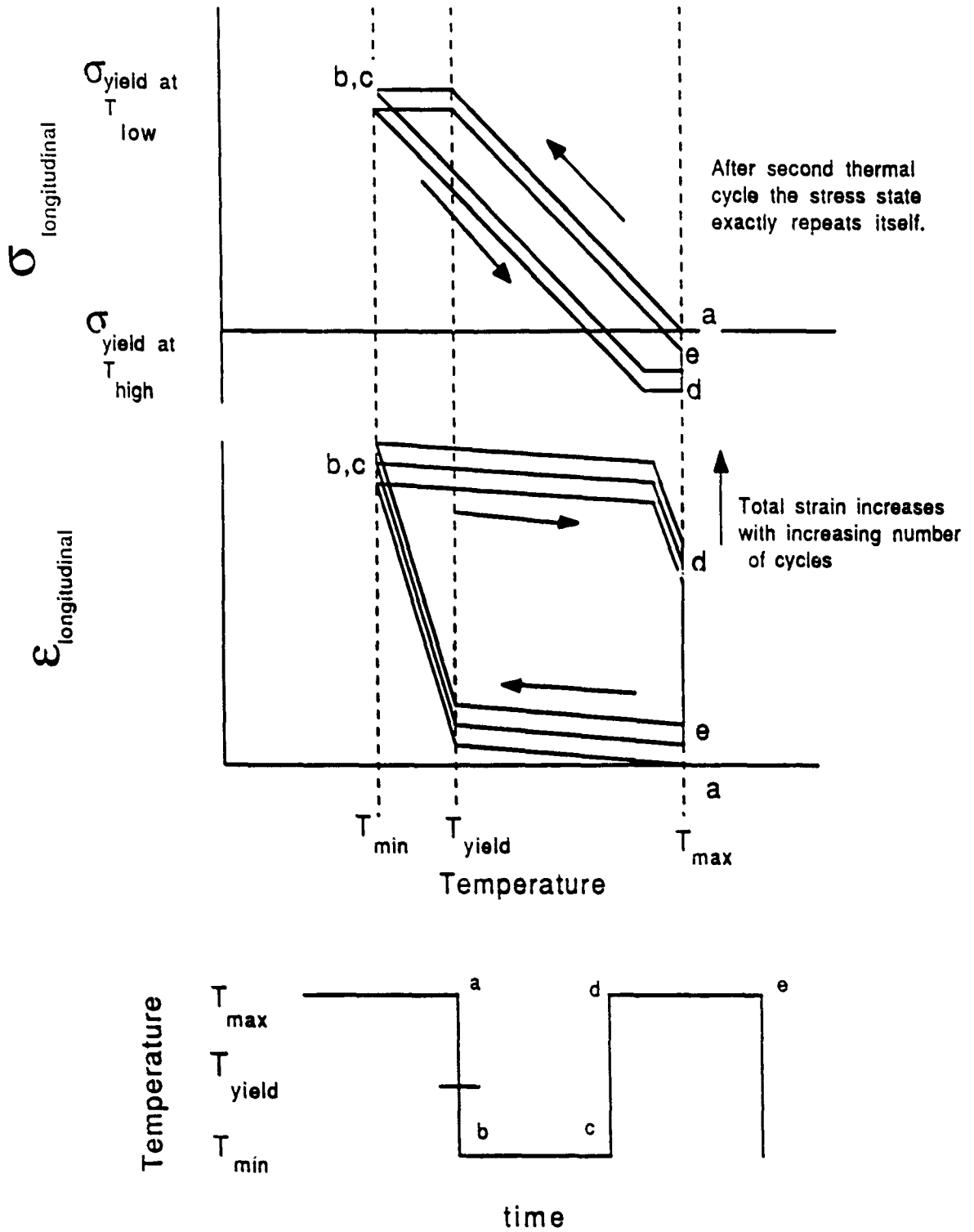


Figure 6.3 Model Stress and Strain versus Temperature Behavior.

Figure 6.3 shows the average matrix longitudinal stress and strain as a composite is thermal cycled. The composite originally starts at zero stress at high temperature. If the composite behaved perfectly elastically a high stress would develop in the matrix. The matrix cannot support this level of stress however so the matrix plastically yields. The difference between the stress obtained in an ideal elastic matrix and the yield stress of the matrix is called the stress due to yielding. When the composite is again raised to the original high temperature the negative of the cool-down elastic temperature stresses are applied to the composite. At this point if no low temperature plastic yielding has occurred the composite would be at zero stress and strain. However if low temperature plastic yielding has occurred then the stress state in the composite will be equal to the stress due to yielding. If this stress is outside the high temperature yield surface, a reverse high temperature plastic yielding occurs. After the high temperature plastic yielding has occurred creep processes reduce the composite stress and strain further. In general some residual stresses will remain in the composite at the completion of the high temperature residence time. As the composite is again cooled from high temperature these residual stresses will superimpose on the elastic temperature stresses. The second thermal cycle stress due to yielding will be less than in the first cycle case and so will be the amount of plastic yielding. When the composite is again heated to high temperature the same negative of the cool-down elastic temperature stress is applied as in the first cycle case. Therefore the same high temperature plastic strains, and high temperature creep strains are experienced in the second cycle as in the first. As the composite is given additional thermal cycles the second thermal cycle stress and strain values repeat.

One important prediction made by the model is that the amount of thermal cycling strain will be zero if the material is at very high temperature and plastic and creep strains eliminate all residual stresses. In this case the composite returns to the original configuration after each cycle and no additive strains result. However, if the homologous temperature of the matrix is decreased, greater residual stresses are retained. Therefore the model predicts that even if the low cycle temperature is held constant the strain per thermal cycle will increase if the maximum cycle temperature is

decreased. This is true unless high cycle temperature is reduced by too large an amount. In this case the rate of thermal cycling strain will again be zero since the thermal strains are elastic.

6.2 Comparison of Present Model with Previous Models

In this section the results of the three different models examined in this thesis are compared. The one-dimensional nature of the Garmong model limits a direct comparison to the continuous fiber case. The specific material properties used for each model are given in Tables 6.1 and 6.2.

Table 6.1 Garmong Model Input Parameters

$\alpha_m - \alpha_f$	= $10 \times 10^{-6} / K$
V_f	= 0.5
E_m	= $6.9 \times 10^4 \text{ MN/m}^2$
E_f	= $2.1 \times 10^5 \text{ MN/m}^2$
σ_0	= $56.0 - 0.07 * T$
K^*	= 690 MN/m^2
n	= 0.5
G	= 2.62×10^4
s	= 4.4
$D_0 A G b / k$	= $3.1 \times 10^{26} / s$
Q/R	= 17,600 K
T_{max}	= 700 K
T_{min}	= 300 K
T_{max} hold time	= 60 seconds

Table 6.2 Taya-Mori and Present Model Input Parameters

α_m	= 24.7 x 10 ⁻⁶ / K
α_f	= 14.7 x 10 ⁻⁶ / K
v_f	= 0.33
v_m	= 0.17
V_f	= 0.5
E_m	= 6.9 x 10 ⁴ MN/m ²
E_f	= 2.1 x 10 ⁵ MN/m ²
$\sigma_{0\ Tmin}$	= 35 MN/m ²
$\sigma_{0\ Tmax}$	= 7.0 MN/m ²
G	= 2.62 x 10 ⁴
s	= 4.4
D_0AGb/k	= 3.1 x 10 ²⁶ /s
Q/R	= 17,600 K
T_{max}	= 700 K
T_{min}	= 300 K
T_{max} hold time = 60 seconds	
Fiber Aspect Ratio = 1000.	

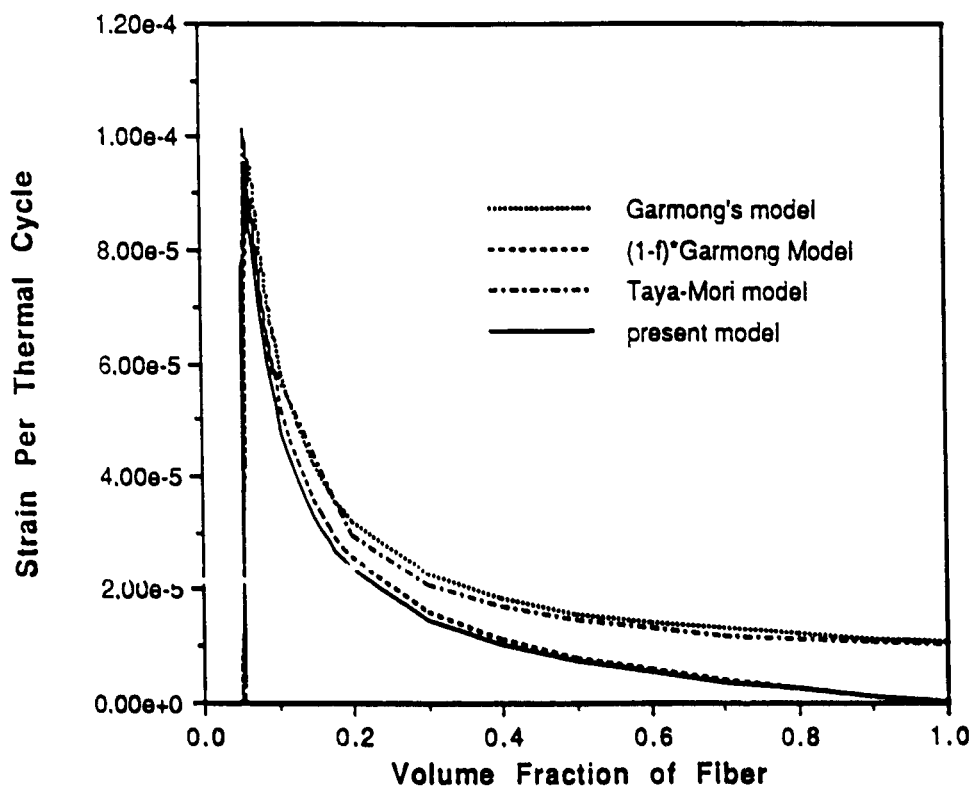


Figure 6.4 Comparison of Present Model with Computed Garmong Result.

In Figure 6.4 the three models considered in this thesis, and the product of the matrix volume fraction with the Garmong model result are compared. The product of the matrix volume fraction and Garmong's result was included since this result would naturally follow the derivation of the Present Model and the Taya-Mori model. Figure 6.4 shows that the three models give very similar results at low fiber volume fractions. The Taya-Mori model and Garmong model have a close agreement for the entire range of fiber volume fraction. Likewise the present model and the product of the matrix volume fraction and Garmong's model have a close agreement for the entire range of fiber volume fraction. The most significant disagreement occurs at a

fiber volume fraction of one. The Taya-Mori and Garmong result predict a non-zero value, while the Present Model and the product of the matrix volume fraction and Garmong's model predict a zero value.

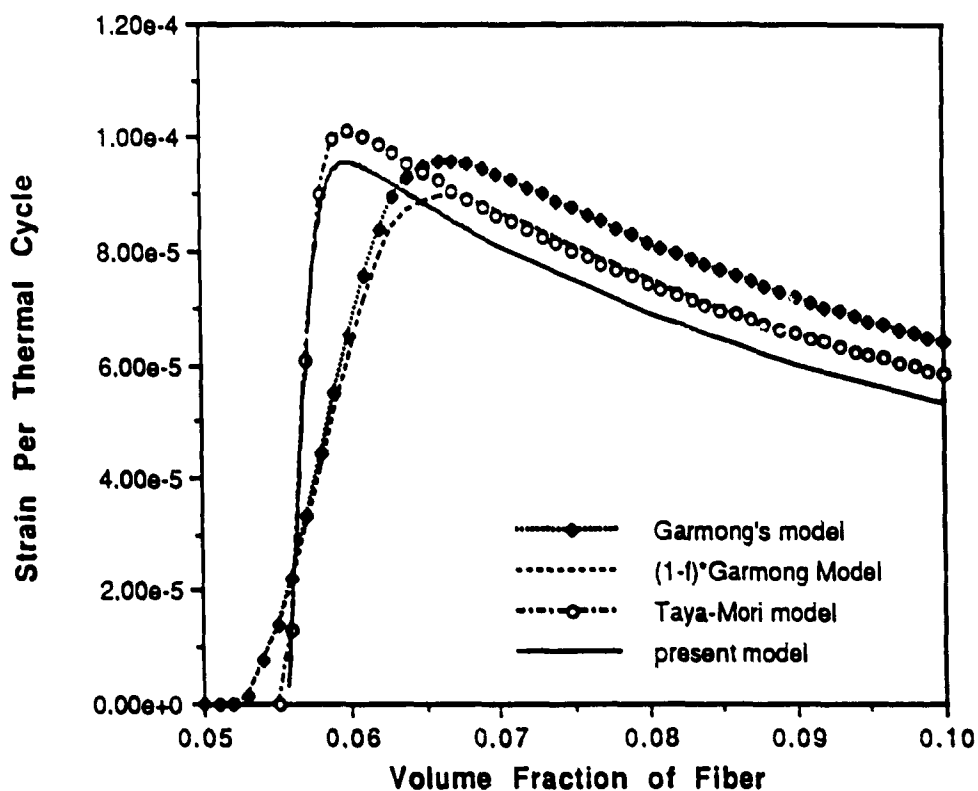


Figure 6.5 Expanded View of Figure 6.4.

Figure 6.5 shows an expanded view of the low fiber volume fraction range of Figure 6.4. It shows that for this set of input parameters the three models are in close agreement for the critical fiber volume fraction needed to initiate thermal cycling deformation. This figure also shows that the initial rise in predicted strain per thermal

cycle is sharper in the Taya-Mori and Present Model cases than in the Garmong model case.

Because the Garmong Model and the Present Model account for the same mechanical processes during a thermal cycle very close agreement can be expected between the Present Model and the product of the matrix volume fraction and the Garmong Model when the fiber aspect ratio is large. The models can be expected to give increasingly different results as the fiber aspect ratio is decreased and three dimensional effects becomes more important. The largest disagreement between the models occurs at a fiber aspect ratio of one when the Present Model predicts zero thermal cycling strain while the Garmong Model would give the same result as in the continuous fiber case. While the Garmong Model was formulated for an arbitrary heating and cooling rate the Present Model was specialized to an instantaneous heat-up or cool-down, steady temperature, time-temperature history. This is not a limitation on the Present Model however since any arbitrary time-temperature trajectory can be approximated as a finite sum of instantaneous heat-up or cool-down, steady temperature events.

The Present Model result is very nearly equal to the product of the matrix volume fraction times the Taya-Mori model result in Figure 6.5. Recall that the present model result is

$$(1-f) (e_p + e_{htp} + e_c) \quad (6.2.1)$$

while the Taya-Mori result is given as

$$(e_p + e_c) \quad (6.2.2)$$

without high temperature plastic strain being calculated. Figure 6.6 shows the stress relief result of the Taya-Mori Model. Because the stress relief is so rapid the creep strain calculated in the Taya-Mori Model is very nearly equal to the sum of the high temperature plastic strain and creep strain calculated in the Present Model. Because of this the model results differ by a factor of $1-f$. The Taya-Mori Model and the Present Model will have increasingly similar results as the matrix creep becomes

more rapid, and the fiber volume fraction decreases. The models give increasingly different results as the matrix creep becomes less rapid, and the fiber volume fraction increases. Therefore the largest difference in results predicted by the two models would occur in the case of a high volume fraction composite thermal cycled between two low temperatures.

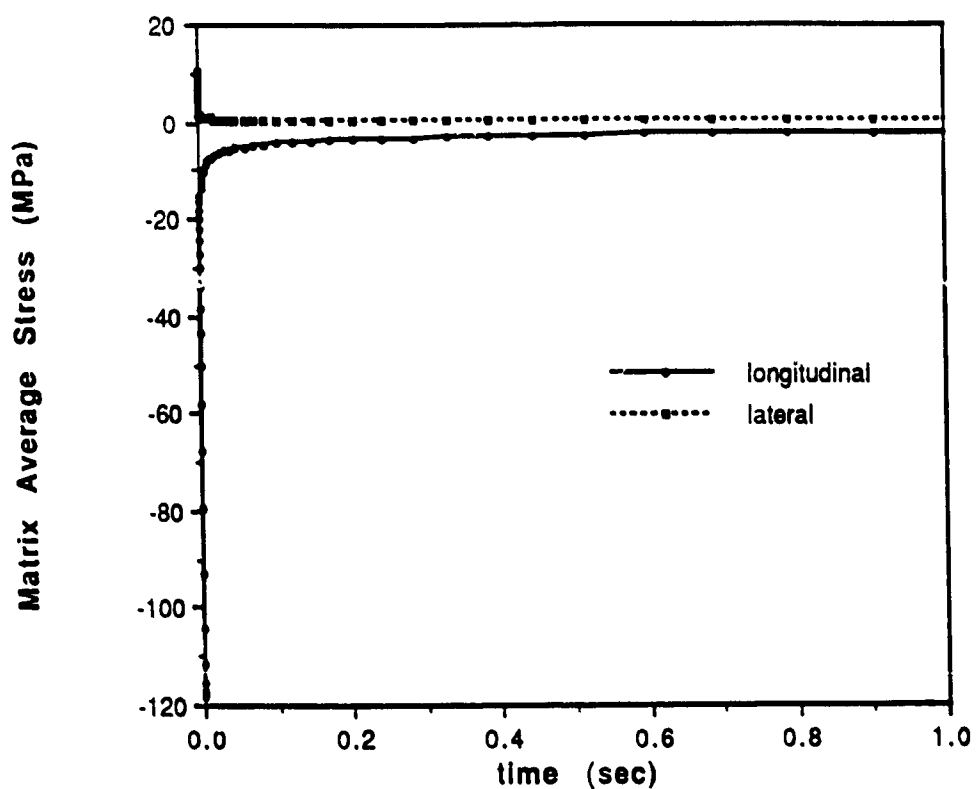


Figure 6.6 Taya-Mori Stress Relaxation.

6.3 Comparison of Present Model with Experiment

6.3.1 W-1%ThO₂ Reinforced 67Fe-24Cr-8Al-0.5Y

Table 6.3 Input Data for W-FeCrAlY

67Fe-24Cr-8Al-0.5Y

Young's Modulus	2.01 E 5 MPa
Poisson's Ratio	0.33
Coefficient of Thermal Expansion	26.1 E-6 /C°
Uniaxial Yield Stress	220 MPa
High Temperature Uniaxial Yield Stress	6.9 MPa
High Temperature Shear Modulus	2.88 E 4 MPa
Creep Constant	1.66 E 25
Power Law Exponent	6.09

W-1%ThO₂

Young's Modulus	3.58 E 5 MPa
Poisson's Ratio	0.285
Coefficient of Thermal Expansion	4.75 E -6 /C°
Aspect Ratio	5
Volume Fraction of Fiber	0.30 or 0.20

Thermal Cycle

T _{max}	1100 C
T _{min}	352 or 534 C
Del T	-748 or -566 C
High Temperature Hold Time	360 sec.

In gathering input data for the model it was discovered that the scientific literature is lacking in detailed information about the mechanical properties of FeCrAlY. The literature did, however, explicitly state that the high temperature properties of FeCrAlY are very similar to stainless steel (Wukusick and Collins, 1964). Therefore when information on a particular property was unavailable a value from a stainless steel was used. Following this policy the data in Table 6.3 was obtained from a variety of sources. The value for the Uniaxial Elastic Modulus came from room temperature tensile tests discussed earlier in this thesis. The value for Poissons Ratio is that typical for stainless steels. The Coefficient of Thermal Expansion and the Yield Strength as a function of temperature were given in Wukusick and Collins, 1964, for a 70 Fe-25 Cr-4 Al-1Y alloy. The Wukusick and Collins data for high temperature yield stress is shown in Figure 6.7. The high temperature shear modulus value was given in Ashby and Frost, 1982, for a 316 stainless steel at 1100 C.

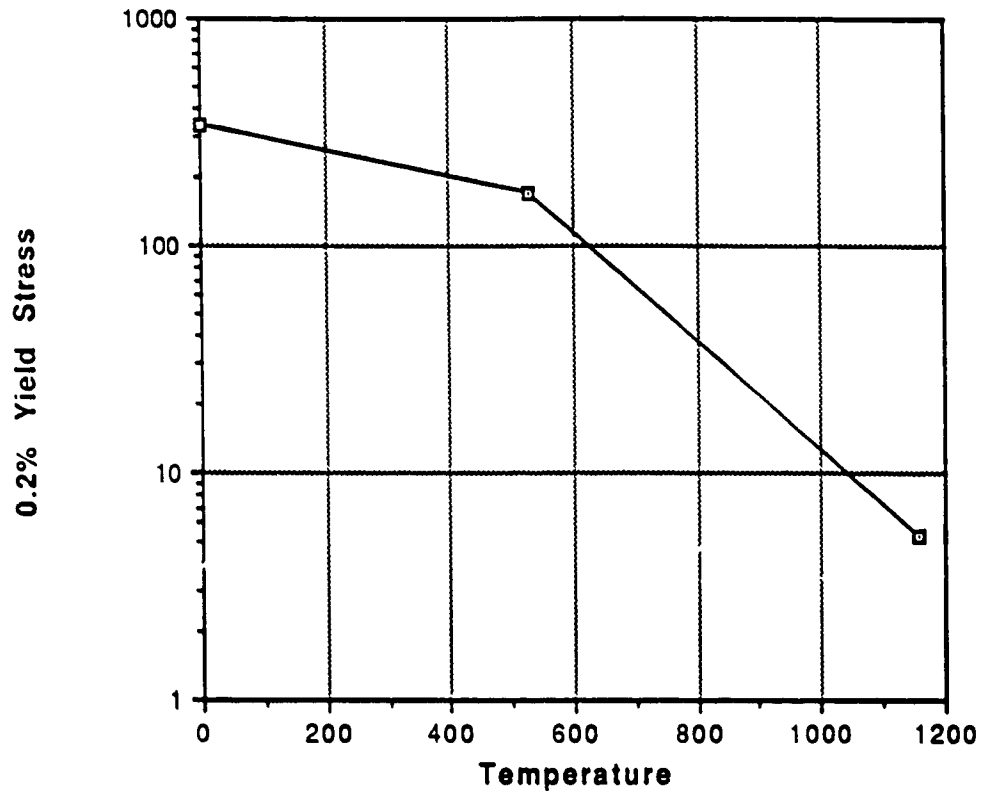


Figure 6.7 0.2% Yield Stress Versus Temperature for FeCrAlY (from Wukusick and Collins, 1964)

Table 6.4 Creep Data for FeCrAlY (ref. Saller et al, 1954)

<u>Cr</u>	<u>Al</u>		<u>Temp. C</u>	<u>Stress MPa</u>	<u>Creep Rate %/hr</u>
25	5		1204	1.38	2.07
25	5	5 Nb	1204	3.45	2.9
25	5	5 Nb	1204	2.76	0.34
25	5	5 Nb	1204	1.90	0.143
25	5	5 Nb	1204	1.38	0.006

The creep behavior of the FeCrAlY matrix was approximated using data found in a 1954 Battelle Memorial Institute study (Saller et al, 1954). This data is given in Table 6.4. To find the parameters of Equation (6.3.1), the 25Cr-5Al-5Nb data was fitted with a regression to determine the power law exponent n . The creep constant K was then found with the single 25Cr-5Al data point.

$$\dot{\epsilon} = K \left\{ \frac{\sigma}{G} \right\}^n \quad (6.3.1)$$

The model input data for the W-1%ThO₂ reinforcement was more readily available. The value for the Uniaxial Elastic Modulus was found in Harris and Ellison, 1966. The values for Poissons Ratio and the Coefficient of Thermal Expansion were obtained in Touloukian et al, 1967.

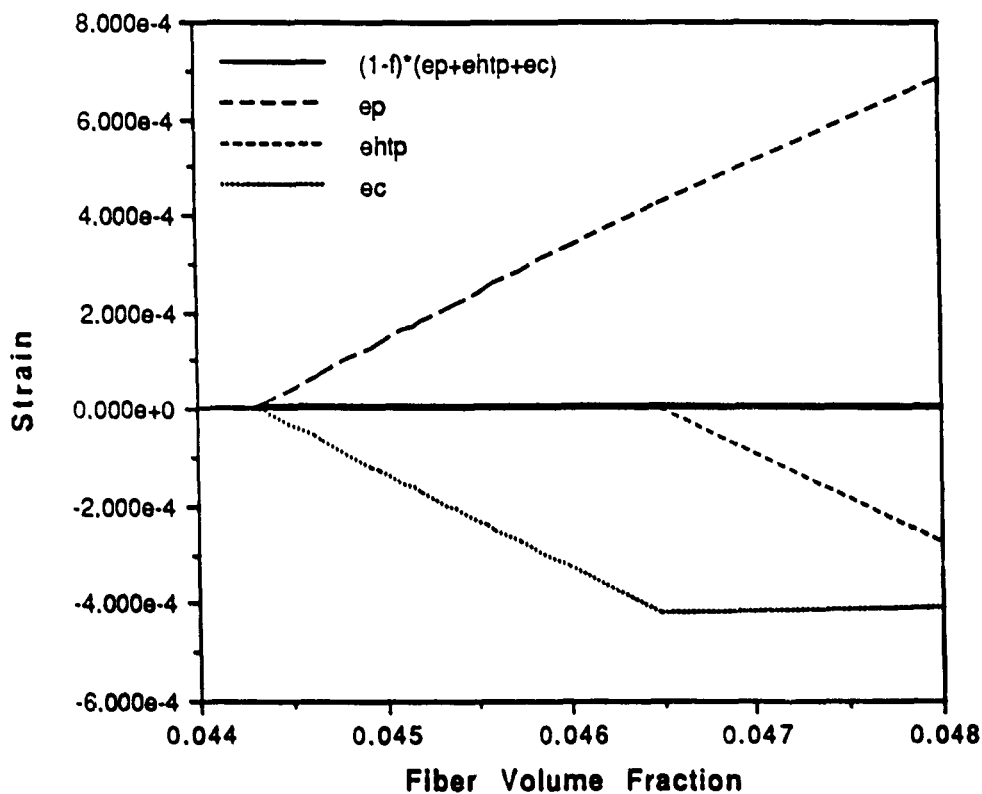


Figure 6.8 Model Strain Components versus Fiber Volume Fraction.

Figure 6.8 shows the four strain components of the model as a function of fiber volume fraction for the ASF-20, 1100-352 C case. In this figure one can see the initiation of low temperature plastic straining occurs at a fiber volume fraction of 0.044. As the fiber volume fraction is increased the flow stress in the matrix at the start of the high temperature residence time increases, and the amount of creep strain grows larger. At a fiber volume fraction of 0.047 the flow stress calculated at the completion of the heat-up event is as large as the yield surface and high temperature plastic straining begins.

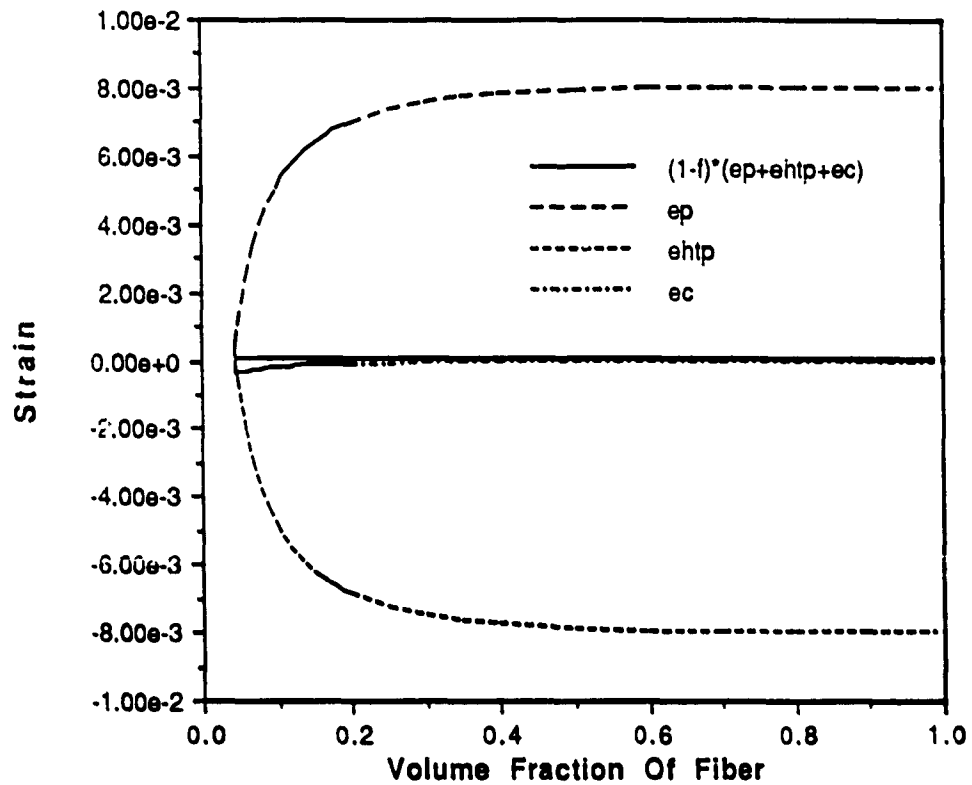


Figure 6.9 Model Strain Components versus Fiber Volume Fraction.

Figure 6.9 extends the domain of Figure 6.8 to a fiber volume fraction of 1.0. In this figure one can see that the final strain per thermal cycle prediction is very small in comparison to the magnitudes of the computed matrix strains. One can also see in this figure that the matrix plastic strains grow rapidly when the fiber volume fraction is small but then attain a nearly constant value as the fiber volume fraction is increased from 0.6. Finally the figure shows that the creep strain is larger at small volume fractions than at high volume fractions.

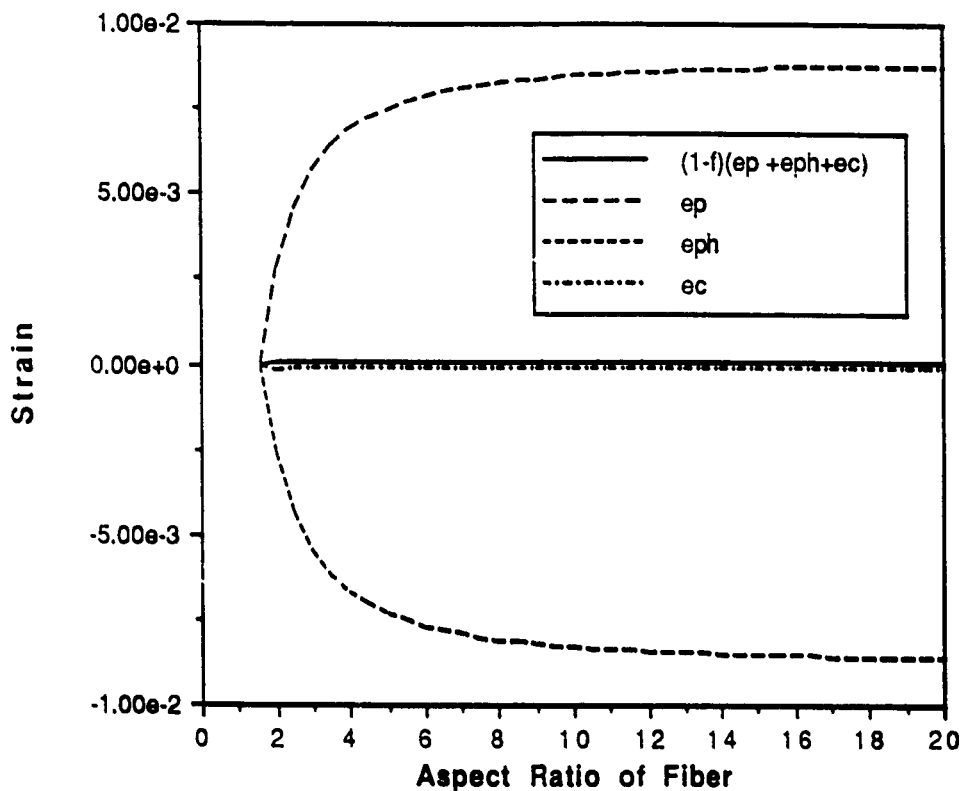


Figure 6.10 Model Strain Components Versus Fiber Aspect Ratio.

Figure 6.10 shows that when the fiber volume fraction is held constant and the fiber aspect ratio is increased the model behavior is similar to that shown in Figure 6.9. In this case zero plastic strain occurs until the fiber aspect ratio reaches a critical value larger than one. No plastic straining would be expected at a fiber aspect ratio of one since at that aspect ratio the average matrix stress is hydrostatic. The amount of plastic strain rapidly increases between an aspect ratio of two and four, and then little change results from further increase. In this figure little creep strain occurs at any value of fiber aspect ratio.

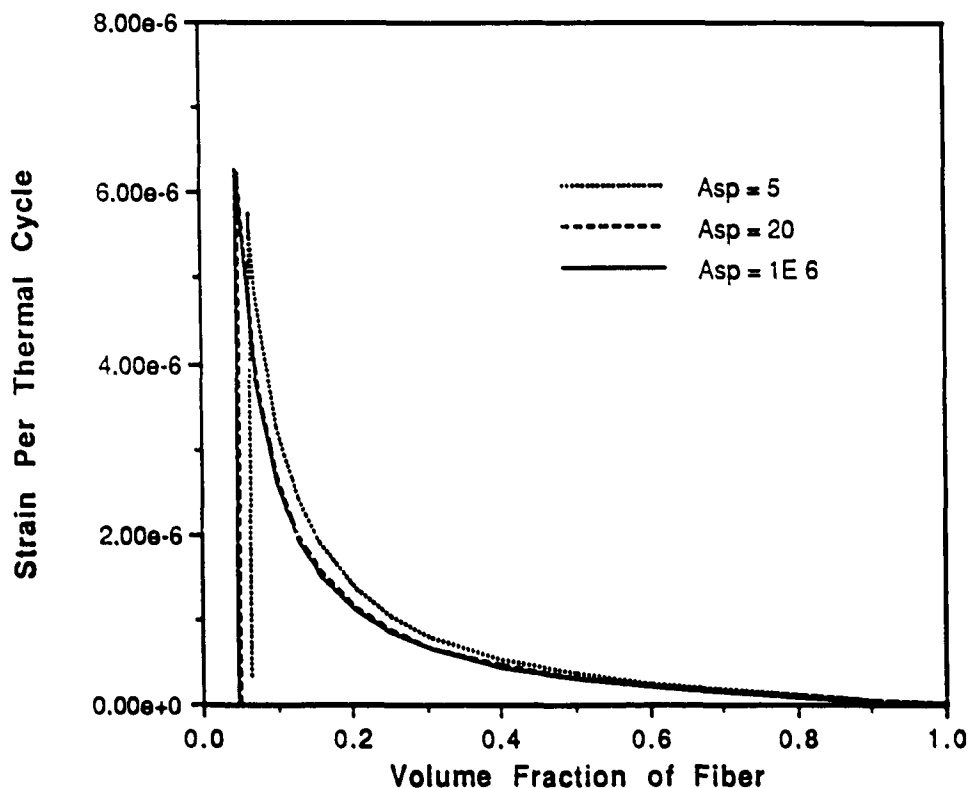


Figure 6.11 Strain Per Thermal Cycle Versus Fiber Volume Fraction.

Figure 6.11 shows the predicted strain per thermal cycle as a function of fiber volume fraction for three different fiber aspect ratios. Here one can see that the critical fiber volume fraction needed to initiate straining is larger in the aspect ratio 5.0 case than in larger aspect ratio cases. Also evident in this figure is the very close agreement between the fiber aspect 20 and the continuous fiber result. Finally the model predicts a slightly larger strain per thermal cycle in the aspect ratio 5.0 case than in the larger aspect ratio cases. However, the difference between the results is so small an experimental verification of this prediction would be impossible.

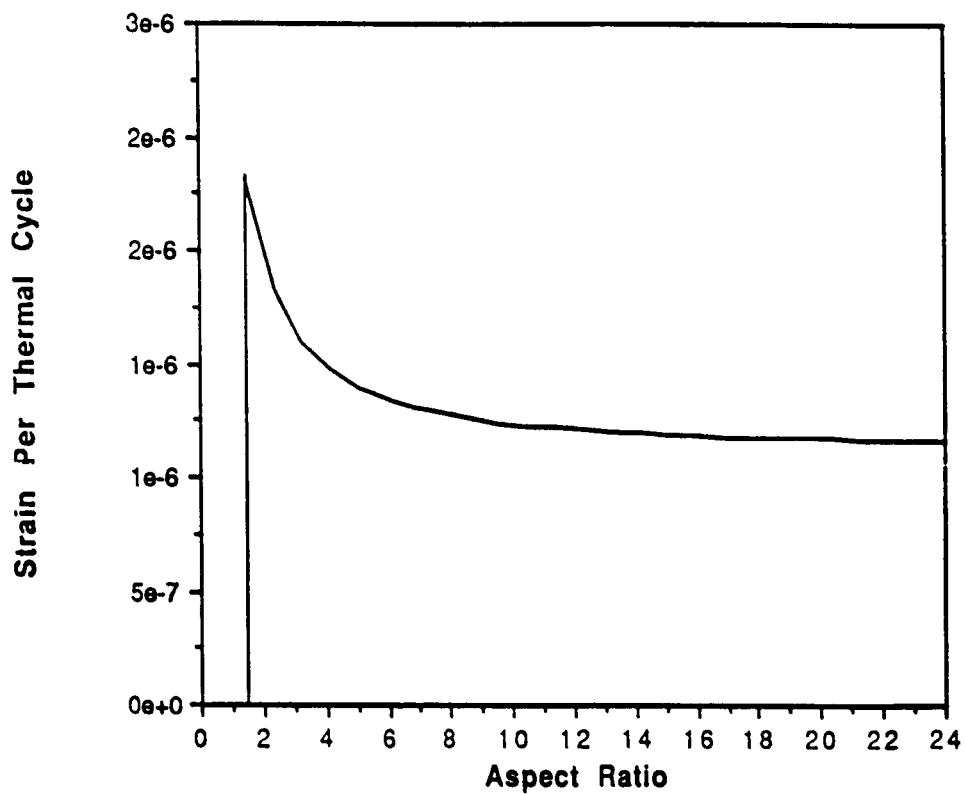


Figure 6.12 Strain Per Thermal Cycle Versus Fiber Aspect Ratio.

Figure 6.12 shows the model prediction for a constant 0.2 fiber volume percent composite as the fiber aspect ratio is changed. After an initial sharp increase the prediction becomes constant as the fiber aspect ratio increases to infinity.

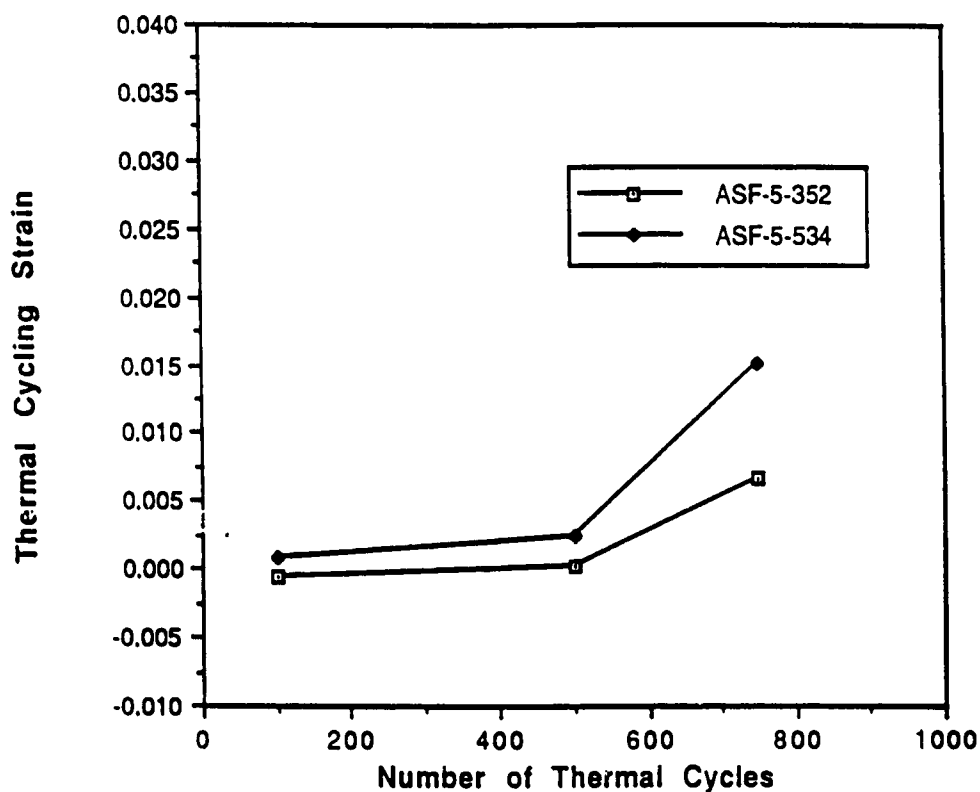


Figure 6.13 Thermal Cycling Strain versus Number of Thermal Cycles, W-FeCrAlY Experimental Result.

The ASF-5 data which will be compared to the predictions of the model is shown in Figure 6.13. This data was discussed in Chapter Four. The ASF-5 set was selected because SEM photography had shown little reinforcement-matrix interfacial damage after 500 cycles, and thus it provided a good approximation to the model assumption of perfect interfaces.

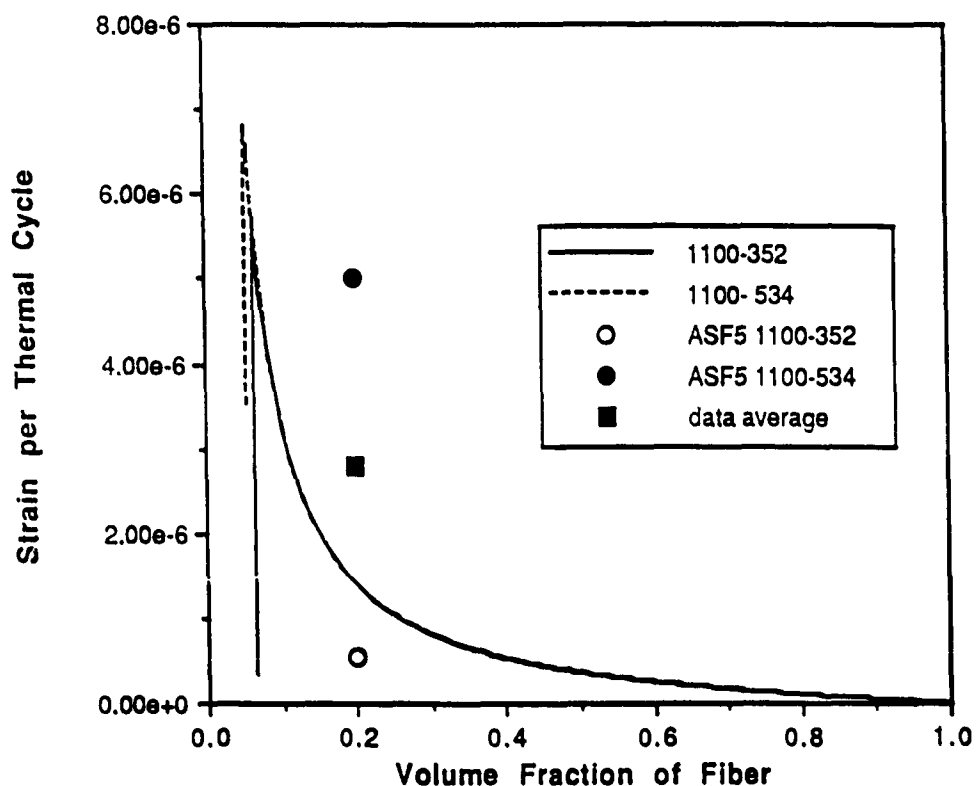


Figure 6.14 Comparison of Model Prediction with Experimental Result for Thermal Cycling Strain per Cycle versus Volume Fraction of Fiber, W-1%ThO₂ FeCrAlY.

In Figure 6.14 the strain per thermal cycle predictions of the model are compared to the two ASF-5, 500 cycle data points. The model predicted the same strain per thermal cycle in both the 1100-352 C and the 1100-534 C cases. Because the measured thermal cycling deformations were only on the order of 20 micron the micrometer measurement technique has significant scatter.

6.3.2 W Reinforced Cu

Table 6.5 Input Data for W-Cu

Cu

Young's Modulus	1.10 E 5 MPa
Poisson's Ratio	0.35
Coefficient of Thermal Expansion	20.0 E-6 /C°
Uniaxial Yield Stress	68.9 MPa
High Temperature Uniaxial Yield Stress	11.4 MPa
High Temperature Shear Modulus	2.91 E 4 MPa
Creep Constant	1.04 E 16
Power Law Exponent	4.8

W

Young's Modulus	3.58 E 5 MPa
Poisson's Ratio	0.285
Coefficient of Thermal Expansion	4.75 E -6 /C°
Aspect Ratio	3000
Volume Fraction of Fiber	0.50 and 0.10

Thermal Cycle

T _{max}	800 C
T _{min}	200 C
Del T	-600 C
High Temperature Hold Time	250 sec.

Another set of experimental data was available in the literature for tungsten reinforced copper composites (Yoda et al, 1978; Yoda et al, 1979). The test specimens were produced by first winding 100 micron diameter tungsten wire around a flat graphite sheet. The fibers were then liquid infiltrated by 99.99% pure copper at 1150 C in a mullite tube. The processing was completed by a directional solidification treatment necessary to eliminate matrix porosity. Specimens were fabricated by wheel-cutting and emery paper finishing. Finally the specimens were sealed in evacuated quartz tubes to protect them from oxidation.

The W-Cu specimens were placed in a shuttle mechanism which transported them in and out of a resistance furnace held at 800 C. The hold time in the high temperature furnace was 250 seconds. Periodically the specimens were removed and measured with a slide caliper and/or a micrometer.

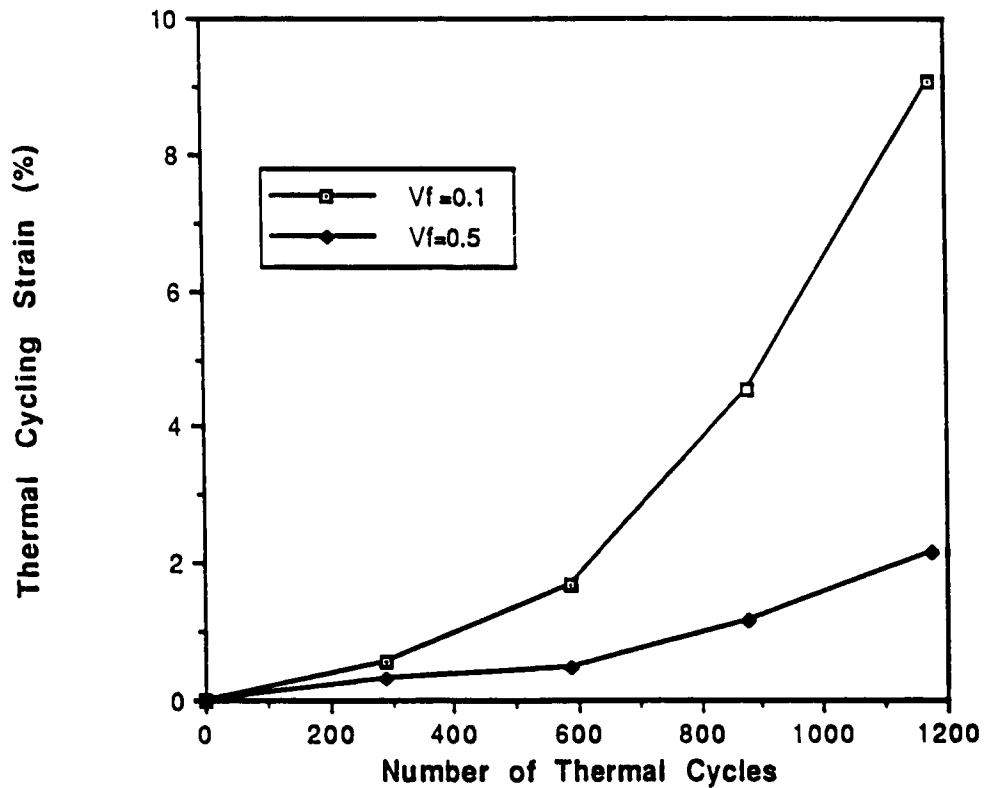


Figure 6.15 Thermal Cycling Strain versus Number of Thermal Cycles, W-Cu Experimental Result.

Yoda et al's experimental results are shown in Figure 6.15. The 0.1 volume fraction produced a larger strain per thermal cycle than did the 0.5 volume fraction.

Additionally the amount of strain per thermal cycle increased with increasing thermal cycling strain. In Yoda et al, 1979, the composite interfaces were shown to evolve a significantly defected form as the thermal cycling strain per thermal cycle increased. The form of this thermal cycling damage was very similar to that exhibited by the material of this study.

The model input parameters, Young's Modulus, Uniaxial Yield Strength, and High Temperature Uniaxial Yield Strength all were found in Carreker and Hibbard, 1953. This paper was referenced in Yoda et al, 1978, for matrix properties. The values for Poisson's Ratio, Creep Constant, and Power Law Exponent were found in Frost and Ashby, 1982. The Coefficient of Thermal Expansion was found in Touloukian et al, 1967. The properties of the tungsten reinforcement were the same as in the W-1%ThO₂ FeCrAlY case.

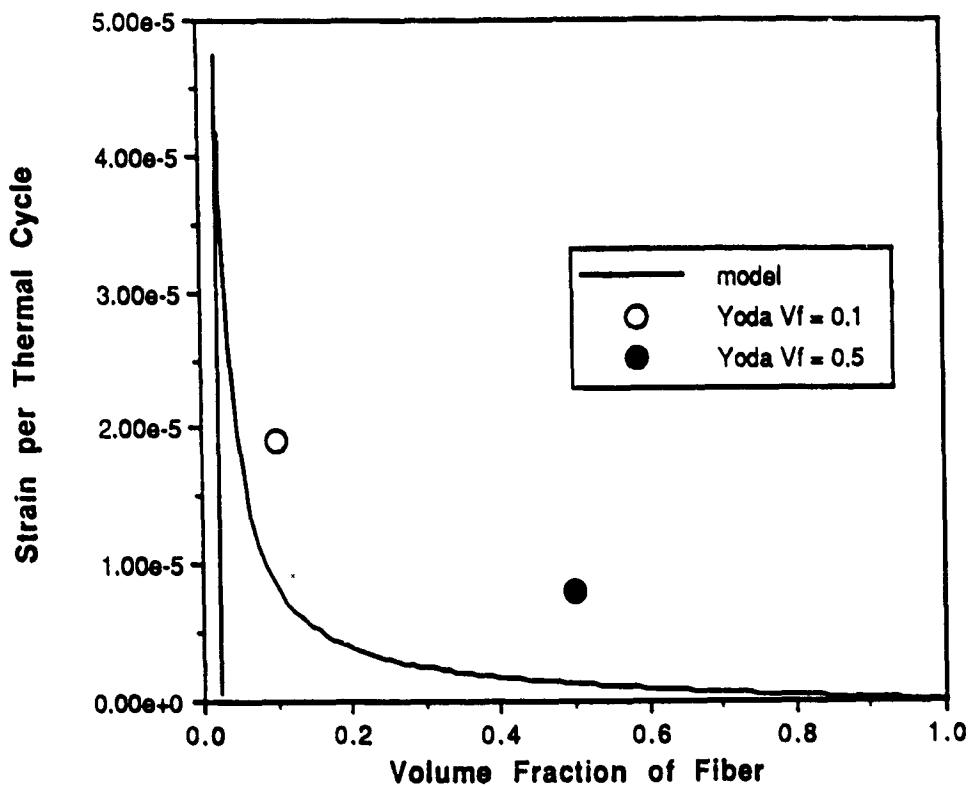


Figure 6.16 Comparison of Model Prediction with Experimental Result for Thermal Cycling Strain per Cycle versus Volume Fraction of Fiber, W-Cu.

Figure 6.16 shows that the experimental result is larger than the model prediction. This is likely due to the inherently weak bond between the copper matrix and tungsten fiber in this material. With a weak bond the composite matrix experiences less high temperature plastic strain than would be the case for a perfect reinforcement-matrix bond and therefore the rate of strain per thermal cycle is increased.

6.3.3 SiC Reinforced 2124-T6 Al

Table 6.6 Input Data for SiC-Al

2124 Al

Young's Modulus	0.676 E 5 MPa
Poisson's Ratio	0.33
Coefficient of Thermal Expansion	24.7 E-6 /C°
Uniaxial Yield Stress	50.8 MPa
High Temperature Uniaxial Yield Stress	34.5 MPa
High Temperature Shear Modulus	2.02 E 4 MPa
Creep Constant	3.41E 12
Power Law Exponent	5.08

SiC

Young's Modulus	4.27 E 5 MPa
Poisson's Ratio	0.17
Coefficient of Thermal Expansion	4.30 E -6 /C°
Aspect Ratio	4.0
Volume Fraction of Fiber	0.15

Thermal Cycle

T _{max}	400 C
T _{min}	20 C
Del T	-380 C
High Temperature Hold Time	125 sec.

The third set of experimental data was taken with a SiC whisker reinforced 2124-T6 Aluminum (Patterson and Taya, 1985; Taya and Mori, 1987). The composite material was processed by hot pressing a mixture of aluminum powder and SiC

whiskers. After pressing, the material was extruded, hot rolled, and finally heat treated. Rectangular thermal cycling samples were cut with the dimensions of 6.35 mm, 87 mm, and 40 mm. The samples were then thermal cycled between a hot fluidized bed set at either 400 C or 500 C and a water cooled air enclosure maintained at 10 C. The samples were transported between the two environments with a pneumatic cylinder which provided a hot zone hold time of 125 seconds. Tests were continued for 100 and 1000 cycles. After thermal cycling the dimensions of the samples were measured.

During material analysis it was discovered that the reinforcement had a 2-D planar misalignment normal to the pressing direction. Therefore the data useful for comparison with the thermal cycling model is the lateral deformation measured parallel to the pressing direction. The reference gave this measurement for two different maximum cycle temperatures: 500 C, and 400 C. These results are shown in Figure 6.17.

All of the model input data was available in Taya and Mori, 1987, except for the high temperature yield strength which was found in the Aerospace Structural Metals Handbook, 1989.

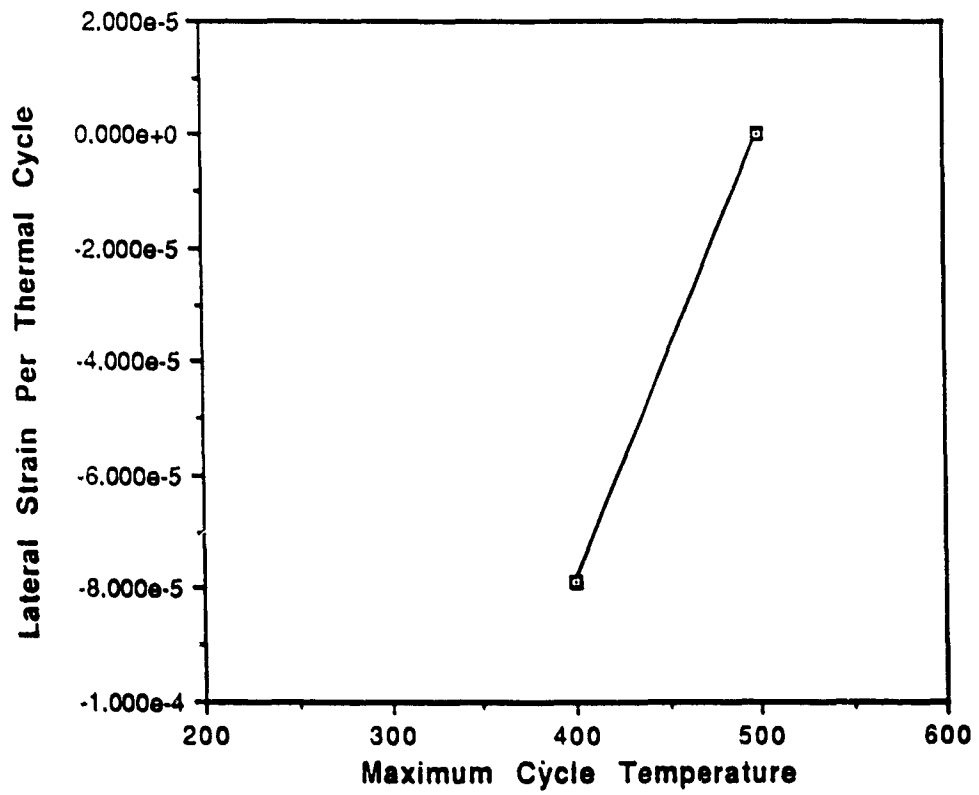


Figure 6.17 Maximum Thermal Cycle Temperature versus Lateral Strain, SiC-Al, Experimental Result.

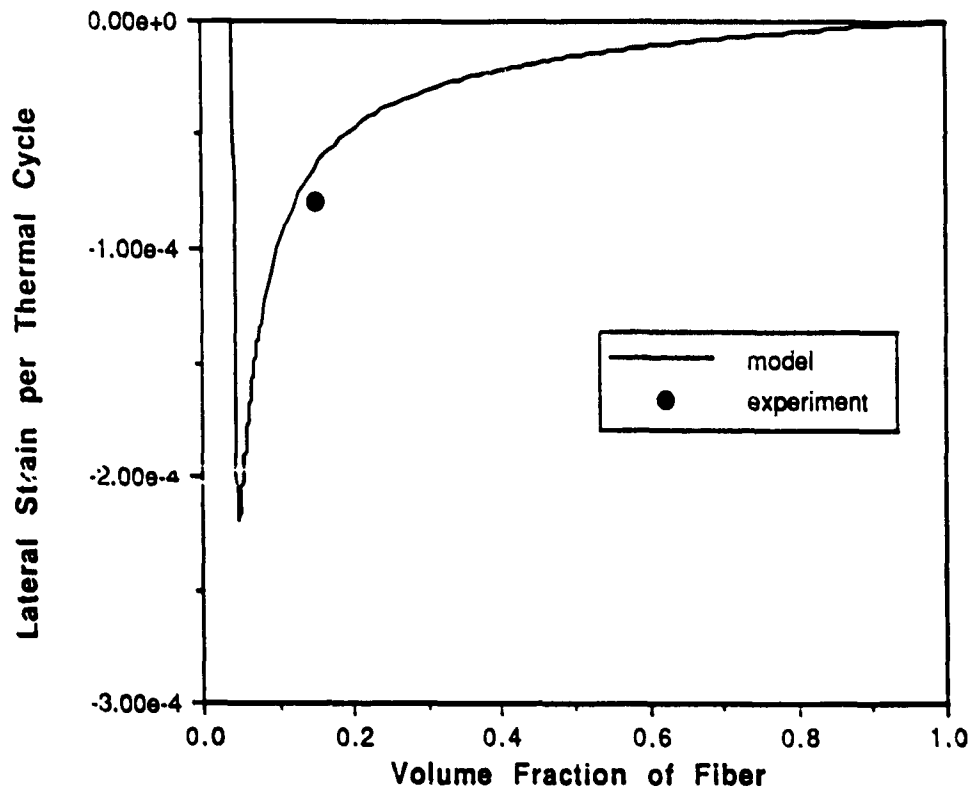


Figure 6.18 Comparison of Model Prediction with Experimental Result for Thermal Cycling Lateral Strain per Cycle versus Volume Fraction of Fiber, SiC-Al.

6.4 Analysis of the Case of Defected Interfaces

Previous researchers have shown that the matrix immediately adjacent to the fiber-matrix interface experiences a radial compressive stress during composite cool-down, and a radial tensile stress during composite heat-up (Takao and Taya, 1985). It therefore seems reasonable that the damage morphology presented in Chapter 5 would permit larger longitudinal shear load transfer between fiber and matrix during composite cool-down than during composite heat-up. Because of this, the composite would have a larger effective fiber volume fraction during cool-down than during heat-up within a particular thermal cycle. Furthermore, the quantitative results of Chapter 5 showed that large aspect ratio fibers first developed significant debonding near the fiber end, and with increasing thermal cycles the damage progressed towards the fiber longitudinal center. Therefore the composite would have a diminishing effective fiber volume fraction with increasing number of thermal cycles.

Figure 6.19 shows how the fiber-matrix interfacial damage is conjectured to evolve over a number of thermal cycles. In this figure, a reinforcing fiber has interfacial damage of effective length l_{n-1} during the heat-up portion of cycle $n-1$. During the cool-down portion of cycle n , this damage length is decreased to $l_{n-1} - dl_n$ by compressive radial interfacial stresses. Upon subsequent heat-up the damage grows to a new larger effective length l_n . During the next cool-down event during cycle $n+1$ compressive forces reduce the effective damage length by a slightly different amount dl_{n+1} . The development of an effective damage length, l , results in a decrease in effective fiber volume fraction, f_e . The development of a difference in effective fiber length between cool-down and heat-up, dl , results in a difference in effective fiber volume fraction between cool-down and heat-up, df .

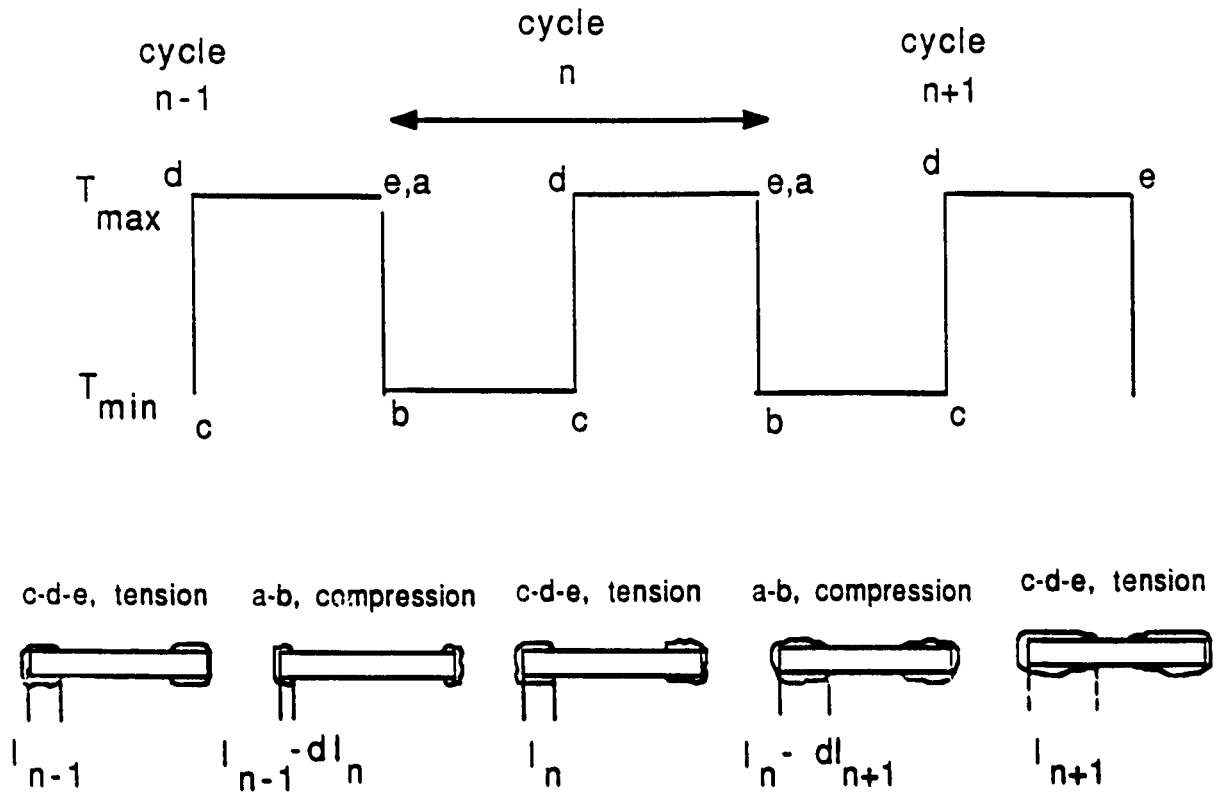


Figure 6.19 Progressively Damaged Fiber-Matrix Interface.

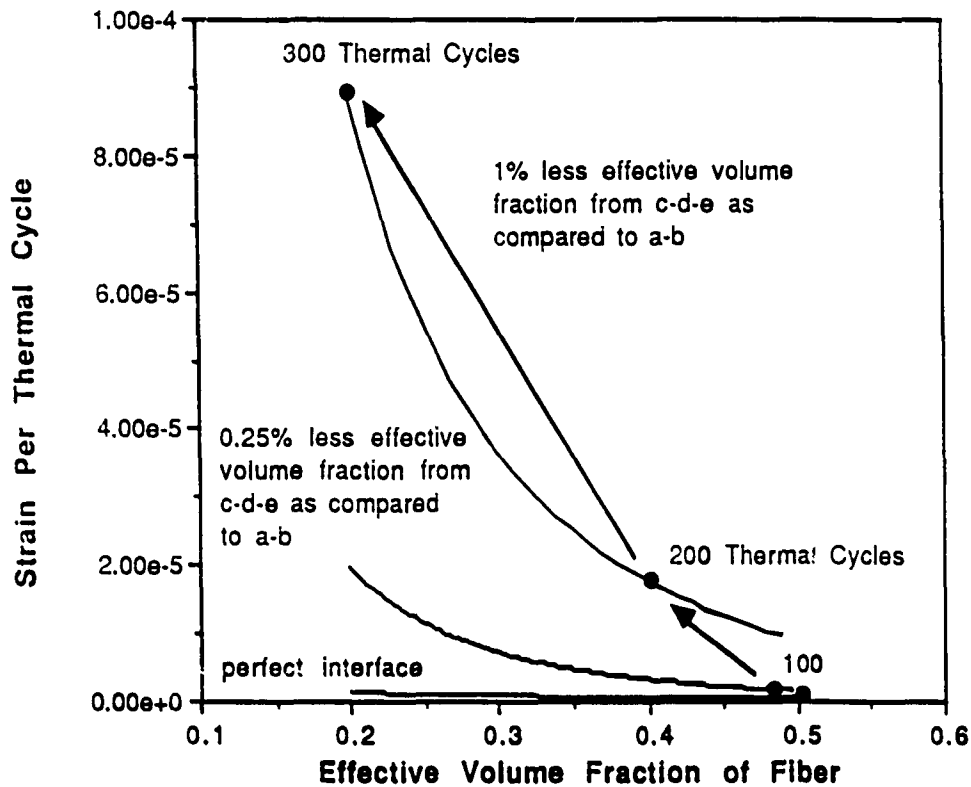


Figure 6.20 Hypothetical Damage Process.

Figure 6.20 shows results calculated for a 20 aspect ratio, W-FeCrAlY composite. The computation of strain per thermal cycle has been generalized to the case of defected interfaces by the substitution of

$$\text{Strain per Thermal Cycle} = (1.0 - f)(\epsilon_{p-df} + \epsilon_{hp_f} + \epsilon_{c_f}) \quad (6.4.1)$$

in place of Equation (6.1.26).

Superimposed on the calculated strain per thermal cycling results is a hypothetical f_e - df trajectory which is conjectured to duplicate the qualitative evolution of f_e and df in real composite materials. In this hypothetical example, the composite is fabricated with an initial fiber volume fraction of 0.50 and perfect interfaces. After 100 thermal cycles interfacial damage processes have reduced f_e to 0.48, and df has become

0.25%. After 200 thermal cycles the interfacial damage has increased until f_e has been reduced to 0.4, while df has increased to 1%. After 300 cycles the damage has increased much more so as to allow an effective fiber volume fraction of only 0.2 during heat-up, while df has remained at 1%. The results show that as the effective volume fraction becomes smaller, and df assumes a stable value of 1%, a far larger amount of thermal cycling strain occurs per thermal cycle than would be the case in a undefected composite.

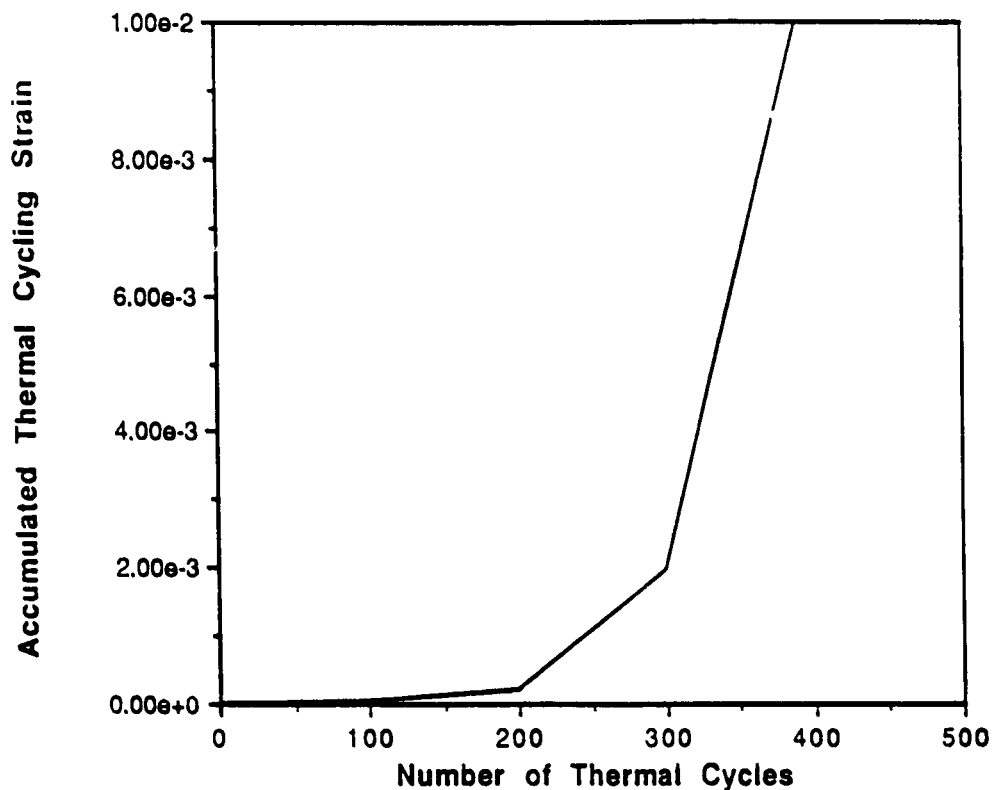


Figure 6.21 Integration of the Hypothetical Process in Figure 6.20.

The step-wise integration of the thermal cycling strain due to the hypothetical damage process of Figure 6.20 is shown Figure 6.21. For the first 100 cycles the composite has perfect interfaces and the strain per thermal cycle is very small, therefore little accumulated strain exists after 100 thermal cycles. After 200 thermal cycles the strain

per thermal cycle is larger and therefore the slope of the accumulated thermal cycling strain versus number of thermal cycles curve becomes larger. The composite is expected to continue to suffer increased strain per cycle until the interfacial damage saturates or else the composite is destroyed. The hypothetical process results shown in Figure 6.21 show qualitative agreement with experimental results for W-Cu and W-FeCrAlY composites shown in Figure 6.13 and Figure 6.15.

Chapter 7 Conclusions and Recommendations

7.1 Conclusions

Analysis and experimental results from this work can be used to justify a number of conclusions regarding damage accumulation processes in metal matrix composite materials subjected to repeated thermal cycles. While considering these conclusions it is important to discriminate between the concepts of interfacial plastic strain, and matrix average plastic strain. Interfacial plastic strain is the plastic flow of matrix material in a small region adjacent to a reinforcement interface. Repetitive exposures to interfacial plastic flow causes interfacial damage porosity. Matrix average plastic strain is an effective medium concept where the composite body as a whole experiences shape distortion. Matrix average plasticity can not occur with spherical reinforcements since the effects of the interfacial plastic strains are isotropic in the far field, however interfacial plastic flow will occur given sufficient temperature change.

The first conclusion to be made is the new analytical model presented in this work provides accurate quantitative predictions of composite thermal cycling strain in the special case of nondefected interfaces. This conclusion is supported by the good agreement between analytical prediction and experimental result for the W-FeCrAlY, W-Cu, and SiC-Al composite systems. The model prediction is based on the calculation of a low temperature average plastic strain, a high temperature average plastic strain, and a high temperature creep strain. The model results show that a minimum critical fiber volume fraction is required to initiate thermal cycling deformation, these results also show that a minimum critical fiber aspect ratio is required for the initiation of thermal cycling deformation.

The most important conclusion justified by this study is the thermal cycling strain per thermal cycle in a composite will increase strongly with increasing reinforcement-

matrix interfacial damage. This acceleration in composite deformation is particularly serious in low fiber volume fraction composites. This contention is well supported by scanning electron microscope imagery, quantitative damage porosity results, and experimental measurements of strain per thermal cycle in the W-FeCrAlY and W-Cu material systems. Since the model predictions of thermal cycling strain in the case of undefected interfaces are very small one must conclude that it is the acceleration of the thermal cycling strain per thermal cycle caused by accumulation of interfacial damage that causes the practical design concern.

Another conclusion warranted by the results of this study is the addition of 10 volume percent of ground Al_2O_3 fibers significantly delayed the interfacial damage development of a 0.2 fiber volume fraction, aspect ratio 20 W-FeCrAlY composite. This contention is well supported by the comparison of scanning electron microscope imagery, quantitative damage porosity results found with scanning technology, and experimental measurements of strain per thermal cycle between similar non-hybrid and hybrid material. This delay in interfacial damage development resulted in a decreased thermal cycling strain at high numbers of cycles in the Al_2O_3 -hybrid as compared to the non- Al_2O_3 -hybrid composite. The addition of Al_2O_3 is conjectured to reduce the effective matrix coefficient of thermal expansion, and expand the effective matrix yield surface. Both effects would reduce the severity of plastic strain near the reinforcement interfaces.

7.2 Recommendations

Having reached a number of conclusions during this work it is appropriate to recommend a processing scheme intended to optimize the thermal cycling dimensional stability of a high strength, creep resistant metal matrix composite. The selected composite configuration is a refinement of Professor Taya's original idea of a hybrid composite so as to exploit desirable predictions of the present model. The recommended configuration minimizes interfacial plastic strains so as to delay the initiation of interfacial damage, and at the same time increases the cool-down temperature change required to cause low temperature matrix plastic strain in the effective medium sense. Such a configuration is shown in Figure 7.1.

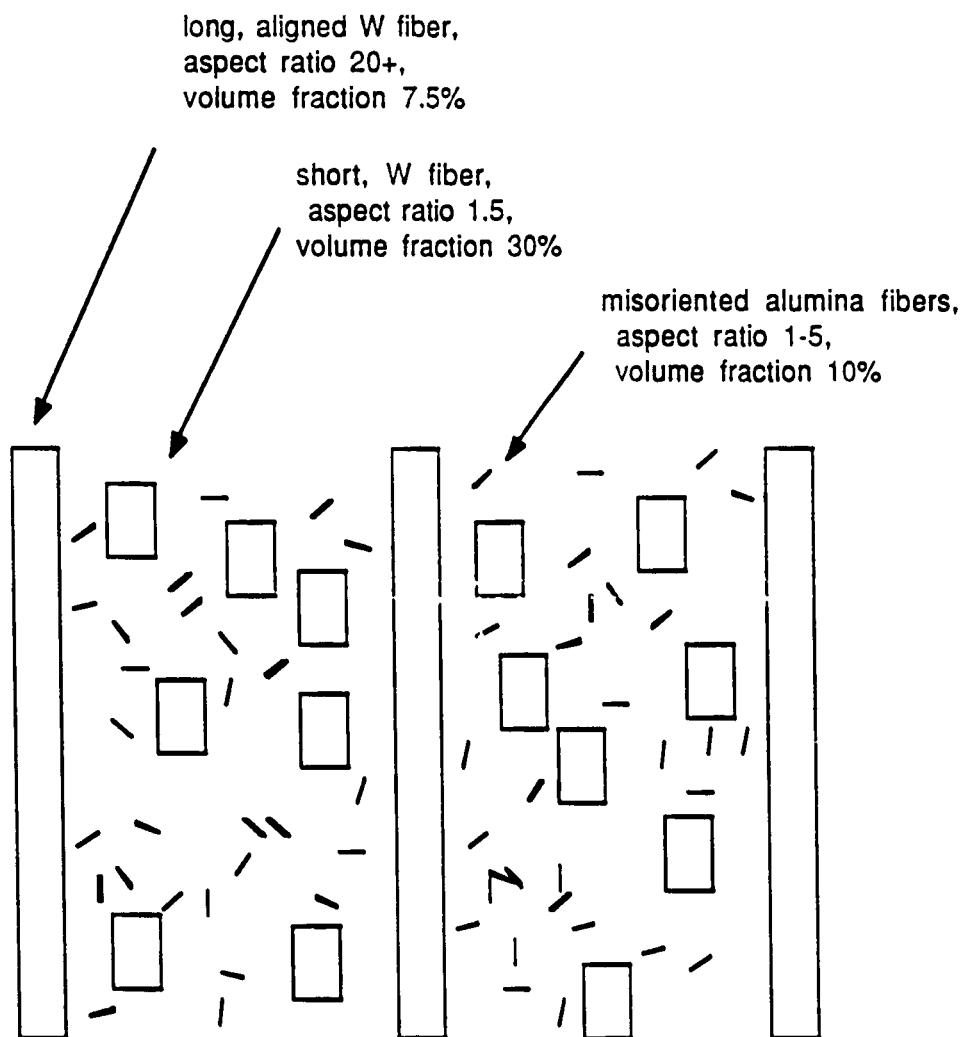


Figure 7.1 Recommended Thermal Cycling Resistant W-FeCrAlY Composite Mixed Scale Hybrid Reinforcement Configuration.

In this configuration the small diameter alumina reinforcement is included to reduce the effective matrix coefficient of expansion, and increase the effective matrix flow strength. The improvement of these properties would reduce the extent of plastic deformation near the interfaces of the small aspect ratio tungsten fibers. The short

tungsten fibers would in turn reduce the severity of plastic strains near the long tungsten fibers in a similar way. The recommended configuration would reduce average matrix plastic strains in the effective medium sense by having short fibers with an aspect ratio less than the critical aspect ratio, and long fibers with a fiber volume fraction less than the critical fiber volume fraction.

The present analysis is unable to precisely calculate the critical temperature change for the proposed composite since the hybrid matrix low temperature yield stress is unknown. However an approximate solution can be found if one assumes an effective matrix flow strength 25% larger than that of the monolithic matrix, and finds the coefficient of thermal expansion of the matrix by rule of mixtures. The properties used are given in Table 7.1.

Table 7.1 Input Data for Recommended W-FeCrAlY Mixed Scale Hybrid Composite

67Fe-24Cr-8Al-0.5Y-Al₂O₃ - short W-1%ThO₂ Hybrid Matrix

Young's Modulus	2.01 E 5 MPa
Poisson's Ratio	0.33
Coefficient of Thermal Expansion	17.45 E-6 /C°
Uniaxial Yield Stress	275 MPa

W-1%ThO₂

Young's Modulus	3.58 E 5 MPa
Poisson's Ratio	0.285
Coefficient of Thermal Expansion	4.75 E -6 /C°
Aspect Ratio	20
Volume Fraction of Long Fiber	0.075

Using the above properties the model predicts a temperature decrease of 1093 C is necessary for the initiation of low temperature average matrix plastic strain. This result contrasts sharply with the case of a 0.375 volume fraction, 20 aspect ratio non-hybrid W-FeCrAlY composite for which the analysis yielded a critical temperature change of 130 C.

Interfacial plastic strain will certainly occur if the recommended composite is thermal cycled between 1100 and 20 C, and because of this interfacial defect structures will very likely develop. These interfacial defect structures can be expected to reduce the composite strength and creep resistance. However, the development of defect structures is not predicted to lead to a dramatic increase in directional composite deformation since the matrix cool-down strain will remain elastic in the effective medium sense. The composite can therefore be expected to exhibit a small nearly isotropic swelling with increasing number of thermal cycles.

References

Armstrong, W., and Taya, M., 1987, "An Investigation of the Thermal Cycling Damage of 25vol.% SiCw/Alumina Ceramic Matrix Composite," *Proceedings of the 4th US-Japan Conference on Composite Materials (USJCCM4)*, Technomic Publications, pp. 765,772.

Armstrong, W., and Taya, M., 1990, "Design of a New Creep-Thermal Cycler for High Temperature Metal Matrix Composites," *Experimental Techniques*, to be published.

Armstrong, W., and Taya, M., 1991, "Damage Accumulation Mechanisms in Advanced Metal Matrix Composites Subjected to Thermal Cycling," to be published.

Arsenault, R. J., and Taya, M., 1987, "Thermal Residual Stress in Metal Matrix Composite," *Acta Metall.*, Vol. 35, No. 3, pp. 651-659

Arsenault, R. J., 1987, "Strengthening Mechanisms in Discontinuous SiC / Al Composites," *Composite Structures 4*, Vol. 2, Damage Assessment and Material Evaluation, Edited by I. H. Marshall, Elsevier Applied Science, pp. 2.70-2.80.

Ayer, R., Scanlon, J. C., Ramanarayanan, T. A., Mueller, R. R., and Petkovic-Luton, R., 1987, "Crystal Structure of Intermetallic Phase in Fe-20Cr-4Al-0.5Y Alloy by Convergent Beam Diffraction," *J.Mater.Res*, 2(1), pp. 16-27

Bahei-El-Din, Y. A., Dvorak, G. J., and Wu, J., 1989, "Fracture of Fibrous Metal Matrix Composites-II. Modeling and Numerical Analysis," *Engineering Fracture Mechanics*, Vol. 34, No. 1, pp. 105-123.

- Blann, G. A., Dias, D. J., and Nelson, J. A., 1989, "Raising the Standards for Coating Analysis," *Advanced Materials and Processes*, Dec., pp. 31-36.
- Brentnall, W. D., 1976, "Metal Matrix Composites for High Temperature Turbine Blades," Final Report, AD A030074, 39 pages.
- Brentnall, W. D., et al, 1974, "Metal Matrix Composites for High Temperature Turbine Blades," AD-782 398, 52 pages.
- Brentnall, W. D., et al, 1975, "Metal Matrix Composites for High Temperature Turbine Blades," AD A009 298, 39 pages.
- Brentnall, W. D., et al, 1977, "FRS Composites for Advanced Gas Turbine Engine Components," Final Report, NADC 76077-30, 39 pages.
- Carreker, R. P., Jr., and Hibbard, W. R., Jr., 1953, "Tensile Deformation of High-Purity Copper as a Function of Temperature, Strain Rate, and Grain Size," *Acta Metallurgica*, Vol. 1, Nov., pp. 654-663.
- Caulfield, T., and Tien, J. K., 1989, "High Temperature Reaction Zone Growth in Tungsten Fiber Reinforced Superalloy Composites: Part 1. Application of the Moving Boundary Equations," *Metallurgical Transactions A*, Vol. 20A, Feb., pp. 255-265.
- Chaboche, J. L., 1989, "Phenomenological Aspects of Continuum Damage Mechanics," *Theoretical and Applied Mechanics*, P. Germain, M. Piau, and D. Caillerie Editors, Elsevier Science Publishers, pp. 41-56.
- Christensen, R. M., 1979, "Solutions for Effective Shear Properties in Three Phase Sphere and Cylinder Models," *J. Mech. Phys. Solids*, Vol. 27, pp. 315-330.
- Christensen, R. M., 1990, "A Critical Evaluation for a Class of Micro-Mechanics Models," *J. Mech. Phys. Solids*, Vol. 38, No. 3, pp. 379-404.

- Chubb, W., Alfant, S., Bauer, A. A., Jablonowski, E. J., Shober, F. R., and Dickerson, R. F., 1958, "Constitution, Metallurgy, and Oxidation Resistance of Iron-Chromium-Aluminum Alloys," BMI-1298, Battelle Memorial Institute, 104 pages.
- Cox, H. L., 1952, "The Elasticity and Strength of Paper and Other Fibrous Materials," *Brit. Jour. Appl. Phys.*, Vol. 3, pp. 73-79.
- Davidson, D. L., 1987, "Micromechanisms of Fatigue Crack Growth and Fracture Toughness in Metal Matrix Composites," AD-A185 200, 26 pages.
- De Silva, A. R. T., 1968, "A Theoretical Analysis of Creep in Fibre Reinforced Composites," *J. Mech. Phys. Solids*, Vol. 16, pp. 169-186
- DiCarlo, J. A., 1985, "Fibers for Structurally Reliable Metal and Ceramic Composites," *Journal of Metals*, June, pp. 44-49.
- Donachie, M., 1988, "Relationships of Properties and Processes," *Titanium, A Technical Guide*, M. J. Donachie, Jr. Editor, ASM International, pp. 157-206.
- Dvorak, G. J., Bahei-El-Din, Y. A., and Bank, L. C., 1989, "Fracture of Fibrous Metal Matrix Composites-I. Experimental Results," *Engineering Fracture Mechanics*, Vol. 34, No. 1, pp. 87-104.
- Eaton, H., and Norden, H., 1985, "Chemical and Microstructural Changes at High Temperature in Tungsten Wire Reinforced Metal-Matrix Composite Materials," *Failure Mechanisms in High Performance Materials*, Cambridge University Press, pp. 109-116.
- Echigoya, Armstrong, W. D., and Taya, M., 1990, "The Degradation Mode of High Temperature Metal Matrix Composites by Thermal Cycling," *MSE-A Journal*, to be published.

- Eshelby, J. D., 1957, "The Determination of the Elastic Field of an Ellipsoidal Inclusion, and Related Problems," *Proceedings of the Royal Society of London, Series A*, Vol. 241, pp. 376-396
- Evans, A. G., and Cannon, R. M., 1989, "Stresses in Oxide Films and Relationships with Cracking and Spalling," *Materials Science Forum*, Vol. 43, pp. 243-268.
- Garmong, G., 1974, "Elastic-Plastic Analysis of Deformation Induced by Thermal Stress in Eutectic Composites: I Theory," *Metallurgical Transactions*, Vol. 5, Oct., pp. 2183-2190.
- Garmong, G., 1974, "Elastic-Plastic Analysis of Deformation Induced by Thermal Stress in Eutectic Composites: II Thermal Expansion," *Metallurgical Transactions*, Vol. 5, Oct., pp. 2191-2197.
- Garmong, G., 1974, "Elastic-Plastic Analysis of Deformation Induced by Thermal Stress in Eutectic Composites: III Thermal-Cycling Damage," *Metallurgical Transactions*, Vol. 5, Oct., pp. 2199-2205.
- Garmong, G., 1975, "Author's Reply," *Metallurgical Transactions*, Vol. 6a, August, pp. 1676-1677.
- Golightly, F. A., Stott, F. H., and Wood, G. C., 1976, "The Influence of Yttrium Additions on the Oxide-Scale Adhesion to an Iron-Chromium-Aluminum Alloy," *Oxidation of Metals*, Vol. 10, No. 3, pp. 163-187
- Golightly, F., Stott, F., and Wood, G., 1979, "The Tensile Straining of Oxidized Fe-Cr-Al-Y alloys," *Werkstoffe und Korrosion*, Vol. 30, pp. 487-491. Warren, R., and Andersson, C., 1982, Short-Term Tensile Strength and Creep Behavior of

- Harris, B., and Ellison, E. G., 1966, "Creep and Tensile Properties of Heavily Drawn Tungsten Wire," *Transactions of the ASM*, Vol. 59, pp.744-754.
- Hartman, G. A., III, 1985, "A Thermal Control System for Thermal Cycling," *Journal of Testing and Evaluation*, JTEVA, Vol. 13, No. 5, Sept., pp. 363-366.
- Hashish, M., 1988, "Visualization of the Abrasive-Waterjet Cutting Process," *Experimental Mechanics*, June, pp. 159-169.
- Helmink, R. C., and Piwonka, T. S., 1979, "Cast Fiber-Reinforced Superalloys," *Advanced Fibers and Composites for Elevated Temperatures*, I. Ahmad and B. R. Noton Editors, The Metallurgical Society of AIME, pp. 205-223.
- Jackson, M. R., and Mehan, R. L., 1987, "LPPD Iron Base Metal Matrix Composites," *Sixth International Conference on Composite Materials, ICCM & ECCM*, Vol. 2, F. L. Matthews, N. C. R. Buskell, J. M. Hodgkinson, and J. Morton Editors, Elsevier Applied Science, pp. 2.431-2.440
- Jacobson, B. E., 1980, "Methods for Characterization of Coating Microstructures," *Thin Solid Films*, 73, pp. 341-345.
- Johnson W. S., 1988, "Fatigue Testing and Damage Development in Continuous Fiber Reinforced Metal Matrix Composites," *NASA Technical Memorandum 100628*, 55 pages.
- Johnson, W. S., 1982, "Mechanisms of Fatigue Damage in Boron / Aluminum Composites," *Damage in Composite Materials*, ASTM STP 775, K. L. Reifsnider Editor, pp. 83-102
- Johnson, W. S., 1987, "Fatigue Damage Accumulation in Various Metal Matrix Composites," *NASA Technical Memorandum 89116*, 67 pages.

- Kelly, A., and Street, K. N., 1972, "Creep of Discontinuous Fiber Composites II. Theory for the Steady-State," *Proceedings of the Royal Society of London, Series A*, Vol. 328, pp. 283-293.
- Krajcinovic, D., and Ilankkamban, R., 1985, "Mechanics of Solids with Defective Microstructure," *J. Struct. Mech.*, 13(3&4), pp. 267-282.
- Kyono, T., Kuroda, E., Kitamura, A., Mori, T., and Taya, M., 1988, "Effects of Thermal Cycling on Properties of Carbon Fiber / Aluminum Composites," *Transactions of the ASME, Journal of Engineering Materials and Technology*, Vol. 110, April, pp. 89-95.
- Larsson, L. O. K., and Warren, R., 1979, "Tungsten Wire Reinforced Metals for High Temperature Application," *Advanced Fibers and Composites for Elevated Temperatures*, I. Ahmad and B. R. Noton Editors, The Metallurgical Society of AIME, pp. 108-125.
- Lawson, L. R., 1987, "Thermal Cycling Apparatus for Thermomechanical Fatigue Testing", *Rev. Sci. Instrum.*, 58 (10), pp. 1942-1944.
- LeFlour, J. C., and Locicero, R., 1987, "Influence of Internal Stresses Induced by Thermal Cycling on the Plastic Deformation Resistance of an Al / SiC Composite Material," *Scripta Metallurgica*, Vol. 21, 1071-1076.
- Lemaitre, J., and Dufailly, J., 1987, "Damage Measurements," *Engineering Fracture Mechanics*, Vol. 28, No. 5/6, pp. 643-661
- Lindblom, Y., 1978, "Creep and Structural Stability of High Temperature Materials," *High Temperature Alloys for Gas Turbines*, D. Coutsouradis, P. Felix, H. Fischmeister, L. Habraken, Y. Lindblom, and M. O. Speidel Editors, Applied Science Publishers LTD, pp. 285-316

- Lulay, K., 1990, "The Effects of Cooling on the Flow Strength of Metal Matrix Composites," University of Washington Doctoral Dissertation
- Luthra, K. L., and Briant, C. L., 1989, "The Role of Surface Segregation and Stresses in Scale Adherence," *Materials Science Forum*, Vol. 43, pp. 299-326.
- Mckimpson, M. G., and Scott, T. E., 1989, "Processing and Properties of Metal Matrix Composites Containing Discontinuous Reinforcement," *Materials Science and Engineering*, A107, pp.93-106.
- McLean, D., 1972, "Viscous Flow of Aligned Composites," *Journal of Materials Science*, Vol. 7, pp. 98-104.
- Mileiko, S. T., 1970, "Steady State Creep of a Composite Material with Short Fibres," *Journal of Materials Science*, Vol. 5, pp. 254-261.
- Morimoto, T., and Taya, M., 1988, "Thermal Cycling Damage of High Temperature Metal Matrix Composites," *Proceedings International Conference Fractures*, K. Salama et al Editors, Pergamon Press
- Morimoto, T., Yamaoka, T., Lilholt, H., and Taya, M., 1988, "Second Stage Creep of SiC Whisker / 6061 Aluminum Composite at 573K," *Transactions of the ASME, Journal of Engineering Materials and Technology*, April, Vol. 110, pp. 70-76.
- Mortensen, A., Gungor, M. N., Cornie, J. A., and Flemings, M. C., 1986, "Alloy Microstructures in Cast Metal Matrix Composites," *J. Met. March*, pp. 30-35.
- Mullendore, J. A., 1984, "Tungsten: Its Manufacture, Properties, and Application," *Refractory Metals and Their Industrial Applications*, ASTM STP 849, R.E. Smallwood Editor, pp. 82-105.

- Patterson, W.G., and Taya, M., "Thermal Cycling Damage of SiC Whisker/2124 Aluminum," *Proc. ICCM-V*, TMS-AIME, W. C. Harrigan Jr., J. Strife, and A. K. Dhingra Editors, pp. 53-66.
- Pernot, J. J., and Mall, S., 1989, "A Thermal-Mechanical Fatigue Crack-Growth Testing System," *Experimental Techniques*, Feb., pp. 24-28.
- Petrasek, D. W., 1972, "High-Temperature Strength of Refractory-Metal Wires and Consideration for Composite Applications," NASA Technical Note D-6881, 40 pages.
- Petrasek, D. W., and Signorelli, R. A., 1981, "Tungsten Fiber Reinforced Superalloys - A Status Review," NASA Technical Memorandum 82590, 68 pages.
- Petrasek, D. W., and Signorelli, R. A., 1987, "Fiber Reinforced Superalloys," NASA Technical Memorandum 89865, 61 pages.
- Petrasek, D. W., and Signorelli, R. A., Caulfield, T., and Tein, J. K., "Fiber Reinforced Superalloys," *Superalloys, Supercomposites and Superceramics*, J. K. Tein, and T. Caulfield Editors, Academic Press, pp. 625-671
- Rack, H. J., and Ratnaparkhi, P., 1988, "Damage Tolerance in Discontinuously Reinforced Metal Matrix Composites," *Journal of Metals*, Nov., pp. 55-57.
- Raghaven, A., Scalon, J. C., Ramanarayanan, T. A., Mueller, R. R., and Petkovic-Luton, R., 1987, "Crystal Structure of Intermetallic Phase in Fe-20Cr-4Al-0.5Y Alloy by Convergent Beam Electron Diffraction," *J. Mater. Res.*, Vol. 2, No. 1, pp. 16-27
- Rairden, J. R., and Habesch, E. M., 1981, "Low-Pressure-Plasma-Deposited Coatings Formed From Mechanically Alloyed Powders," *Thin Solid Films*, 83, pp. 353-360.

- Ramanarayanan T. A., Ayer R., Petkovic-Luton R., Leta D. P., 1988, "Investigation of Mechanisms of Yttrium-Induced Effects on Growth Rate and Adherence of Protective Oxide Scales at High Temperatures," *High Temperatures-High Pressures*, Vol. 20, No. 3, pp. 277-292.
- Reifsnider, K. L., 1988, "Damage-Tolerant Polymer Composite Systems," *Journal of Metals*, Nov., pp. 51-54.
- Roberts, A. C., Harries, D. R., Arkell, D. R., Dewey, M.A.P., and Hughes, J. D. H., 1969, "Effects of Yttrium on the Structure and Post-Irradiation Tensile Properties of an Iron-Chromium-Aluminum Alloy," *Irradiation Effects in Structural Alloys for Thermal and Fast Reactors*, ASTM STP 457, pp. 312-328
- Rozner, A. G., and Wiley, R. C., 1979, "Processing of Tungsten Wire Reinforced FeCrAlY Alloy Composite," *Advanced Fibers and Composites for Elevated Temperatures*, Edited by I. Ahmad, and B. R. Noton, The Metallurgical Society of AIME, pp. 175-182.
- Saff, C. R., Harmon, D. M., and Johnson, W. S., 1988, "Damage Initiation and Growth in Fiber-Reinforced MMCs," *Journal of Metals*, Nov., pp. 58-63.
- Saller, H. A., Stacey, J. T., and Eddy, N.S., 1954, "Investigation of Wrought Iron-Chromium-Aluminum Alloys for Service at 2200 F," *Battelle Memorial Institute*, BMI-922, 45 pages
- Schoutens, J. E., 1987, "Considerations for Designing with Metal Matrix Composite Materials," *Composite Structures 4*, Vol. 2, Damage Assessment and Material Evaluation, Edited by I. H. Marshall, Elsevier Applied Science, pp. 2.82-2.97.
- Sehitoglu, H., 1985, "Constraint Effect in Thermo-Mechanical Fatigue," *Transactions of the ASME, Journal of Engineering Materials and Technology*, Vol. 107, July, pp. 221-226

- Snow, D. B., and Dunham, T. E., 1974, "Control of Grain Structure for Lamp Filament Applications," *Grain Boundaries in Engineering Materials*, J. L. Walter, J.H. Westbrook, D.A. Woodford Editors, pp. 77-88
- Stecura, S., 1986, "Advanced Thermal Barrier System Bond Coatings for Use on Nickel-, Cobalt-, and Iron-Base Alloy Substrates," *Thin Solid Films*, Vol. 136, pp. 241-256
- Stott, F. H., Golightly, F. A., and Wood, G. C., 1979, "The Influence of Thermal Cycling on the Oxidation Behavior of Fe-Cr-Al and Fe-Cr-Al-Y Alloys at 1200 C," *Corrosion Science*, Vol. 19, pp.889 to 906
- Takao, Y., Chcu, T. W., and Taya, M., 1982, "Effective Longitudinal Young's Modulus of Misoriented Short Fiber Composites," *Trans. of ASME Journal of Applied Mechanics*, Sept., Vol 49, pp. 536-540
- Takao, Y., and Taya, M., 1985, "Thermal Expansion Coefficients and Thermal Stresses in an Aligned Short Fiber Composite with Application to a Short Carbon Fiber / Aluminum," *Transactions of the ASME, Journal of Applied Mechanics*, Dec., Vol. 52., pp. 806-810.
- Talreja, R., 1989, "Damage Development in Composites: Mechanisms and Modeling," *Journal of Strain Analysis*, Vol. 24, No. 4, pp. 215-222.
- Taya, M., 1986, "Modeling of the Second and Third Stage Creep Rates of an Aligned Short Fiber Metal Matrix Composite," *Advances in Composite Materials and Structures*, ASME WAM Bound Volume, S. S. Wang and Y. Rajapakse Editors.
- Taya, M., 1989, "*Metal Matrix Composites: Thermomechanical Behavior*," Pergamon Press, 264 pages.

- Taya, M., and Mori, T., 1987, "Modeling of Dimensional Change in Metal Matrix Composite Subjected to Thermal Cycling," *Thermomechanical Couplings in Solids*, H.D. Bui and Q. S. Nguyen (Editors), Elsevier Science Publishers B. V. (North-Holland) IUTAM, pp. 147-162.
- Tien, J., Caulfield, T., and Wu, Y., 1989, "High Temperature Reaction Zone Growth in Tungsten Fiber Reinforced Superalloy Composites: Part II. Matrix Chemistry Effects," *Metallurgical Transactions A*, Vol. 20A, Feb., pp. 267-272.
- Tjong, S., Hsieh, I., and Ho, N., 1988, "Dislocation Structures in a Cyclically Deformed Fe-25 Cr-2 Al Alloy," *Z. Metallkunde*, Bd. 79, H. 3, pp. 189-193.
- Touloukian, Y. S., Editor, 1967, "Thermophysical Properties of High Temperature Solid Materials," Macmillan.
- Tyson, W. R., 1975, "Discussion of "Elastic-Plastic Analysis of Deformation Induced by Thermal Stress in Eutectic Composites," *Metallurgical Transactions A*, Vol. 6A, pp. 1674-1676.
- Warren, R., and Anderson, C., 1982, "Short-Term Tensile Strength and Creep Behavior of Tungsten Wires Up to 1100 C," *High Temperatures High Pressures*, Vol. 14, pp. 41-51.
- Warren, R., Larsson, L. O. K., Ekstrom, P., and Jansson, T., 1982, "Thermal Cycling of W-Wire Reinforced Metal Matrix Composites," *Progress in Science and Engineering of Composites*, ICCM-IV, T. Hayashi, K. Kawata, and S. Umekawa Editors
- Westfall, L. J., and Petrusek, D. W., 1988, "Thermal-Mechanical Fatigue Test Apparatus For Metal Matrix Composites and Joint Attachments," *Testing Technology of Metal Matrix Composites*, ASTM STP 964, P. R. DiGiovanni and N. R. Adsit Editors, pp. 1-17.

- Westfall, L. J., 1985, "Composite Monolayer Fabrication By an Arc-Spray Process," NASA-TM-86917, 9 pages.
- Wetherhold, R. C., and Westfall, L. J., 1987, "Deformation of Surface Cladding and Matrix of Tungsten-Fiber-Reinforced Superalloy Under Thermomechanical Loading," *Materials Science and Engineering*, Vol. 85, pp. L13-L17.
- Wetherhold, R. C., and Westfall, L. J., 1988, "Thermal Cycling of Tungsten-Fibre-Reinforced Superalloy Composites," *J. Mater. Sci.*, Vol. 23 (2), pp. 713-717.
- White, M. K., and Wright, M. A., 1976, "Investigations Into the Mechanisms of Thermal Cycling Damage in Metal Matrix Composites," N00014-75-C-0352, 84 pages.
- Wilson, F., Knott, B., and Desforges, C., 1978, Preparation and Properties of Some ODS Fe-Cr-Al Alloys," *Metallurgical Transactions A*, Vol. 9A, Feb., pp. 275-282.
- Winsa, E. A., 1982, "Tungsten Fiber Reinforced Superalloy Composite High Temperature Design Considerations," NASA Technical Memorandum 82811, 12 pages.
- Wolff, E.G., Min, B. K., and Kural, M. H., 1985, "Thermal Cycling of a Unidirectional Graphite-Magnesium Composite," *Jour. of Mater. Sci.*, Vol. 20, pp. 1141-1149.
- Write, M. A., 1973, "The Mechanical Properties of Metal Matrix Composites Subjected to Cyclic Temperature Changes," AD774890, 98 pages.
- Wukusick, C. S., and Collins, J. F., 1964, "An Iron-Chromium-Aluminum Alloy Conaining Yttrium," *Materials Research and Standards*, Vol. 4, No. 12, pp. 637-646.

Yoda, S., Kurihara, N., Wakashima, K., and Umekawa, S., 1978, "Thermal Cycling-Induced Deformation of Fibrous Composites with Particular Reference to the Tungsten-copper System," *Met. Trans. A*, Vol. 9A, pp. 1229-1236.

Yoda, S., Takahashi, R., Wakashima, K., and Umekawa, S., 1979, "Fiber/Matrix Interface Porosity Formation in Tungsten Fiber/Copper Composites on Thermal Cycling," *Met. Trans. A*, Vol. 10A, pp. 1796-1798.

Yoshitake, M., 1985, "Production of Metal Powders and Their Application in Composite Materials: Part 1," *Metal Powder Report*, June, pp. 323-327.

Appendix A Cox Shear Lag Model

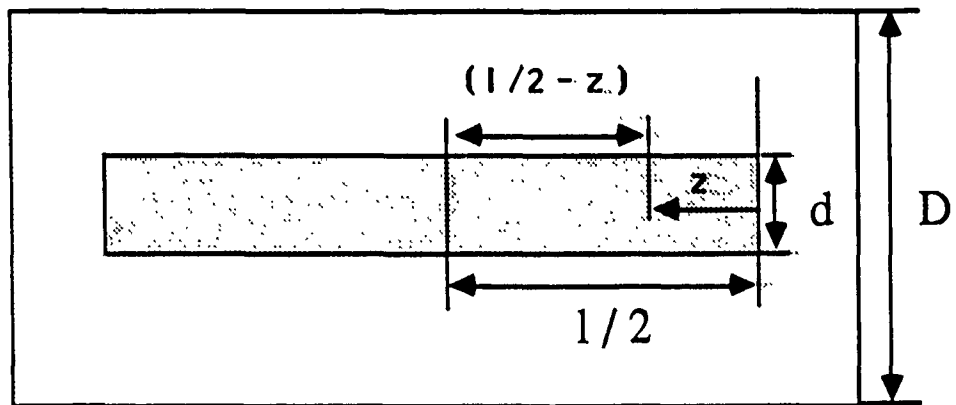


Figure A1. Cox Shear Lag Model Parameters

The Shear Lag Model assumes that the bond between the fiber and matrix is perfect, and that forces are not transmitted through the fiber ends. The solid domain is subjected to a far field uniform strain e . Consider a material point at a location z along the fiber longitudinal axis as shown in Figure A1.. The displacement of this point will be v if no fiber is present. The z derivative of the v displacement function is e , the uniform far field applied strain. If a fiber is included in this domain the composite displacement function is altered by the significantly stiffer fiber. The displacement function with the fiber present is labeled u . The difference between u and v is proportional to t_0 , the matrix fiber interface shear stress. Finding a differential change in fiber axial stress as

$$d\sigma_f = \frac{\pi d \tau_0 dz}{\frac{\pi d^2}{4}} = \frac{4 \tau_0 dz}{d} \quad (\text{A1})$$

from which the z derivative of the fiber axial stress can be given as

$$\frac{d\sigma_f}{dz} = \frac{4 \tau_0}{d} = h(u - v) \quad (\text{A2})$$

$$\frac{du}{dz} = \frac{\sigma_f}{E_f} \quad (\text{A3})$$

and the applied composite strain e is given by

$$e = \frac{dv}{dz} \quad (\text{A4})$$

Differentiating equation (A2), and using (A3) and (A4) yields

$$\frac{d^2 \sigma_f}{dz^2} = \frac{d}{dz} h(u - v) = h \left(\frac{\sigma_f}{E_f} - e \right) \quad (\text{A5})$$

Equation (A5) is a nonhomogeneous ordinary differential equation which has the solution form of

$$\sigma_f = E_f e + C_1 \cosh \left(\sqrt{\frac{h}{E_f}} \left(\frac{1}{2} - z \right) \right) + C_2 \sinh \left(\sqrt{\frac{h}{E_f}} \left(\frac{1}{2} - z \right) \right) \quad (\text{A6})$$

Applying the boundary condition of σ_f is equal to 0 at $(1/2 - z)$ equal to $1/2$ gives

$$0 = E_f + C_1 \cosh \left(\sqrt{\frac{h}{E_f}} \frac{1}{2} \right) + C_2 \sinh \left(\sqrt{\frac{h}{E_f}} \frac{1}{2} \right) \quad (\text{A7})$$

Differentiating (A6) with respect to z and setting equal to zero at the fiber center, we find that C_2 is equal to zero. Using this result and solving for C_1 in equation (A7) one finds

$$\sigma_f = E_f e \left\{ 1 - \frac{\cosh \left(\sqrt{\frac{h}{E_f}} \left(\frac{1}{2} - z \right) \right)}{\cosh \left(\sqrt{\frac{h}{E_f}} \frac{1}{2} \right)} \right\} \quad (\text{A8})$$

The interfacial shear stress can now be found from (A2) as $d/4$ times the z derivative of σ_f .

$$\tau = -\frac{d E_f}{4} e^{\sqrt{\frac{h}{E_f}}} \frac{\sinh\left(\sqrt{\frac{h}{E_f}} \left(\frac{1}{2} - z\right)\right)}{\cosh\left(\sqrt{\frac{h}{E_f}} \frac{1}{2}\right)} \quad (\text{A9})$$

By similar triangles one can find the shear displacement g_r as a function of r as

$$\gamma_r = \frac{\tau_o d}{2 r G_m} \quad (\text{A10})$$

The difference between u and v can be found by integrating (A10) between the interface and the shear cell boundary

$$\int_{\frac{d}{2}}^{\frac{D}{2}} \frac{\tau_o d}{2 r G_m} dr = \frac{\tau_o d}{2 G_m} \ln\left(\frac{D}{d}\right) = v - u \quad (\text{A11})$$

Now using (A2) and (A11) h can be evaluated as

$$h = \frac{8 G_m}{d^2 \ln\left(\frac{D}{d}\right)} \quad (\text{A12})$$

Figure A2 shows the Cox Model stress predictions for the W-FeCrAlY material system subject to a heat-up of 100 C. A cool-down of 100 C would result in predictions of equal magnitude but opposite sign.

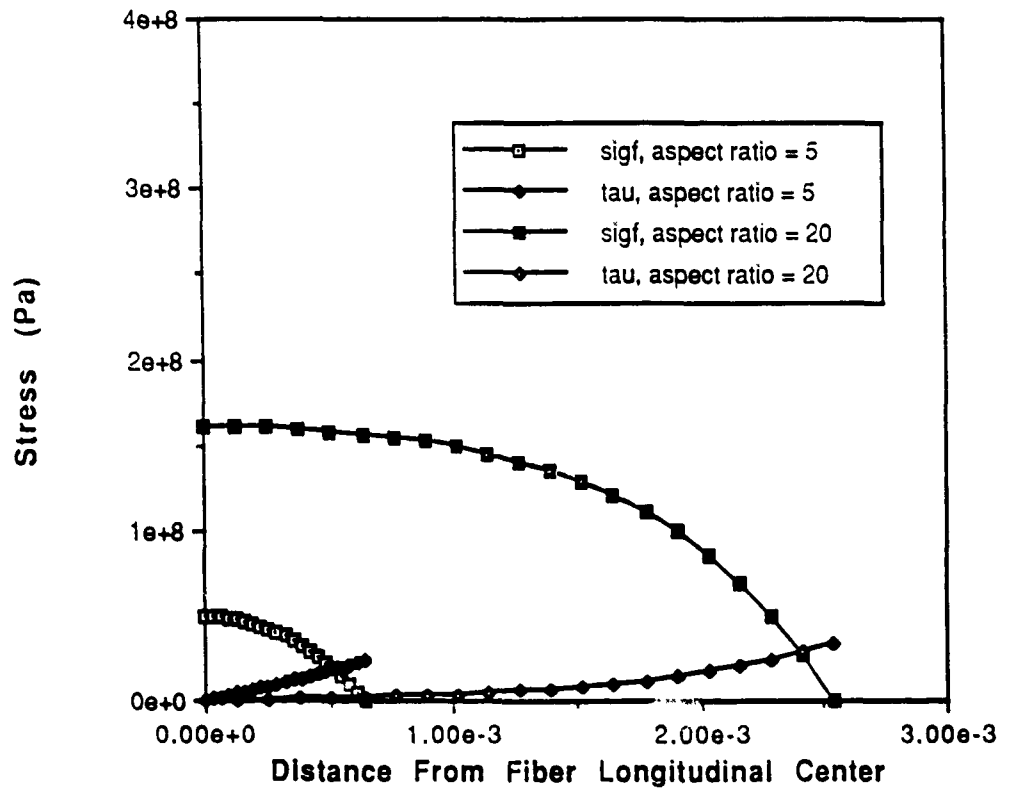


Figure A2. Cox Model Result For W-FeCrAlY Composites.

Appendix B Eshelby Tensors

(Lulay,1990)

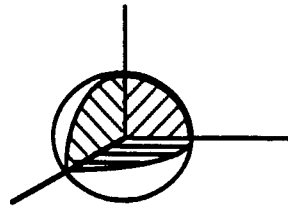


Figure B.1 Sphere.

Eshelby's tensors for Figure B.1:

$$S_{1111} = S_{2222} = S_{3333} = \frac{7 - 5\nu}{15(1 - \nu)}$$

$$S_{1122} = S_{2233} = S_{3311} = S_{2211} = S_{3322} = \frac{5\nu - 1}{15(1 - \nu)}$$

$$S_{1212} = S_{2323} = S_{3131} = \frac{4 - 5\nu}{15(1 - \nu)}$$

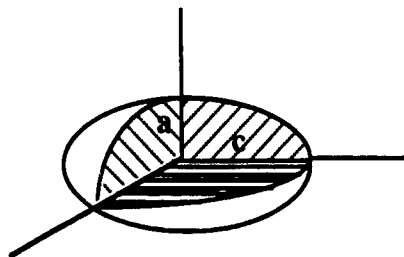


Figure B.2 Oblate spheroid.

Eshelby's tensors for Figure B.2:

$$S_{1111} = S_{2222} = \frac{3}{8(1-\nu)} \left\{ 1 - \frac{1}{1-\beta^2} \right\} + \frac{g}{4(1-\nu)} \left\{ \frac{9}{4(1-\beta^2)} + 1 - 2\nu \right\}$$

$$S_{3333} = 1 - \frac{\beta^2}{(1-\nu)(1-\beta^2)} + \frac{g}{2(1-\nu)} \left\{ \frac{3\beta^2}{1-\beta^2} - (1-2\nu) \right\}$$

$$S_{1122} = S_{2211} = \frac{1}{8(1-\nu)} \left\{ 1 - \frac{1}{1-\beta^2} \right\} + \frac{g}{4(1-\nu)} \left\{ \frac{3}{4(1-\beta^2)} - (1-2\nu) \right\}$$

$$S_{1133} = S_{2233} = \frac{\beta^2}{2(1-\nu)(1-\beta^2)} - \frac{g}{4(1-\nu)} \left\{ \frac{3\beta^2}{1-\beta^2} + 1 - 2\nu \right\}$$

$$S_{3311} = S_{3322} = \frac{1}{2(1-\nu)} \left\{ \frac{3}{2(1-\beta^2)} - (1-2\nu) \right\} - \frac{g}{4(1-\nu)} \left\{ \frac{3}{4(1-\beta^2)} - (1-2\nu) \right\}$$

$$S_{1212} = -\frac{1}{8(1-\nu)} \frac{\beta^2}{(1-\beta^2)} + \frac{g}{16(1-\nu)} \left\{ \frac{3}{1-\beta^2} + 4(1-2\nu) \right\}$$

$$S_{1313} = S_{2323} = \sqrt{(1-4(1-\nu))} \sqrt{(1-2\nu + \sqrt{(1+\beta^2)(1-\beta^2)})} - \sqrt{g, 8(1-\nu)} \left\{ 1 - 2\nu + 3 \frac{1+\beta^2}{1-\beta^2} \right\}$$

where

$$g = \frac{\beta}{(1-\beta^2)^{3/2}} \left\{ \cos^{-1}\beta - \beta(1-\beta^2)^{1/2} \right\}$$

$$\beta = \frac{a}{c} < 1$$

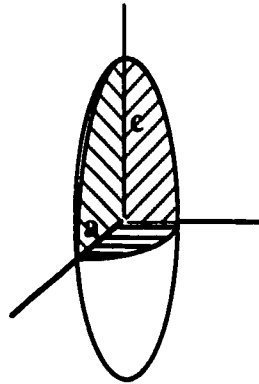


Figure B.3 Prolate spheroid.

Eshelby's tensors for Figure B.3:

$$S_{1111} = S_{2222} = \frac{3}{8(1-\nu)} \frac{\beta^2}{\beta^2 - 1} + \frac{g}{4(1-\nu)} \left\{ 1 - 2\nu - \frac{9}{4(\beta^2 - 1)} \right\}$$

$$S_{3333} = \frac{1}{2(1-\nu)} \left[1 - 2\nu + \frac{3\beta^2 - 1}{\beta^2 - 1} - \left\{ 1 - 2\nu + \frac{3\beta^2}{\beta^2 - 1} \right\} g \right]$$

$$S_{1122} = S_{2211} = \frac{1}{4(1-\nu)} \left[\frac{\beta^2}{2(\beta^2 - 1)} - \left\{ 1 - 2\nu + \frac{3}{4(\beta^2 - 1)} \right\} g \right]$$

$$S_{1133} = S_{2233} = -\frac{1}{2(1-\nu)} \frac{\beta^2}{(\beta^2-1)} + \frac{1}{4(1-\nu)} \left\{ \frac{3\beta^2}{\beta^2-1} - (1-2\nu) \right\} g$$

$$S_{3311} = S_{3322} = -\frac{1}{2(1-\nu)} \left\{ 1-2\nu + \frac{1}{\beta^2-1} \right\} + \frac{1}{2(1-\nu)} \left\{ 1-2\nu + \frac{3}{2(\beta^2-1)} \right\}$$

$$S_{1212} = \frac{1}{8(1-\nu)} \frac{\beta^2}{(\beta^2-1)} + \frac{g}{4(1-\nu)} \left\{ 1-2\nu - \frac{3}{4(\beta^2-1)} \right\}$$

$$S_{1313} = S_{2323} = \frac{1}{4(1-\nu)} \left\{ 1-2\nu - \frac{\beta^2+1}{\beta^2-1} \right\} - \frac{g}{8(1-\nu)} \left\{ 1-2\nu - \frac{3(\beta^2+1)}{\beta^2-1} \right\}$$

where:

$$g = \frac{\beta}{(\beta^2-1)^{3/2}} \left\{ \beta(\beta^2-1)^{1/2} - \cosh^{-1}\beta \right\}$$

$$\beta = \frac{c}{a} > 1$$